COMPUTATIONAL STUDY OF INTERACTION OF TWIN RECTANGULAR JETS

A Dissertation

by

HAN LI

Submitted to the Office of Graduate and Professional Studies of
Texas A&M University
in partial fulfillment of the requirements for the degree of

DOCTOR OF PHILOSOPHY

Chair of Committee,	N.K. Anand
Co-Chair of Committee,	Yassin A. Hassan
Committee Members,	Hamn-Ching Chen
	Maria King
Head of Department,	Andreas A. Polycarpou

December 2018

Major Subject: Mechanical Engineering

Copyright 2018 Han Li

ABSTRACT

Turbulent jet interactions play a significant role in terms of momentum and heat transfer. Interactions of multiple turbulent jets occurs in next-generation nuclear reactors, where high-temperature flow mixing in the lower plenum and mixing fluctuations in the coolant may influence power oscillations and flow-induced vibrations. Thus, the estimation of mixing condition needs to be accurate. Recent benchmark experiments using the particle image velocimetry (PIV) technique provided high-fidelity experimental data that could be used in verification studies. Computational fluid dynamics (CFD) simulations are extensively employed in the study of mixing phenomenon of parallel jets. Therefore, the validation of various turbulence models is of great importance for ensuring that the numerical results are reliable and can serve as a guide for future designs.

In this study, an open source CFD library, i.e., OpenFOAM, was utilized to conduct numerical simulations of twin jets. This work consists of two parts: one part focuses on steady-state simulations and the other on transient simulations. In the first part, the steady state Reynolds-averaged Navier-Stokes (RANS) models, such as the realizable k - ϵ and the shear stress transport k - ω, were used for the steady-state validation study. Steady-state simulations showed that with proper boundary conditions at the inlets, the mean velocity data agreed well with the experimental data within engineering accuracy (14%). In the second part, the partially averaged Navier - Stokes (PANS) models were implemented in the code and were utilized to conduct transient simulations. Fluctuating inlet boundary conditions from experiments were employed. The results obtained from PANS and the unsteady RANS (URANS) models were com-

pared with experimental data. The PANS model showed a good agreement with the experimental data in terms of the merging point (4.3%). In addition, the k - ϵ PANS model was compared with the k - ϵ URANS model. A power spectrum density (PSD) analysis was performed based on the velocity at four sample locations to compare the resolved frequencies between the PANS and URANS models. It was observed that the PANS model showed better capabilities of resolving higher turbulence flow frequencies compared to the URANS based on the PSD analysis.

Another part of this study included the use of large eddy simulation numerical methodology on a parallel jet system and the computational results were validated against the benchmark PIV experiments. The results indicated a good agreement in terms of the merging point and time-averaged velocity profile. Spectral analyses via Welch's power spectral density functions were used to analyze frequency information in turbulent jets. The proper orthogonal decomposition (POD) analysis method was applied using a snapshot method. The POD analysis showed vortex structures similar to those in the benchmark PIV experiment.

DEDICATION

To My mother Junyan Li,

and

My father Shubin Li

ACKNOWLEDGMENTS

I am greatly indebted to my academic advisors, Dr. N. K. Anand and Dr. Yassin Hassan who supervised my doctoral work and provided tremendous support and encouragement, without which this dissertation would not have materialized. I am particularly thankful for their valuable insights and patience to train me to be a researcher.

I am also grateful to Dr. Hamn-Ching Chen and Dr. Maria King for taking time to serve as the committee members. Their feedbacks have greatly enhanced my dissertation.

Many thanks to my friends and colleagues in my research group for their help and support. The staff at Texas A&M High Performance Research Computing (HPRC) group are also gratefully acknowledged for providing assistance and computing resources.

Finally, I am ever thankful to my mother, Junyan Li, and my father, Shubin Li, for their continuous encouragement and support.

CONTRIBUTORS AND FUNDING SOURCES

Contributors

This work was supported by a dissertation committee consisting of Professor N. K. Anand of the Department of Mechanical Engineering, Professor Yassin Hassan of the Department of Nuclear Engineering, Professor Hamn-Ching Chen of the Department of Civil Engineering and Professor Maria King of the Department of Biological and Agricultural Engineering.

All other work conducted for the dissertation was completed by the student independently.

Funding Sources

This project is partially funded by nuclear energy advanced modeling and simulation (NEAMS) program under U.S. Department of Energy (DOE).

NOMENCLATURE

a	Jet width
$C_1, A_s, W, \tilde{S}$	Coefficients for realizable $k-\epsilon$ model
C_2, A_0	Constants for realizable $k-\epsilon$ model
$C_{\epsilon 1}, C_{\epsilon 2}, C_\mu$	Closure coefficients for $k-\epsilon$ models
$C^*_{\epsilon 2}$	Closure coefficient for PANS $k-\epsilon$ model
C_S	Smagorinsky constant
C_w	Constant for wall-adapting local eddy-viscosity (WALE) large eddy simulation (LES) model
f	Quantity of interest for grid convergence index (GCI) calculation
f_k	Unresolved-to-total ratio of turbulent kinetic energy
f_ϵ	Unresolved-to-total ratio of turbulent dissipation rate
$\overline{g}_{ij}$	Filtered velocity gradient tensor
k	Tubulent kinetic energy
L	Length of the jet nozzle
l	Length scale of turbulence
p	Formal order of accuracy
P_k	Production of tubulent kinetic energy
r	Grid refinement factor

Re	Reynolds number
$\mathbf{S}$	Jet spacing
S_{ij}	Mean rate of strain tensor
T	Time period (s)
t	Time (s)
u′,v′,w′	Fluctuating part of velocity in x, y, and z-directions ($m \cdot s^{-1}$)
$\overline{u}, \overline{v}, \overline{w}$	Filtered velocity in x, y, and z-directions ($m \cdot s^{-1}$)
U, V, W	Mean velocity in x, y, and z-directions ($m \cdot s^{-1}$)
u, v, w	Instantaneous velocity in x, y, and z-directions ($m \cdot s^{-1}$)
$\mathbb{V}$	System volume

List of Abbriviations

CFD	Computational fluid dynamics
CP	Combining point
DNS	Direct numerical simulation
GCI	Grid convergence index
HWA	Hot wire anemometry
LDA	Laser Doppler anemometry
LES	Large eddy simulations
LUST	Linear-upwind stablized transport
MP	Merging point
PANS	Partially averaged Navier-Stokes equations

PIV	Particle image velocimetry
POD	Proper orthogonal decomposition
PSD	Power spectral density
RANS	Reynolds-averaged Navier-Stokes equations
RMS	Root mean square
SFR	Sodium-fast reactors
SFS	Sub-filter stress
SGS stress	Sub-grid scale stress
URANS	Unsteady Reynolds-averaged Navier-Stokes equations

Greek Symbols

$\alpha_1, \beta_1, \alpha_2, \beta_2, \sigma_\omega$	Model coefficient for shear stress transport (SST) $k-\omega$ model
Δ	Grid spacing
δ_{ij}	Kronecker delta
ϵ	Rate of dissipation of turbulent kinetic energy
η	Model coefficient for realizable $k-\epsilon$ model
Λ	Taylor scale of turbulence
μ	Dynamic viscosity
μ_t	Turbulent dynamic viscosity
ν	Kinematic viscosity
ν_t	Turbulent kinematic viscosity
ω	Specific rate of dissipation

Ω_{ij}	Mean rate of rotation tensor
ρ	Density
$\sigma_k, \sigma_\epsilon,$	Closure constants for $k-\epsilon$ models
$\sigma_{ku}, \sigma_{\epsilon u},$	Closure constants for $k-\epsilon$ models
τ	Unresolved stress term

Subscripts

$fine$	Finer mesh
i, j	Index variables for tensor notation
MAX	Maximum
SGS	Sub-grid scale
u	Unresolved portion

Superscipts

—	LES/PANS filtered variables
$\rightarrow$	Vector
n	Index variable associated with time step

TABLE OF CONTENTS

Page

LIST OF FIGURES

FIGURE Page

LIST OF TABLES

TABLE Page

1. INTRODUCTION *

1.1 Overview of twin jets flows

A system of two or more parallel jets has an interesting flow structure, which could accomplish rapid mixing. The mixing feature of parallel jets can be found in several engineering applications (e.g., in very high temperature reactor). The coolants merge in the upper or lower plenum, after passing through the reactor core. In sodium-cooled fast reactors (SFR), the mixing of different-temperature fluids from jets can cause thermal stresses and flow-induced vibration in a rod bundle. In cooling applications of electronic packages, jet impingement is considered as an efficient strategy for heat removal. In boiler burners, a fuel injection system with parallel jets can be an effective strategy to achieve fuel mixing. Because of the importance of multiple-jet systems and their wide range of applications, a study on the interaction between parallel turbulent jets is necessary. This study focuses on two parallel jets referred to as twin jets.

Computational fluid dynamics (CFD) can be used extensively to aid in the design of systems and components. However, in order to use CFD tools for design and analysis purposes, validation work is necessary, such as by comparing numerical data against benchmark experimental results. A twin-jet water facility was designed to investigate the thermal hydraulic phenomenon and measurement techniques for advanced reactors such as SFR. The experimental efforts started at the University of Tennessee, Knoxville [1] and later moved to Texas A&M University [2–4] for benchmarking experiments using non-intrusive measurement techniques such as laser Doppler anemometry (LDA) and

*Part of the content in this section is reprinted with permission from H. Li, N. K. Anand, and Y. A. Hassan, "Computational study of turbulent flow interaction between twin rectangular jets," *Int. J. Heat Mass Transf.,* vol. 119, pp. 752-767, Apr. 2018. Copyright [2018] by Elsevier

particle image velocimetry (PIV). Benchmark data by Wang et al. [2] included time-averaged velocity, vorticity, and Reynolds stress profiles. Another experimental work by Lee et al. [4] based on the same facility and operating conditions provided additional spectral information and proper orthogonal decomposition (POD) analysis with high-frequency data collection method of up to 2000Hz. In this study, the simulation results were compared to the time-averaged experimental data by Wang et al. [2] and the data by Lee et al. [4] for spectral information of turbulent flow.

It is beneficial to introduce the typical structure of twin jets flow, which is shown in figure 1.1. Twin jets flows have three distinct regions: converging region, merging region, and combined region. In the converging region, there is recirculation between the two jets, and the jet interactions are still at a primitive stage. At the end of the converging region, the mean velocity along the axis of symmetry is zero. This location is defined as the merging point (MP). Beyond the MP, twin jets start to merge into a single jet. The point at which the flow behaves as a single jet is defined as the combining point (CP); this means that the streamwise mean velocity U at the symmetry line reaches its maximum. The region between MP and CP is defined as the merging region. The region beyond CP is the combined region. Two vital parameters are often used to describe the twin-jet system, namely the jet width $\boldsymbol{a}$ and the jet spacing S.

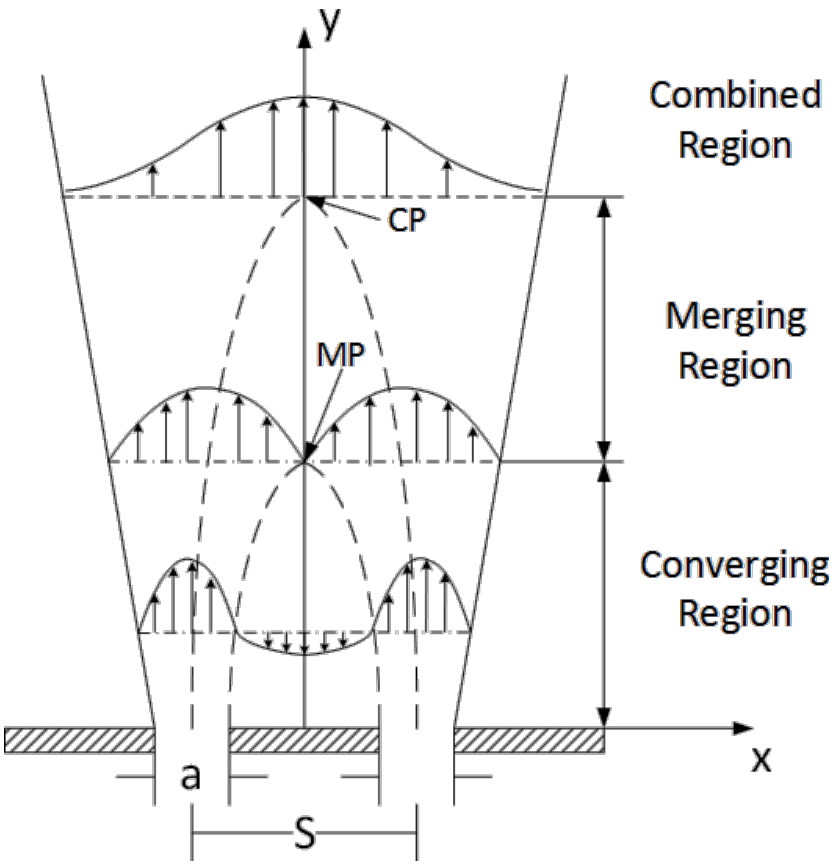

Figure 1.1: Schematic of the twin jets flow structure.

1.2 OpenFOAM

The solver used in the present work is OpenFOAM. OpenFOAM originally stands for "Open source **F**ield **O**peration **A**nd **M**anipulation" which is a C++ toolbox with numerical solvers for computational mechanics including CFD. OpenFOAM is the leading free, open source software for CFD, owned by the OpenFOAM Foundation [5]. It is distributed exclusively under the General Public License (GPL). GPL provides users the freedom to modify and redistribute the software and a guarantee of continued free use, within the terms of the license. The development of OpenFOAM was initiated by Prof. David Gosman and Dr. Radd Issa, with principal developers, Mr. Henry Weller

and Dr. Hrvoje Jasak [6]. It was based on the finite volume method taking advantage of the object-oriented programming in C++. Figure 1.2 shows the structure of the OpenFOAM package. OpenFOAM is a comprehensive toolbox, which is capable of pre-processing, solving, and post-processing.

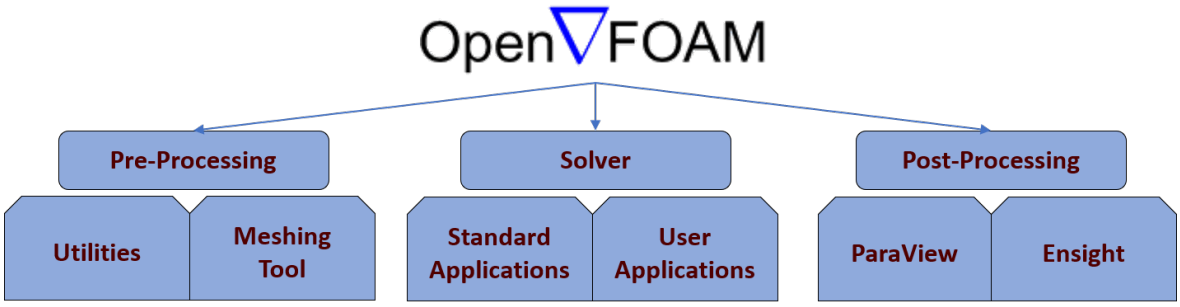

Figure 1.2: Illustration of OpenFOAM library structure.

1.3 Brief introduction on turbulent models

Because the twin jets flow in the present work is turbulent, this section provides a brief introduction on turbulent flow and turbulence models. Three different categories of turbulence models are used in this study: Reynolds averaged Navier-Stokes models, a partially averaged Navier-Stokes (PANS) model, and large eddy simulations (LES). RANS can perform steady-state and unsteady simulations (transient). The steady-state simulation in Section 3 is referred to as RANS, whereas the unsteady simulation is referred to as URANS. RANS/URANS models were intended to provide practical approaches to perform turbulent flow simulations with less computational cost. LES was proposed to compute the complete time history of turbulent flow with rich physics resolved. The PANS model was developed to be a hybrid method which was intended to bridge between RANS/URANS and LES.

In turbulent flows, the kinetic energy distributed among various scales of fluid motion can be described using an energy spectrum as a function of wavenumber [7], as shown using a log-log scale in figure 1.3. The kinetic energy is pumped into turbulence flow from external sources at large scale, which is also called energy containing scales. Turbulence extracts energy at large scales and eventually makes it available to small scales. Large-scale motions induce smaller scale motions by a process called energy cascade. The mathematical origin of energy cascade is the nonlinear term in the Navier-Stokes equations [7]. The energy cascade process occurs in the scale range called inertial subrange, where the energy decays at a slope maintained at -5/3, which is also known as Kolmogorov -5/3 law [8]. In the energy cascade process, the kinetic energy in larger eddies gradually transfers to smaller eddies. The kinetic energy will continue to dissipate into smaller scales, where molecular viscosity takes over, called dissipation range. Most RANS/URANS models that relied on the Kolmogorov -5/3 law, where the entire energy cascading processes occur, have been modeled. On the other hand, the LES filtering method is applied based on wavenumber cut-off, where the smaller-scale turbulence in the dissipation range is assumed to have a universal behavior. Thus, the energy cascading process of turbulence flow motion is resolved in LES. PANS can be a bridging method that smoothly connects modeled flow scales based on parameters from RANS/URANS to LES as needed.

In this study, those three categories of turbulence modeling methodologies are employed on twin-jet flows as presented in Sections 3 to 5.

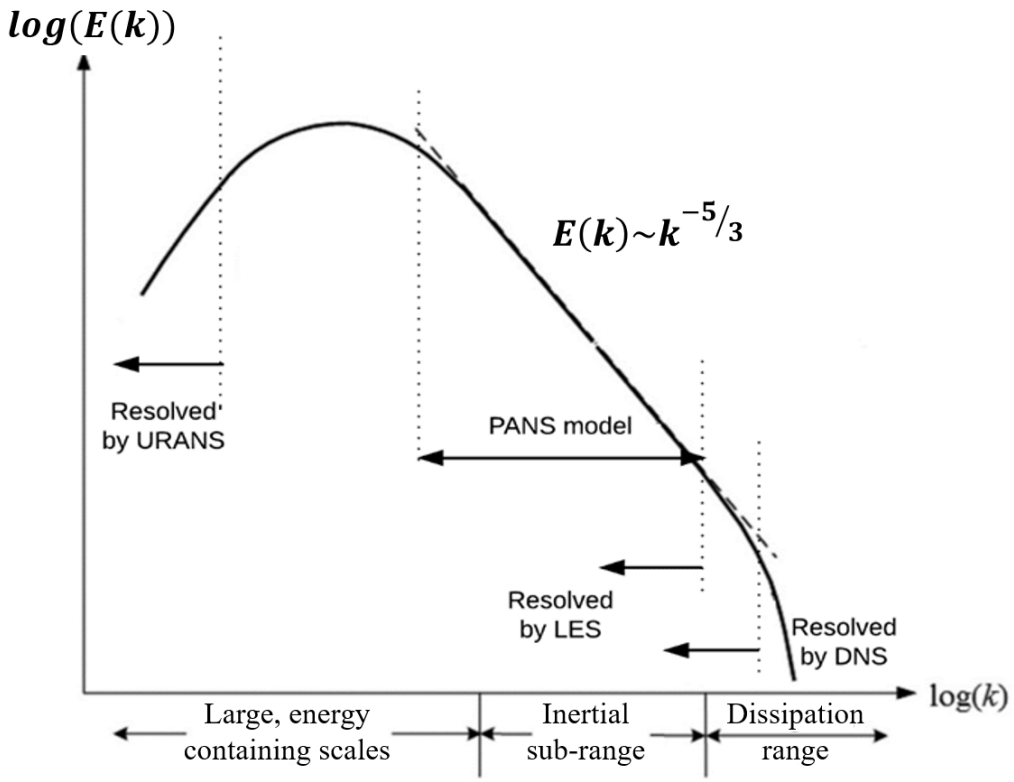

Figure 1.3: Typical energy spectrum in turbulent flow

1.4 Outline

This dissertation is organized as follows: Section 2 presents a literature review of twin-jet flows, whereas Section 3 focused on steady state RANS models. Section 4 discusses the development and results of the PANS models and the URANS simulations are presented as a comparison case. Section 5 presents the results and analysis with LES. This work concludes with a summary in Section 6.

2. LITERATURE REVIEW *

The history of twin jets study can be traced back to 1960. Miller and Comings [9] experimentally investigated the merging of a dual-jet flow using hot-wire anemometer (HWA) with air as working fluid. The spacing ratio (S/a) was 6, and the aspect ratio was 40. Based on the large aspect ratio, this study was treated as a study of a two-dimensional twin jets system. The mean flow of their measurements presented a symmetry along the centerline, and the merging point (MP) was reported to be at $y/\mathbf{a} = 7$. Their study revealed that after a particular location, the two jets combined into a single jet. Tanaka [10, 11] reported experimental studies on twin jets, with air issuing from parallel slot nozzles, he employed the HWA method. The study was focused on the effect of changing the distance between nozzles (S/a), varying from 8.5 to 26.3. In his first report [10], the author focused on the interference between the two jets and proposed a correlation between the MPs and spacing ratios. The author discovered a negative pressure region between the two jets due to the circulation of flow. In the second report, Tanaka [11] focused on the combined flow of the twin jets. The results confirmed that the combined flow profile agreed well with the single-jet velocity distributions; the width of the combined jet spread linearly downstream as a single one.

Marsters [12] introduced an integral method for predicting the mixing of twin jets and conducted an experimental work on the mean flow using parallel-plane jets. The author's model predictions agreed well with the experimental data. The author also

*Part of the content in this section is reprinted with permission from H. Li, N. K. Anand, and Y. A. Hassan, "Computational study of turbulent flow interaction between twin rectangular jets," *Int. J. Heat Mass Transf.,* vol. 119, pp. 752-767, Apr. 2018. Copyright [2018] by Elsevier

found that the static pressure distribution along the centerline of the flow field is insensitive to the Reynolds number within the range of 8,600< Re <15,700. Elbanna and Gahin [13] investigated twin jets with a spacing ratio of 12.5 using the HWA technique. The authors found that jets that spread linearly behaved in a manner similar to that of a single jet; however, the three components of velocity fluctuations showed different behaviors.

Self-preservation is a jet-flow feature that normalizes the velocity profile to be similar at different locations downstream of the jet entrance. Lin and Sheu [14] conducted experiments with parallel-plane jets, with spacing ratios of 30 and 40. They found that the mean velocity was self-preserving in the converging and combined regions, whereas the Reynolds stress exhibited self-preserving behavior only in the combined region.

During the early stages of experimental research on twin jets, HWA, which is an intrusive measurement method, was extensively used. In 1997, the laser Doppler anemometry (LDA) measuring system, which is a non-intrusive measuring technique, was first used by Nasr and Lai in the study of twin jets [15]. The spacing ratio was 4.25, and the results confirmed that the development of coherent structures created from the shear layer instability was significant in controlling the dynamics of twin jets [15]. Bunderson and Smith [16] conducted experiments on parallel-jet mixing using the Schlieren flow visualization and HWA. The spacing ratio was between 7 and 27. Their experiments showed that parallel jets flapped when the two jets had equal momentum flux. The oscillation frequency was similar to that of the wake of the flow over a bluff body. Moreover, the results indicated that controlling the momentum flux ratio of the jets could be an effective method for limiting or enhancing jet mixing.

Computational fluid dynamics (CFD) as a useful engineering design tool, was used

in several twin jets studies. Lai and Nasr [17] compared their previous LDA results [15] with two-dimensional simulations of three Reynolds averaged Navier-Stokes (RANS) models (RANS will be further explained in Section 3.1), namely the standard $k-\epsilon$, the renormalization group (RNG) $k-\epsilon$, and the Reynolds stress model. The simulations overpredicted the MP by 8% to 18% compared with the LDA experimental data obtained by the authors [15]. Anderson and Spall [18] conducted a two-dimensional simulation of the standard $k-\epsilon$ model and the Reynolds stress model and compared their own experimental data using the HWA measurements for twin jets with spacing ratios between 9 and 18.25. The results showed that the models could predict the mean symmetry-plane velocity with satisfactory accuracy. Durve et al. [19] performed a two-dimensional steady-state simulation on two and three jets using the FLUENT solver with the Reynolds stress transport model. In their simulations [19], spacing ratios of 9, 13, and 18.25 were considered. Based on their simulation results, the authors [19] proposed a correlation for predicting the MP as a function of the spacing ratio and jet turbulence intensity. They also proposed a correlation between MP and combined point (CP). The studies [2–4, 9–20] on rectangular twin jets are summarized in table 2.1.

2.1 What is missing?

Most of the previous studies were based on large spacing ratios (S/a) and large aspect ratios (L/a) [9–14, 16, 18]. In addition, the working fluid in previous works was predominantly air. However, liquid jets with small spacing ratios attracted much attention owing to their use in next-generation nuclear reactors and electronic cooling devices.

Tanaka [10] reported that the velocity field and turbulence characteristics are a

function of the spacing ratio and aspect ratio. Previously established empirical correlations are not applicable to parallel jets with small spacing ratios [20]. For the experimental work, the intrusive measurement technique, HWA was used in most early studies [9–14, 16, 18], and LDA was used in recent research activities [3, 15, 20]. Both HWA and LDA are point-by-point measurement techniques. Until recently, PIV, which is a high fidelity measurement method, was used by Wang et al. [2] and Lee et al. [4] to study twin rectangular jets as mentioned in Section 1.

Regarding numerical works on the twin-jet systems, previous research focused on steady-state two-dimensional simulations [17–19], but turbulence flow is a three-dimensional phenomenon. In addition, the simulation by Anderson et al. [18] and Durve et al. [19] was based on large spacing ratios. Literature surveys showed two experimental data using PIV measurements with small spacing ratios [2, 4], but no numerical work has been published for the validation of turbulence models on twin-jet flows. Therefore, a comprehensive validation study of CFD models on the twin-jet systems should be conducted to establish the reliability of using CFD simulations for twin jets with small spacing ratios. One of the aims of this work is to perform a validation study using both steady-state and transient models.

2.2 Objective

The objective of this study is focused on performing three-dimensional numerical simulations for twin-jet systems and comparing the results with recent benchmark experimental data [2–4]. The present simulation work involves steady-state simulations with RANS models, transient simulations with PANS models, and LES. The study includes the following :

- Comparison of steady-state RANS model results with experimental data [2].

- Transient simulations with PANS $k - \epsilon$ model and comparison with URANS simulations and experimental data by Lee et al. [4].
- Sensitivity study of inlet boundary conditions on the prediction of MP in twin jets.
- Investigation using LES on twin-jet systems and validation with experiment [4].
- Proper Orthogonal Decomposition (POD) analysis performed on LES data.

Year	Authors	Fluids	**S/a**	L/a	***Re***	Methods
1960 [9]	Miller et al.	Air	**6**	>50	17,800	Hot-wire
1970 [10]	Tanaka	Air	**8.5- 26.3**	>50	4,290- 8,750	Hot-wire
1974 [11]	Tanaka	Air	**8.5- 26.3**	>50	4,290- 8,750	Hot-wire
1977 [12]	Marsters	Air	**17.25**	40	12,000	Hot-wire
1983 [13]	Elbanna et al.	Air	**12.5**	40.8	20,000	Hot-wire
1990 [14]	Lin et al.	Air	**30 & 40**	90	9,000	Hot-wire
1997 [15]	Nasr et al.	Air	**4.25**	24	11,000	LDA
1998 [17]	Lai et al.	Air	**4.25**	24	11,000	LDA, CFD
2001 [18]	Anderson et al.	Air	**9- 18.25**	32	5,900- 6,100	Hot-wire, CFD
2005 [16]	Bunderson et al.	Air	**7- 27**	32	43,000	Hot-wire
2012 [19]	Durve et al.	N/A	**9, 13, 18.25**	N/A	21,000	CFD
2016 [2, 3]	Wang et al.	Water	**3.07**	15.1	9,100	LDA, PIV
2018 [4]	Lee et al.	Water	**3.07**	15.1	9,100	PIV

Table 2.1: List of twin jets studies.

3. REYNOLDS-AVERAGED NAVIER-STOKES MODELS *

3.1 Reynolds-averaged Navier-Stokes equations

The RANS model concept was introduced by Reynolds [21] in 1884. The basis is the Reynolds decomposition method, which divides any fluid variable into mean values and turbulence fluctuation components. Taking velocity u as an example, the Reynolds decomposition is presented in equation (3.1).

$$u(\overrightarrow{x}, t) = U(\overrightarrow{x}, t) + u'(\overrightarrow{x}, t) \tag{3.1}$$

where u is the instantaneous velocity, U is the velocity subject to Reynolds average, and u' is the fluctuating component of velocity. Although the streamwise velocity is used in equation (3.1), the Reynolds decomposition method applies to any flow field variable.

The averaged value is usually obtained by Reynolds averaging, which assumes a variety of forms involving either an integral or a summation. Three types of averaging are discussed in turbulence modeling research activities, time averaging, spatial averaging and ensemble averaging. The term to describe the variable that is subject to averaging is "mean."

Time averaging is used to describe statistically steady flows, for example, the turbulence pipe flow subject to a constant pressure gradient. The time-averaged quantity is defined in equation (3.2).

*Part of the content in this section is reprinted with permission from H. Li, N. K. Anand, and Y. A. Hassan, "Computational study of turbulent flow interaction between twin rectangular jets," *Int. J. Heat Mass Transf.,* vol. 119, pp. 752-767, Apr. 2018. Copyright [2018] by Elsevier

$$U(\overrightarrow{x}) = \frac{1}{T}\int_0^T u(\overrightarrow{x}, t)dt \tag{3.2}$$

where T is the length of the averaging period, u is the velocity field, and U is the average velocity.

Spatial averaging is suitable for statistically homogeneous turbulence flows. The spatial averaging definition is described by equation (3.3).

$$U(t) = \frac{1}{\mathbb{V}}\iiint_{\mathbb{V}} u(\overrightarrow{x}, t)d\mathbb{V} \tag{3.3}$$

Ensemble averaging is the most general type of Reynolds averaging ideally to describe flows that are neither statistically stationary nor homogeneous. An ideal example of ensemble averaging is the fluid variables from N identical experiments, as equation (3.4) indicates.

$$U(\overrightarrow{x}, t) = \frac{1}{N}\sum_{n=1}^{N} u^n(\overrightarrow{x}, t) \tag{3.4}$$

In this study, the steady-state RANS simulations are based on the time averaging concepts. For isothermal incompressible flow, the conservation of mass was presented in equation (3.5) and the conservation of momentum in **??**.

$$\frac{\partial U_i}{\partial x_i} = 0 \tag{3.5}$$

$$\frac{\partial U_j}{\partial t} + \rho U_i \frac{\partial U_j}{\partial x_i} = -\frac{\partial P}{\partial x_j} + \frac{\partial}{\partial x_i}\left(\mu\frac{\partial U_j}{\partial x_i} - \rho\overline{u_i' u_j'}\right) \tag{3.6}$$

where, U_j represents the mean velocity, ρ the density, and $-\rho\overline{u_i' u_j'}$ is known as the

Reynolds stress tensor. By ignoring the transient term $\frac{\partial U_j}{\partial t}$, this method can be used for steady-state simulations for time-averaged mean velocity and pressure, which is referred to as RANS in the present work The transient RANS simulation is usually referred to as unsteady RANS or URANS.

The fundamental problem for RANS turbulence modeling relies on the calculation method of the Reynolds stress tensor, $-\rho\overline{u_i' u_j'}$. Most RANS models are based on Boussinesq approximation. In 1877 Boussinesq [22] hypothesized that the momentum transfer caused by turbulent eddies can be modeled by an eddy viscosity. This is also analogous to the momentum transfer caused by the molecular motion in a gas that can be described by a molecular viscosity. For incompressible flow, Boussinesq's hypothesis assumed that the Reynolds stress tensor, $-\rho\overline{u_i' u_j'}$, is proportional to the mean strain-rate tensor ($S_{ij} = \frac{\partial U_i}{\partial x_j} + \frac{\partial U_j}{\partial x_i}$).

$$-\rho\overline{u_i' u_j'} = \mu_t \left(\frac{\partial U_i}{\partial x_j} + \frac{\partial U_j}{\partial x_i} \right) - \frac{2}{3}\rho k \delta_{ij} \tag{3.7}$$

where k is the turbulent kinetic energy, μ_t is the eddy viscosity or turbulent viscosity, and δ_{ij} is the Kronecker delta.

One of the most popular turbulence model until the last decade of the twentieth century is the $k-\epsilon$ model, which is based on the closure coefficients from Launder et al. [23]; it is also referred to as the standard $k-\epsilon$ model. In this model, k stands for turbulent kinetic energy, whereas ϵ stands for the rate of dissipation of turbulent kinetic energy. A popular variation of the standard $k-\epsilon$ is the realizable $k-\epsilon$ by Shih et al. [24], which consists of a new dissipation rate equation and a new realizable eddy viscosity formulation. The realizable $k-\epsilon$ model provided improved predictions for the spreading rate of both planar and round jets. It also exhibited superior performance

for flows involving rotation, boundary layers under strong adverse pressure gradients, separation, and recirculation.

Another important two-equation turbulence model is the $k-\omega$ model, where k stands for the turbulent kinetic energy (same as in $k-\epsilon$ models), whereas ω stands for the specific dissipation, also called turbulence frequency; $\omega = \epsilon/k$. The closure coefficients from Wilcox [25] is commonly referred to as the standard $k-\omega$, which provides a superior capability for wall-bounded flows. In 1994, Mentor [26] proposed a two-equation turbulence model that combined the $k-\omega$ model and $k-\epsilon$ model through introducing a "blending function" by employing the ω equation for boundary layers and switching to ϵ equation for the free shear region called shear stress transport $k-\omega$ turbulence (SST $k-\omega$) model. The SST $k-\omega$ model has become very popular and is widely used to predict solutions for typical engineering problems.

In this study, for steady-state simulations, the two RANS models , i.e., realizable $k-\epsilon$ model and SST $k-\omega$ model, are employed.

3.1.1 Standard $k-\epsilon$ model

This section describes the standard $k-\epsilon$ model from Launder et al. [23].

Turbulent kinetic energy k:

$$\rho\frac{\partial}{\partial t}(k) + \rho U_i \frac{\partial}{\partial x_i}(k) = \frac{\partial}{\partial x_j}\left[\left(\mu + \frac{\mu_t}{\sigma_k}\right)\frac{\partial k}{\partial x_j}\right] + P_k - \rho\epsilon \tag{3.8}$$

Dissipation rate ϵ:

$$\rho\frac{\partial}{\partial t}(\epsilon) + \rho U_i \frac{\partial}{\partial x_i}(\epsilon) = \frac{\partial}{\partial x_j}\left[\left(\mu + \frac{\mu_t}{\sigma_\epsilon}\right)\frac{\partial \epsilon}{\partial x_j}\right] + C_{\epsilon 1}\frac{\epsilon}{k}P_k - C_{\epsilon 2}\frac{\epsilon^2}{k}\rho \tag{3.9}$$

where the turbulent viscosity is modeled as $\mu_t = \rho C_\mu \frac{k^2}{\epsilon}$, and P_k is the production of

turbulence kinetic energy (k); $P_k = -\rho\overline{u_i' u_j'}\frac{\partial U_j}{\partial x_i}$. The closure coefficients are listed in table 3.1.

$C_{\epsilon 1}$	$C_{\epsilon 2}$	C_μ	σ_k	σ_ϵ
1.44	1.92	0.09	1.0	1.3

Table 3.1: Closure coefficients of standard $k-\epsilon$ model.

3.1.2 Realizable $k-\epsilon$ model

This section explains the realizable $k-\epsilon$ model by Shih et al. [24]. In this model, the k-equation is the same as the standard $k-\epsilon$ in equation (3.8).

The dissipation rate for realizable $k-\epsilon$ model is:

$$\rho\frac{\partial}{\partial t}(\epsilon) + \rho U_i \frac{\partial}{\partial x_i}(\epsilon) = \frac{\partial}{\partial x_j}\left[\left(\mu + \frac{\mu_t}{\sigma_\epsilon}\right)\frac{\partial \epsilon}{\partial x_j}\right] + \rho C_1 S\epsilon - \rho C_2 \frac{\epsilon^2}{k+\sqrt{\nu\epsilon}} \tag{3.10}$$

where the auxiliary relations are defined as

$$C_1 = max\left(0.43, \frac{\eta}{\eta+5}\right)$$

$$\eta = \frac{\overline{S}k}{\epsilon}$$

$$\overline{S} = \sqrt{2S_{ij}S_{ij}}$$

$$S_{ij} = \frac{1}{2}\left(\frac{\partial U_i}{\partial x_j} + \frac{\partial U_j}{\partial x_i}\right)$$

$$\Omega_{ij} = \frac{1}{2}\left(\frac{\partial U_i}{\partial x_j} - \frac{\partial U_j}{\partial x_i}\right)$$

$$C_\mu = \frac{1}{A_0 + A_s U^{(*)} \frac{k}{\epsilon}}$$

$$U^{(*)} = \sqrt{S_{ij} S_{ij} + \Omega_{ij} \Omega_{ij}}$$

$$A_s = \sqrt{6} \left(\frac{1}{3} arccos \left(\sqrt{6} W \right) \right)$$

$$W_0 = \left(\frac{\sqrt{8} S_{ij} S_{jk} S_{kl}}{S} \right)$$

Compared to the standard $k - \epsilon$ model, where $C_\mu = 0.09$, in the realizable $k - \epsilon$ model, C_μ is no longer a constant and is defined as $C_\mu = \frac{1}{A_0 + A_s U^{(*)} \frac{k}{\epsilon}}$. The other closure coefficients are listed in table 3.2.

C_2	A_0	σ_k	σ_ϵ
1.9	4.0	1.0	1.2

Table 3.2: Closure coefficients of realizable $k - \epsilon$ model.

3.1.3 Shear stress transport $k - \omega$ model

This section presents the equations of the SST $k-\omega$ model developed by Menter [26].

Turbulent kinetic energy k :

$$\rho \frac{\partial}{\partial t}(k) + \rho U_i \frac{\partial}{\partial x_i}(k) = \frac{\partial}{\partial x_j} \left[(\mu + \mu_t \sigma_k) \frac{\partial k}{\partial x_j} \right] + P_k - \rho \omega \beta^* \tag{3.11}$$

Specific dissipation rate ω :

$$\rho \frac{\partial}{\partial t}(\omega) + \rho U_i \frac{\partial}{\partial x_i}(\omega) = \frac{\partial}{\partial x_j} \left[(\mu + \mu_t \sigma_\omega) \frac{\partial \omega}{\partial x_j} \right] + \rho \alpha S^2 - \rho \beta \omega^2 + 2(1 - F_1) \sigma_{\omega 2} \frac{1}{\omega} \frac{\partial k}{\partial x_i} \frac{\partial \omega}{\partial x_i} \tag{3.12}$$

where the auxiliary relations are defined as

$$F_1 = tanh\left[\left[min\left[max\left(\frac{2\sqrt{k}}{\beta^*\omega y}, \frac{500\nu}{y^2\omega}\right), \frac{4\sigma_{\omega 2}k}{CD_{k\omega}y^2}\right]\right]^4\right]$$

$$P_k = min\left(\tau_{ij}\frac{\partial U_i}{\partial x_i}, 10\beta^* k\omega\right)$$

$$CD_{k\omega} = max\left(2\rho\sigma_{\omega 2}\frac{1}{\omega}\frac{\partial k}{\partial x_i}\frac{\partial \omega}{\partial x_i}, 10^{-10}\right)$$

Each of the constant below is blended by a blending factor F_1 such that

$$\phi = \phi_1 F_1 + (1 - F_1)\phi_2$$

where ϕ_1 and ϕ_2 are the closure coefficients listed in table 3.3.

α_1	β_1	σ_{k1}	$\sigma_{\omega 1}$
$\frac{5}{9}$	$\frac{3}{40}$	0.85	0.5
α_2	β_2	σ_{k2}	$\sigma_{\omega 2}$
0.44	0.0828	1.0	0.856

Table 3.3: Closure coefficients of SST $k - \omega$ model.

3.2 Simulation setups

For steady-state RANS simulations, the second-order upwind scheme was used for the discretization of momentum equations. The pressure and velocity field were coupled using SIMPLE algorithm [27] which is the ***simpleFoam*** solver in OpenFOAM.The

residuals of all solution variables were monitored. The convergence criterion was set such that all residuals for all variables were less than 10^{-5}.

3.2.1 Computational domain

The computational domain in the present work was intended to simulate the interaction of two parallel jets. Figure 3.1 shows the computational domain for the RANS simulations. The jet outlet length (z-direction) is 87.6 mm, and the width of the jet (**a**) is 5.8 mm. The spacing ratio (**S**) of the jets is 17.8 mm. The size of the computational domain is designed to be comparable to that of the experimental facility [2–4]. The geometric dimensions are 660 × 900 × 680 mm in the x, y, and z directions, respectively. Because the PIV experiments were based on two-dimensional measurements, as shown in figure 3.2, the data extracted in the current simulations were on the same plane.

The computational mesh was generated by an OpenFOAM utility named ***blockMesh***, with a fully hexahedral mesh for the entire domain. The computational meshes in the central region of the domain were finer to ensure that velocity gradients would be properly captured. Figure 3.3 shows the computational mesh. Three mesh sizes with a grid refinement factor of 1.5 were used in the steady-state RANS calculations. The number of cells ranged from 0.8 million to 9.6 million, as listed in table 3.4.

	Smallest cell size (mm)	Total number of cells (millions)
Steady-state RANS Grid 3	0.7250	0.8
Steady-state RANS Grid 2	0.4833	2.8
Steady-state RANS Grid 1	0.3222	9.6

Table 3.4: Mesh details for RANS.

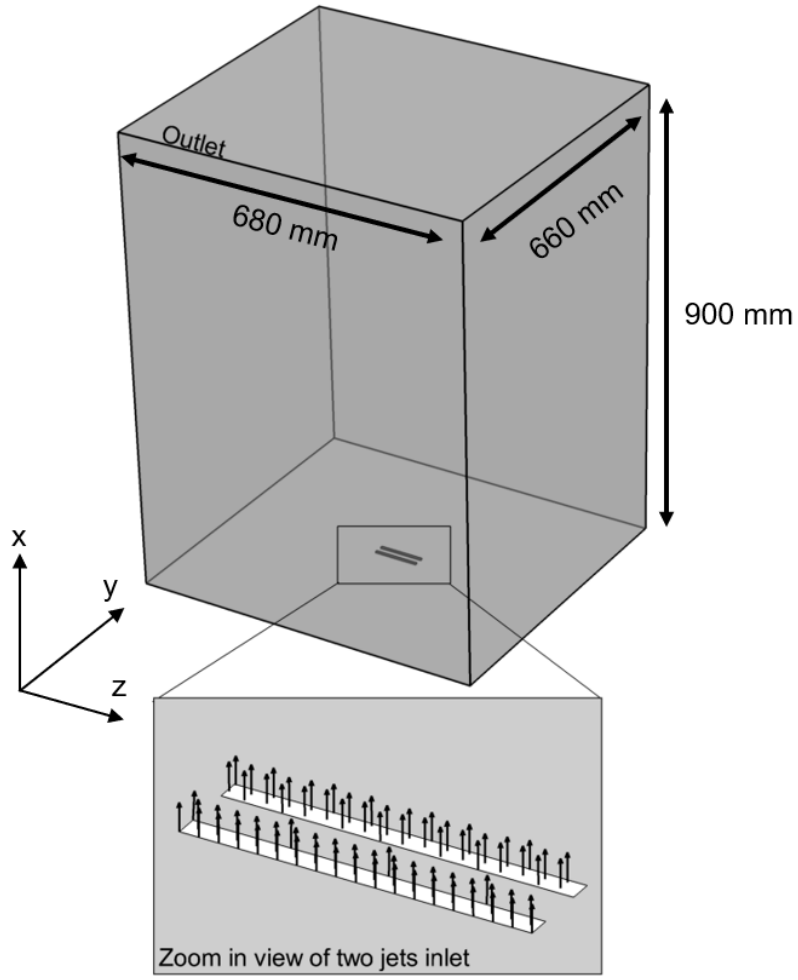

Figure 3.1: Computational domain (RANS, PANS). Reprinted with permission from [28].

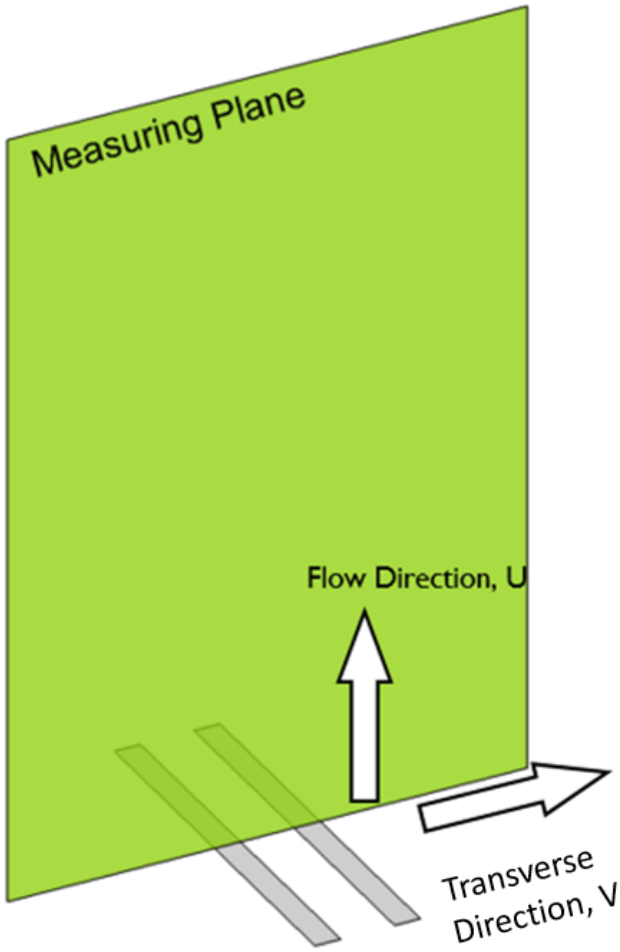

Figure 3.2: A Illustration of PIV measuring plane. Reprinted with permission from [28].

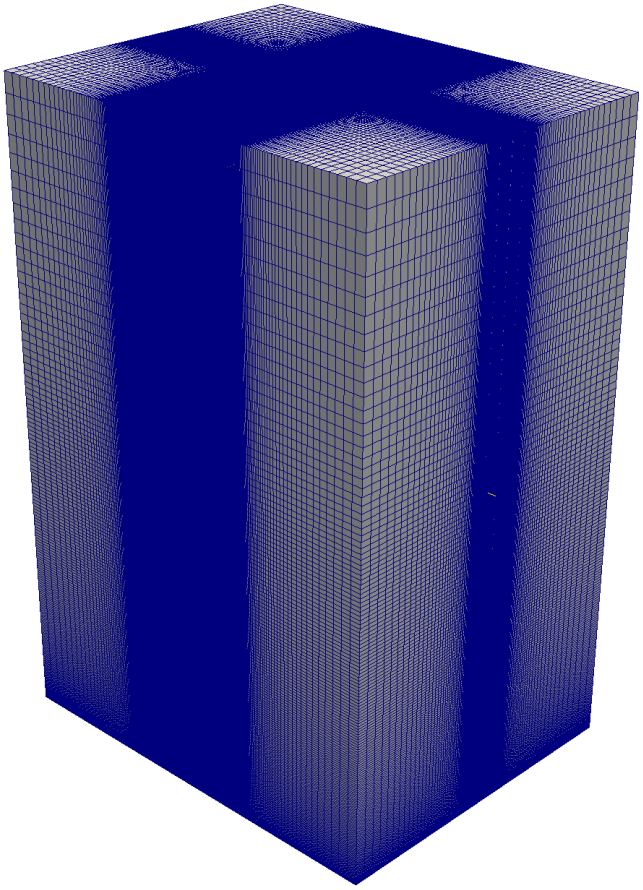

Figure 3.3: A view of the computational grid for RANS simulations. Reprinted with permission from [28].

3.2.2 Boundary conditions

Boundary conditions are essential factors in the present investigation. For the outlet, all simulation cases were using outflow (natural) boundary conditions. Because the walls of the water tank are far away from the jets, the velocity gradient near the walls is relatively small. Therefore, there is no need for wall functions and the no-slip boundary condition was used. The jet inlet boundary conditions were different in all three types of simulations; hence, they will be discussed separately.

In the present study with RANS, the inlet boundary conditions were converted from the PIV experimental data [2], which included the mean streamwise velocity and root-mean-square (RMS) of velocity statistics. The mean velocity profile was used to specif they velocity components of RANS simulations. The RMS of velocity was used for the calculation of turbulence variables such as k, ϵ, and ω. The boundary conditions were calculated from the following equations:

$$k = \frac{1}{2}((\overline{u}_{rms})^2 + (\overline{v}_{rms})^2) \tag{3.13}$$

$$\epsilon = C_{\mu}^{3/4} k^{3/2} l^{-1} \tag{3.14}$$

$$\omega = \frac{\epsilon C_{\mu}}{k} \tag{3.15}$$

where u_{rms} represents the root-mean-square of the U velocity, v_{rms} represents the RMS of V velocity, $C_{\mu} = 0.09$, and l is 10% of the hydraulic diameter. The velocity U and turbulent kinetic energy k profiles are shown in figure 3.4. For the momentum, k and

ϵ equations, a zero-gradient condition was applied at the wall.

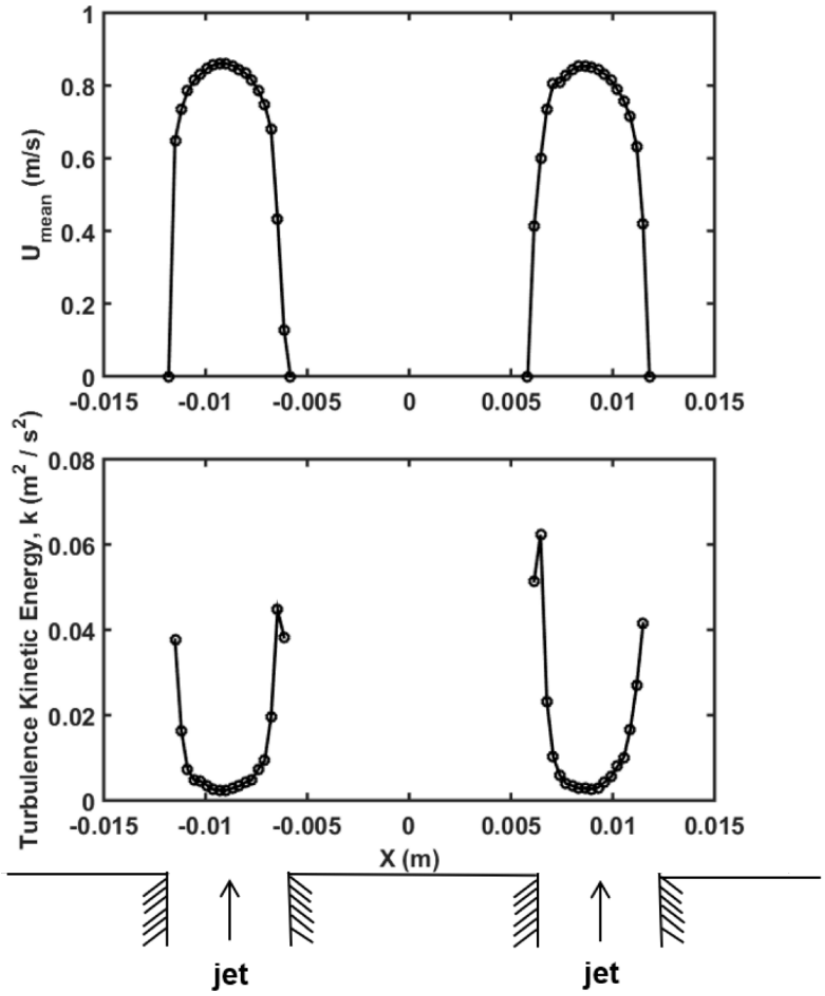

Figure 3.4: Inlet boundary conditions of jets for RANS measured via PIV [2]. Reprinted with permission from [28].

3.3 RANS results

3.3.1 Solution verification with grid convergence index (GCI)

This section presents the grid convergence study with the GCI method [29]. GCI method is a simple method for reporting grid-convergence studies without any restric-

tion to integer refinement (e.g., half-interval method). Compared to conventional grid refinement studies, GCI takes a further step by converting the discretization error estimate into an uncertainty of a grid-converged solution (e.g., error band) [30]. The GCI for the fine grid (GCI_{fine}) is defined as

$$GCI_{fine} = \frac{F_s|\frac{f_1-f_2}{f_1}|}{(r^p-1)} \tag{3.16}$$

where f_2 is the coarse grid solution obtained with grid spacing h_2, f_1 is the fine grid solution obtained with grid spacing h_1, r is the grid refinement factor ($r = h_2/h_1 > 1$), p represents the formal order of accuracy of the algorithm, and F_s is the safety factor, which is 1.5 for the present work with RANS models. The detail of the GCI method are presented in Appendix A. In this section, two RANS models are presented: realizable $k-\epsilon$ and SST $k-\omega$.

Figure 3.5 shows the streamwise velocity (U) along the symmetry line from the realizable $k-\epsilon$. The solutions from three different grids agree well with each other. The three lines almost overlay together. For a quantitative comparison, the MP data with GCI calculation are listed in table 3.5. For the realizable $k-\epsilon$ model, the GCI for MP at Grid 1 is approximately 1.5%, whereas in the SST $k-\omega$ model, the GCI for MP at Grid 1 is approximately 4.5%. Both models in the fine grid exhibit low uncertainties and can be considered as grid-converged solutions.

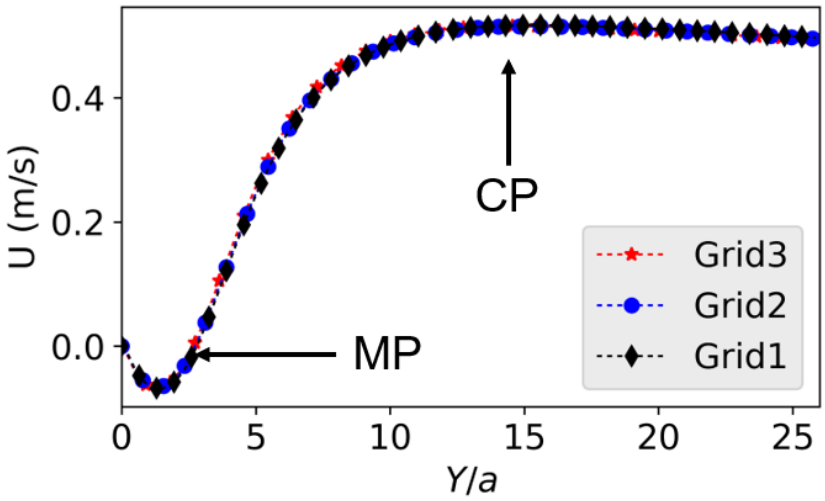

Figure 3.5: Results of streamwise velocity along the centerline obtained from the realizable $k-\epsilon$ model. Reprinted with permission from [28].

Grid #	Realizable $k-\epsilon$	GCI_{fine}	SST $k-\omega$	GCI_{fine}
3 (Coarsest)	2.80a	N/A	2.52a	N/A
2	2.91a	4.385%	2.66a	6.156%
1 (Finest)	2.95a	1.554%	2.76a	4.473%
PIV, Wang et al. [2]	3.45a			
PIV, Lee et al. [4]	3.56a			

Table 3.5: GCI results of merging point (MP) with different meshes.

3.3.2 Solution validation of RANS models

This section presents the solution validation work by comparing the RANS model (realizable $k-\epsilon$ and SST $k-\omega$) results against PIV data [2]. One part of the validation involves comparing the mixing characteristics, i.e., MP; the other part involves comparing the velocity profiles.

For validation purposes, the error in the prediction of MP is defined as

$$E_{MP} = \frac{|MP_{CFD} - MP_{PIV}|}{MP_{PIV}} \times 100\% \tag{3.17}$$

The MP data from CFD and experiments are listed in table 3.5. It can be observed that the MP data obtained from the realizable $k-\epsilon$ are closer to the experimental values ($E_{MP,realizablek-\epsilon} = 14.5\%$) compared to the SST $k-\omega$ data ($E_{MP,SSTk-\omega} = 20.0\%$); however, both models show an underprediction of MP. This could be explained by the overprediction in Reynolds stress (discussed later in this section), which then lead to an overprediction of eddy viscosity.

For comparison of the velocity profile and Reynolds stress profile, four locations along the streamwise direction (y/a = 5.6, 7.0, 10.0, and 11.5) were selected; the locations are marked in figure 3.6. These four locations were selected within the merging region that could represent the merging process. The plots of the velocity and the Reynolds stress profiles are illustrated in figures 3.7 to 3.11. The error bars from the steady-state RANS solutions are based on the GCI pointwise calculation.

The streamwise velocity profiles were expected to be symmetric with respect to X/a = 0 axis; however, owing to the actual experimental conditions and because RANS simulations used experimental data as the boundary conditions, the velocity profiles

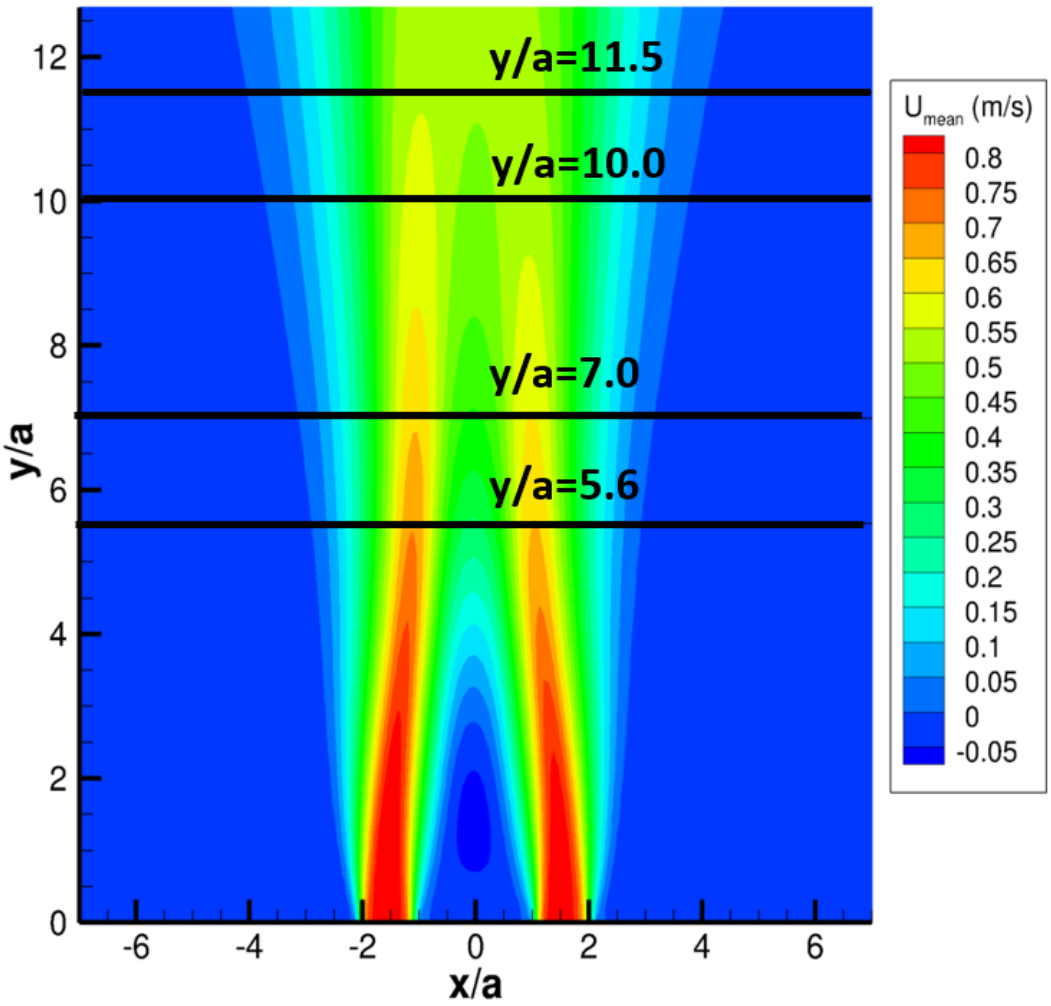

Figure 3.6: Streamwise mean velocity (U) contour plot of realizable $k-\epsilon$. (four selected locations for detail comparison are marked in this plot).

were not perfectly symmetric. The transverse velocity profiles were expected to display an inverted symmetry for the same reason; the inverted-symmetry condition was not perfect in the present study.

Figure 3.7 shows a comparison of the steady-state RANS solutions and the PIV data [2] for the streamwise velocity. The results showed that both models (realizable $k-\epsilon$ and SST $k-\omega$) agree reasonably well with the PIV [2] results. It is worth noting that as flow develops in the streamwise direction, the steady-state RANS solutions

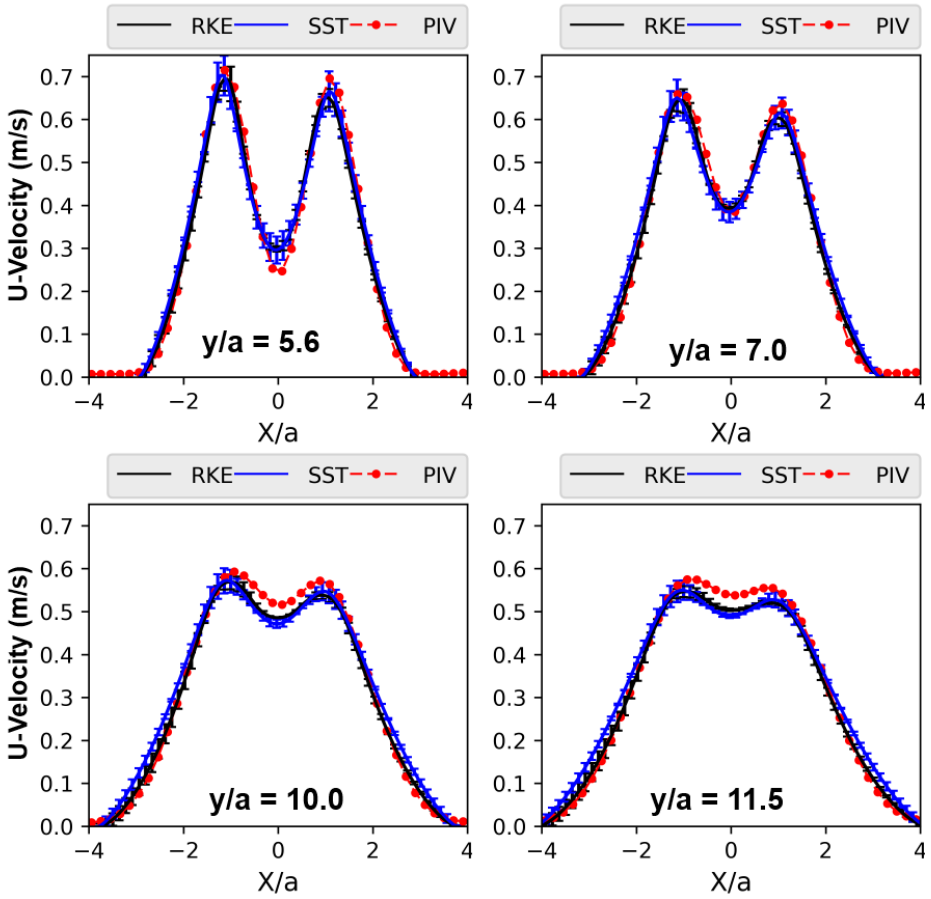

Figure 3.7: Mean streamwise velocity (U) profile comparison at various locations. (RKE: realizable $k-\epsilon$; SST: SST $k-\omega$; PIV: Wang et al. [2]). Reprinted with permission from [28].

tend to slightly underpredict the U velocity. This slight underprediction indicated that the kinetic energy of flow decays faster than expected. Figure 3.8 showed the transverse velocity (V-velocity) of the steady-state RANS solutions and the PIV results. The model predictions agree well with the PIV data [2]; however, the maximum and minimum V-velocity at y/a = 5.6 and 7.0 show noticeable discrepancies. This suggested that the spreading rate of jets is underpredicted in the RANS models.

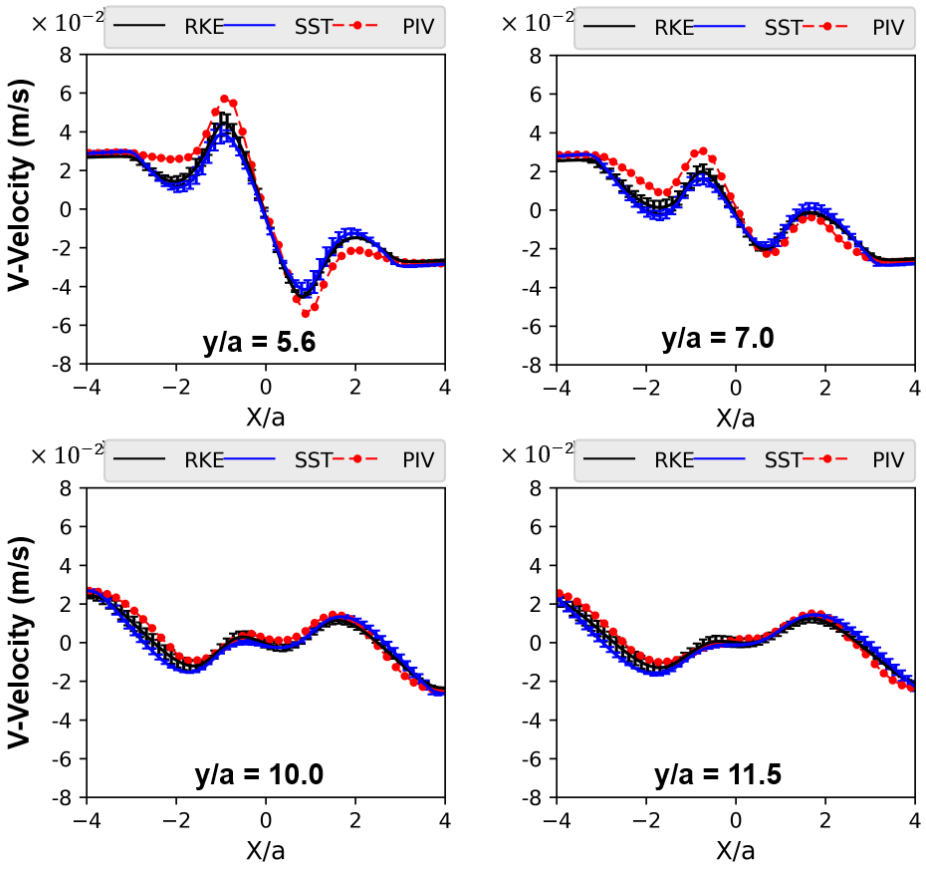

Figure 3.8: Mean spanwise velocity (V) profile comparison at various locations. (RKE: realizable $k-\epsilon$; SST: SST $k-\omega$; PIV: Wang et al. [2]). Reprinted with permission from [28].

The success of a RANS model relies on the accuracy in modeling the Reynolds stress tensor. Thus, the next step of validation is to compare the Reynolds stress profiles against PIV data [2]. The Reynolds stress R_{ij} has a physical interpretation: it is the momentum flux of the i_{th} component in the j_{th} direction caused by the fluctuating velocity field (u' and v'). Experimental data were processed to calculate the RMS of the velocities for the calculation of the Reynolds stress components such that u_{rms} as $\sqrt{\overline{u'u'}}$ and v_{rms} as $\sqrt{\overline{v'v'}}$. Regarding the RANS model, the Reynolds stresses were modeled based on the Boussinesq eddy assumptions as in equation (3.7).

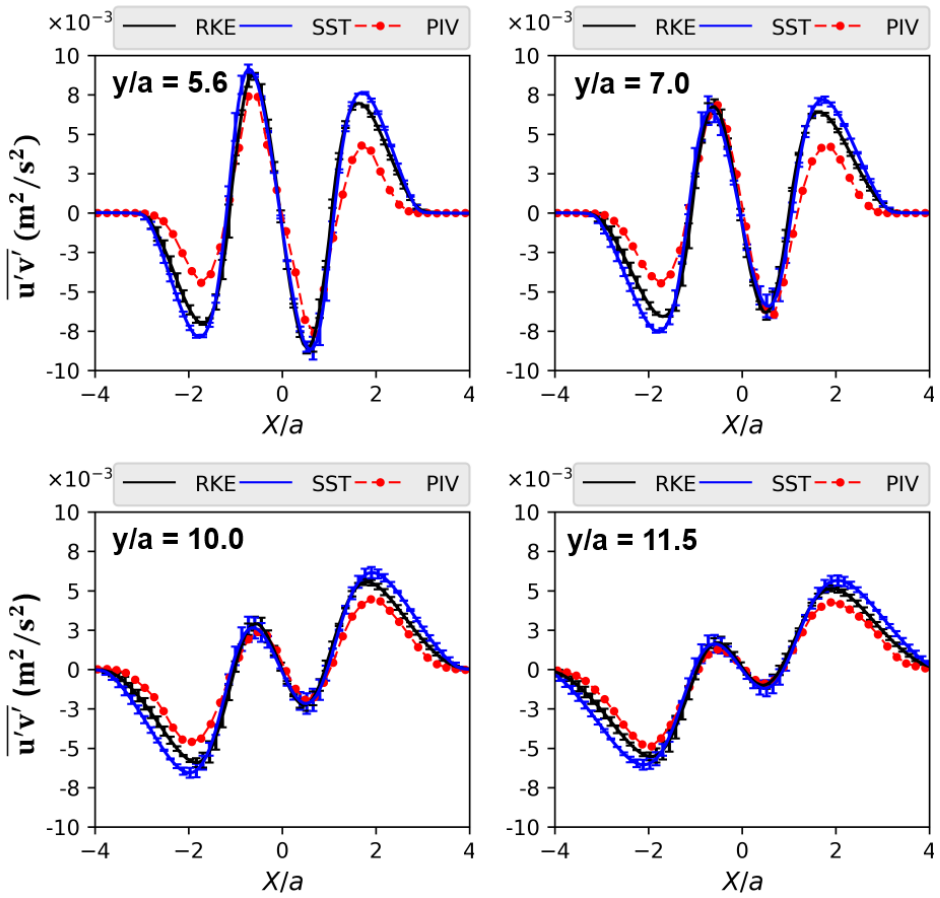

Figure 3.9: Reynolds Stress diagonal component $\overline{\mathbf{u'v'}}$ profile comparison at various locations. (RKE: realizable $k-\epsilon$; SST: SST $k-\omega$; PIV: Wang et al. [2]). Reprinted with permission from [28].

Figure 3.9 shows the off-diagonal component of the Reynolds stress $\overline{u'v'}$. Similar to the transverse velocity data, $\overline{u'v'}$ exhibits a higher discrepancy at y/a = 5.6 and 7. The numerical predictions agree better with the experimental data [2] at further downstream locations. Figure 3.10 shows the streamwise component of the Reynolds stress $\overline{u'u'}$. The steady-state RANS solutions show a consistent overprediction compared to the PIV data [2]. Figure 3.11 shows the Reynolds stress component of the transverse velocity fluctuations $\overline{v'v'}$. In contrast to $\overline{u'v'}$ and $\overline{u'u'}$ it can be observed that in figure 3.11 that the comparison shows a relatively large discrepancy with no-

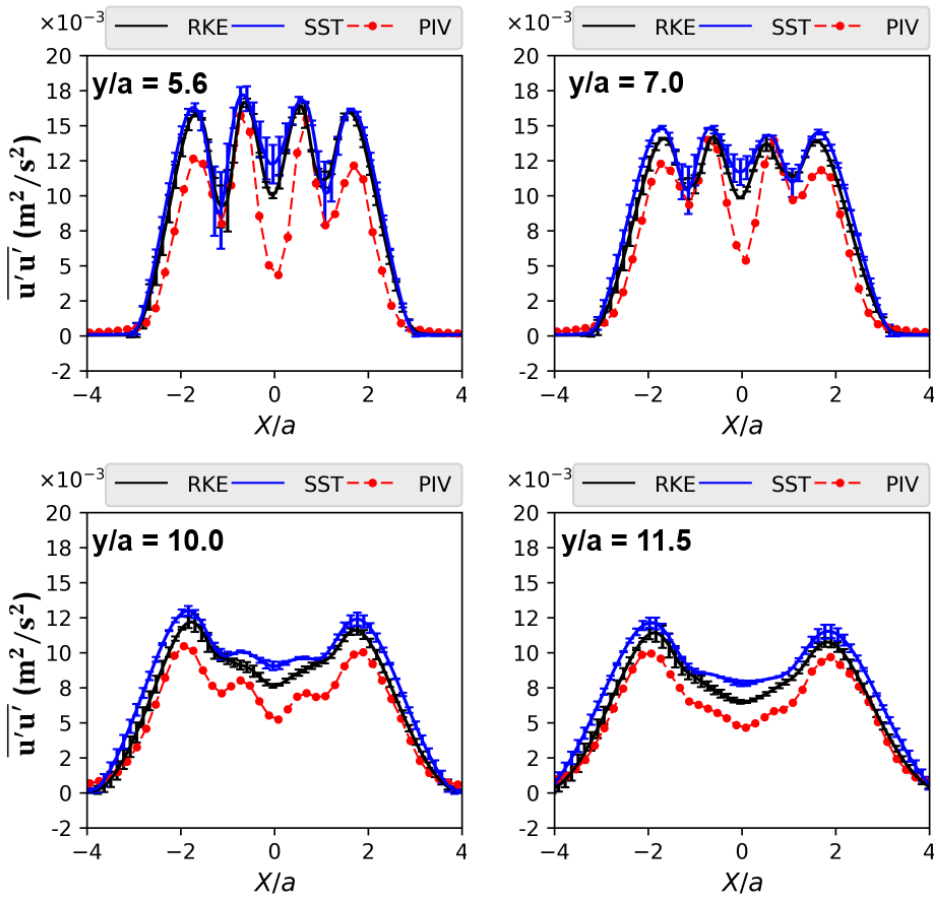

Figure 3.10: Reynolds stress off-diagonal component $\overline{\mathbf{u'u'}}$ profile comparison at various locations. (RKE: realizable $k-\epsilon$; SST: SST $k-\omega$; PIV: Wang et al. [2]). Reprinted with permission from [28].

ticeable overprediction of the PIV data [2]. One plausible explanation might be that the V-velocity magnitudes are small; this causes measurement uncertainties to become amplified. Thus, the $\overline{v'v'}$ component predictions show significant differences from the PIV data [2] compared with other Reynolds stress components. Another explanation for the Reynolds stress overprediction is the Boussinesq eddy assumption in the RANS models, which will be discussed in the next paragraph.

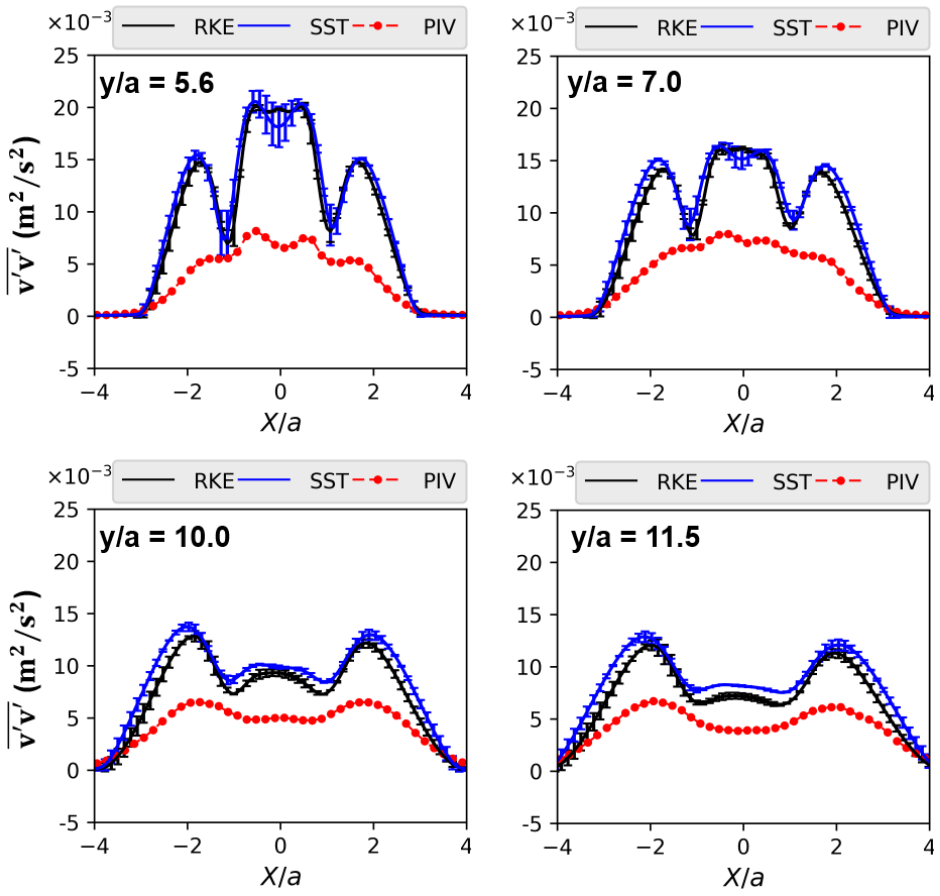

Figure 3.11: Reynolds stress off-diagonal component $\overline{\mathbf{v}'\mathbf{v}'}$ profile comparison at various locations. (RKE: realizable $k-\epsilon$; SST: SST $k-\omega$; PIV: Wang et al. [2]). Reprinted with permission from [28].

It is interesting to note that the comparison of the Reynolds stress with the PIV data [2] showed improvements at locations further downstream as shown in figures 3.9 to 3.11. The basis of the Reynolds stress modeling is the Boussinesq assumption, which supposes that the principal axes of the Reynolds stress tensor (τ_{ij}) are coincident with the mean strain-rate tensor $S_{ij} = \frac{1}{2}\left(\frac{\partial U_i}{\partial x_j} + \frac{\partial U_j}{\partial x_i}\right)$, at all points of turbulent flow [8]. This relation is analogous to Stokess postulate of laminar flow, where the coefficient of proportionality between τ_{ij} and S_{ij} is ν_t, i.e., the eddy viscosity. At locations closer to MP, e.g., y/a = 5.6 and 7, a strong interaction still exists between the two jets, which

exhibits multiscale, anisotropic turbulence phenomena. These phenomena may also lead to a sudden change in the mean strain rate and are typically difficult to predict via the Boussinesq eddy viscosity assumption. At the further downstream locations, the two jets are on the verge of merging into a single jet. The turbulence behaviors are well calibrated by the mainstream RANS models, such as the realizable $k-\epsilon$ and SST $k-\omega$. Thus, the Reynolds stress and V-velocity show a better agreement between the RANS models and the PIV data in the downstream region.

3.4 Boundary condition sensitivity study

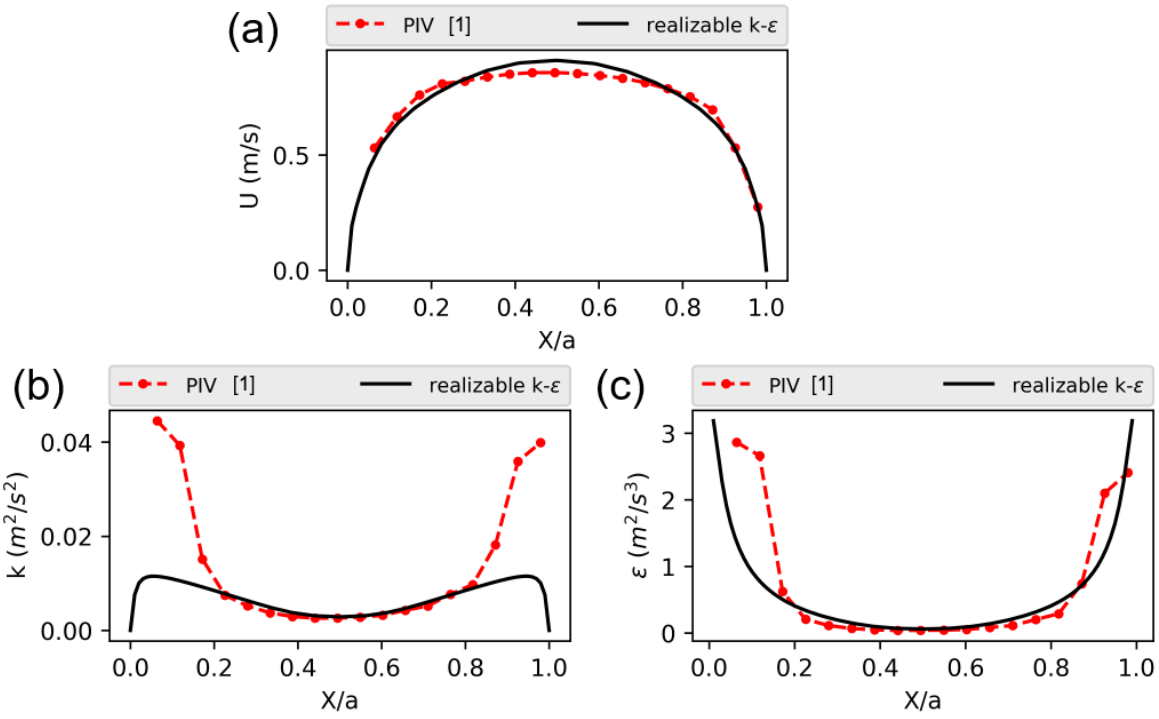

Figure 3.12: CFD and PIV comparison of channel flows. Reprinted with permission from [28].

In the previous section, it was shown that the steady-state RANS solutions from the realizable $k-\epsilon$ and the SST $k-\omega$ models compared reasonably well with the PIV

measurements [2]. However, the validation process was based on the inlet boundary condition from the PIV measurements, and the PIV data would not always contain sufficient information, such as, the design of a parallel jets system with different geometries and mass flow rates using a CFD tool. Thus, the manner in which the choice of boundary conditions can affect the CFD prediction is worth investigating. This investigation would also be valuable in understanding the boundary condition sensitivity in parallel jet flows. The closest available option of boundary condition is the CFD solution for a fully developed channel that has the same cross-section as that of the jet geometry. In this section, the objective is to investigate the sensitivity of the inlet boundary condition to parallel jet flows. A channel flow simulation was performed us-

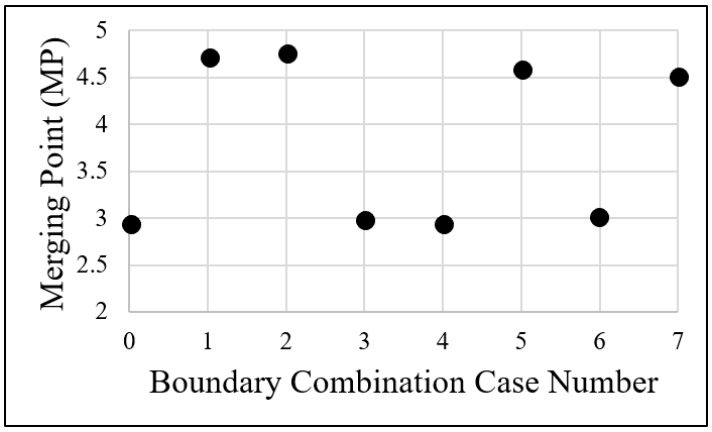

Figure 3.13: Boundary condition sensitivity plot in terms of merging point. Reprinted with permission from [28].

ing the realizable $k-\epsilon$. The channel was modeled geometrically with the same size as that of the jet cross-section. A comparison with the PIV data is shown in figure 3.12. Although U and ϵ CFD solutions are comparable to the PIV data [2], the turbulence kinetic energy, k, shows obvious underpredictions near the boundaries ($x/a = 0$ and

1.0).

To further investigate the impact of the inlet boundary conditions, the boundary conditions of U, k, and ϵ were divided into eight combinations by switching between PIV and CFD values at the inlets, as listed in table 3.6. Case number 0 is the case of the PIV boundary condition that was presented in the previous section. The MPs from all eight simulations are plotted in figure 3.13. It is noticeable that the MP varies within the range of 3a and 4.5a. Whenever the CFD boundary condition is used for the k_{inlet}, the MP spikes over 4.5, which is a 50% difference compared with the predicted MP from the PIV data [2]. As shown in figure 3.13, Cases 0, 3, 4, and 6 presented an MP of approximately 3, for which the inlet k from the PIV data was used. However, Cases 1, 2, 5, and 7 for which the inlet k from the realizable $k-\epsilon$ model was used shows an MP that is higher than 4.5. These results indicate that the boundary information of k, is an important factor for the prediction of the merging characteristic of parallel jet flows. To ensure that CFD simulations will predict the flow characteristics reasonably well, one should select the correct boundary conditions for the mean velocity as well as for the turbulent kinetic energy profile. Because the turbulent kinetic energy is closely related to the turbulent intensity of flow, this part of the current study also indicates that in twin-jet flow, the turbulence intensity change could significantly vary the MP location.

Furthermore, the fact that the CFD solution showed lower k values than the PIV data [2] indicates that the CFD prediction for the channel flow may produce a less intense turbulent flow compared with that of the experimental conditions. The MP predictions for Cases 1, 2, 5, and 7 are further downstream compared with the MP predictions for Cases 0, 3, 4, and 6. This indicates that stronger turbulent flows in the

Case Number	U_{inlet}	k_{inlet}	ϵ_{inlet}	MP (a)
0	PIV	PIV	PIV	2.945
1	CFD	CFD	CFD	4.727
2	PIV	CFD	CFD	4.767
3	PIV	PIV	CFD	2.995
4	CFD	PIV	PIV	2.951
5	PIV	CFD	PIV	4.593
6	CFD	PIV	CFD	3.008
7	CFD	CFD	PIV	4.519

Table 3.6: Boundary condition sensitivity in terms of the merging point. Reprinted with permission from [28].

channel may cause the MP to be closer to the inlet of the jets. Thus, the MP in parallel jet flows may be altered by controlling the turbulence intensity of jets in a channel. A more intense turbulent flow in jet inlets could cause in the MP to shift toward further upstream locations owing to rapid mixing.

4. PARTIALLY AVERAGED NAVIER-STOKES MODELS *

4.1 Partially averaged Navier-Stokes equations

The PANS method was proposed by Girimaji [31]. The purpose was to build a bridging method that enables a smooth transition between RANS and direct numerical simulations (DNS). In contrast to RANS, which uses the Reynolds averaging methodology, PANS applies a partial averaging concept to the Navier-Stokes equations.

In URANS models, the averaging procedure describes the velocity in terms of the mean and fluctuating components. The partial averaging procedure is similar to LES, which uses a generalized homogeneous filter [32]. In this context, the partial averaging operator or filtering operator is "$\langle\rangle$", the filtering process decomposes the velocity into resolved and unresolved parts:

$$u_i = \langle u_i \rangle + \hat{u_i}; \quad \langle u_i \rangle = \overline{u}_i \tag{4.1}$$

where $\langle u_i \rangle$ is the resolved velocity field, $\hat{u_i}$ is the residual velocity and $\langle \hat{u_i} \rangle \neq 0$. By applying the partial averaging operator/filter to the Navier-Stokes equations, the momentum equations for the resolved velocity field is presented as

$$\frac{\partial \overline{u}_i}{\partial t} + \rho \overline{u}_j \frac{\partial \overline{u}_i}{\partial x_j} = -\frac{\partial \langle P \rangle}{\partial x_j} + \frac{\partial}{\partial x_j}\left(\mu \frac{\partial \overline{u}_i}{\partial x_j} - \rho \tau(u_i, u_j)\right) \tag{4.2}$$

where $\tau(u_i, u_j)$ is the unresolved stress also called the sub-filter stress (SFS) term [32], which is defined in equation (4.3).

*Part of the content in this section is reprinted with permission from H. Li, N. K. Anand, and Y. A. Hassan, "Computational study of turbulent flow interaction between twin rectangular jets," *Int. J. Heat Mass Transf.,* vol. 119, pp. 752-767, Apr. 2018. Copyright [2018] by Elsevier

$$\tau(u_i, u_j) = \langle u_i u_j \rangle - \langle u_i \rangle \langle u_j \rangle \tag{4.3}$$

The modeling methodology for SFS varies with different turbulence models. The objective of this section is to describe the PANS model. LES models are briefly explained in Section 5.

Similar to the RANS models, in PANS, the modeling of SFS term was also based on the Boussinesq hypothesis as

$$-\rho\tau(\overline{u}_i, \overline{u}_j) = \mu_u \left(\frac{\partial \overline{u}_i}{\partial x_j} + \frac{\partial \overline{u}_j}{\partial x_i} \right) - \frac{2}{3}\rho k_u \delta_{ij} \tag{4.4}$$

where μ_u is called the unresolved eddy viscosity, and k_u is the unresolved turbulent kinetic energy.

In Girimaji [32], the PANS $k-\epsilon$ models are based on RANS standard $k-\epsilon$ paradigm by introducing the ratio of unresolved-to-total turbulent kinetic energy f_k and unresolved-to-total dissipation rate f_ϵ.

$$f_k = \frac{k_u}{k}, \quad f_\epsilon = \frac{\epsilon_u}{\epsilon} \tag{4.5}$$

By applying the above relations to the RANS standard $k-\epsilon$ equations, we obtain

$$\rho \frac{\partial}{\partial t}(k_u) + \rho \overline{u}_i \frac{\partial}{\partial x_i}(k_u) = f_k \left[\frac{\partial}{\partial x_j} \left((\mu + \frac{\mu_t}{\sigma_k}) \frac{\partial k}{\partial x_j} \right) + P_k - \rho\epsilon \right] \tag{4.6}$$

where the terms in square brackets "[ ]" are from the right-hand side of the standard $k-\epsilon$ in equation (3.8). With $f_k = 1$, we have $k_u = k$, thus equation (4.6) will be identical to equation (3.8), and therefore, the PANS $k-\epsilon$ model will revert to the

RANS standard $k-\epsilon$. When $f_k = 0$, according to equations (4.5) and (4.6), $k = 0$; thus, the turbulence model part will disappear which means that the solver will solve the momentum equation directly (DNS).

Based on the zero-transport model (ZTM), the final model equations for the unresolved turbulent kinetic energy k_u is

$$\rho\frac{\partial}{\partial t}(k_u) + \rho\overline{u}_i\frac{\partial}{\partial x_i}(k_u) = \frac{\partial}{\partial x_j}\left[\left(\mu + \frac{\mu_u}{\sigma_{ku}}\right)\frac{\partial k_u}{\partial x_j}\right] + P_u - \rho\epsilon_u \tag{4.7}$$

and unresolved turbulent dissipation rate ϵ_u is

$$\rho\frac{\partial}{\partial t}(\epsilon_u) + \rho\overline{u}_i\frac{\partial}{\partial x_i}(\epsilon_u) = \frac{\partial}{\partial x_j}\left[\left(\mu + \frac{\mu_u}{\sigma_{\epsilon u}}\right)\frac{\partial \epsilon_u}{\partial x_j}\right] + C_{\epsilon 1}\frac{\epsilon_u}{k_u}P_u - C^*_{\epsilon 2}\frac{\epsilon_u^2}{k_u}\rho \tag{4.8}$$

The two equations above show similarity to the standard $k-\epsilon$ equations. In the present work, the PANS $k-\epsilon$ closure coefficients are based on zero transport model (ZTM), which assumes that the resolved fluctuations do not contribute to the net transport of unresolved turbulent kinetic energy [32]. In contrast to standard $k-\epsilon$ model, the closure coefficients are:

$$\sigma_{ku} = \sigma_k\frac{f_k^2}{f_\epsilon}, \quad \sigma_{\epsilon u} = \sigma_\epsilon\frac{f_k^2}{f_\epsilon}$$

$$C^*_{\epsilon 2} = C_{\epsilon 1} + \frac{f_k}{f_\epsilon}(C_{\epsilon 2} - C_{\epsilon 1})$$

where σ_k, σ_ϵ, $C_{\epsilon 1}$ and $C_{\epsilon 2}$ are the closure coefficients from the standard $k-\epsilon$ model, which are listed in table 3.1. In reference [31], Girimaji suggested that f_k can be calculated through the following relation:

$$f_k = \frac{1}{\sqrt{C_\mu}} \left(\frac{\Delta}{\Lambda} \right)^{2/3} \tag{4.9}$$

where $C_\mu = 0.09$, and $\Lambda = k^{1.5}/\epsilon$ is the Taylor scale of turbulence [33].

PANS models have been investigated by several researchers, who presented their advantages in capturing unsteady phenomena with balanced computational resources. Akula et al. [34] investigated the PANS $k - \omega$ model in order to compare it with the LES in three-dimensional lid-driven cavity flows. The results from the PANS model with a coarser grid showed a better representation of the desired physics compared to the results of LES. Their subsequent research showed that the PANS simulation captured the vortex flow and small-scale behavior at a reasonable computational cost. Chaou et al. [35] demonstrated that the PANS $\zeta - f$ model in a channel flow is valid by showing its ability to capture the near-wall Reynolds stress anisotropy. Basara et al. [36] tested a near-wall formulation of a PANS four-equation model and compared the results with a DNS data. The results showed a good agreement in the mean flow and RMS velocity fluctuation, and they are invariant of the Reynolds stress anisotropy.

In this study, the PANS $k - \epsilon$ model was used for the PANS simulations and is referred to as PANS for the rest of this dissertation.

4.2 Simulation setups

For PANS simulations, the linear upwind stabilized transport (LUST) [37] scheme is applied to the momentum equations. LUST is a fixed blend between linear upwind and centered linear schemes with the intention of controlling numerical diffusion and grid scale oscillations. The PISO algorithm is used to couple pressure and velocity. The solver from OpenFOAM used in PANS is ***pisoFoam***.

The simulation settings are summarized in table 4.1.

	Transient PANS
Pressure-velocity coupling	PISO
Spatial discretization scheme	LUST [37]
Temporal discretization scheme	2^{nd} order backward differencing
Convergence criteria	All residuals, 1×10^{-5}

Table 4.1: Summary of simulation settings.

4.2.1 Computational domain

In the PANS simulation, the geometry was the same as that of the steady-state RANS, shown in figure 3.1. The meshing strategy was the same as in RANS; two mesh sizes were used for comparison, and the cell numbers ranged from 9.6 million to 19 million, as listed in table 4.2.

	Smallest cell size (mm)	Total number of cells (millions)
Transient PANS Grid 2	0.3222	9.6
Transient PANS Grid 1	0.2320	19

Table 4.2: Mesh details for PANS.

4.2.2 Boundary conditions

Similar to RANS (Section 3), the outlet used the outflow (natural) boundary condition, and the no-slip boundary condition was used at the walls. The PANS boundary condition for jet inlets used the data from the PIV experiments [4]. However, since PANS is a transient simulation method, the PANS simulations utilized the instantaneous velocity profile from the PIV measurement data [4]. This was archived by using the ***timeVaryingMappedFixedValue*** function in OpenFOAM to interpolate the PIV data at each time step. The velocity profile at an arbitrary time is plotted in figure 4.1.

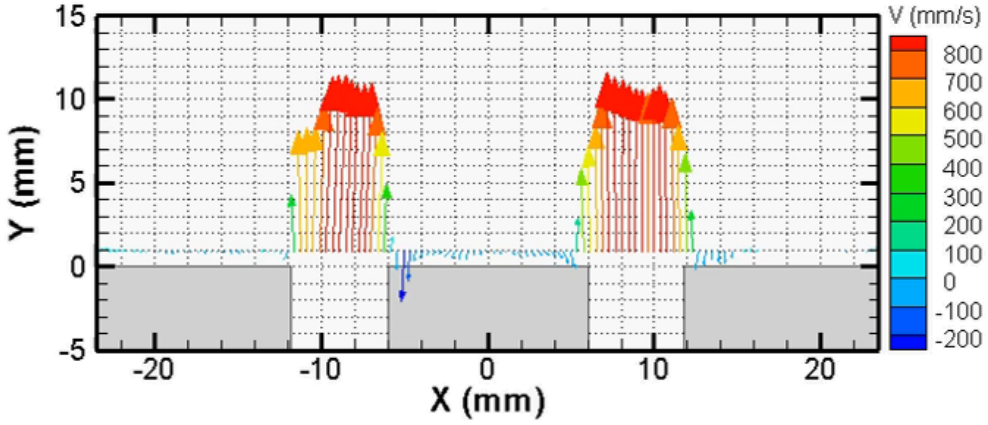

Figure 4.1: Inlet velocity vector for PANS at arbitrary time step from PIV data [4].

4.3 PANS and URANS models results

In this section, the results from PANS and URANS simulations are presented. The focus of this section is the PANS simulation results, whereas the URANS results is presented as a comparison case. The simulation settings for URANS are identical to

those of PANS.

4.3.1 Mean flow validation

The time-averaged data and the validation of the transient PANS simulation results are presented in this section. The time-averaged velocity field is referred to as mean flow in the rest of this section. URANS calculations are presented in comparison with the performance of PANS. For both PANS and URANS calculations, the mean quantities were collected over 55 flow-through-periods to ensure that enough data were used for averaging.

The MP data for different mesh sizes are listed in table 4.3. The difference in MP between two grids from the PANS simulation is 0.04a which is approximately 1% difference. Thus, the PANS grid 2 results is considered as grid-converged. The converged results of the PANS showed the MP to be 3.6a, with an error of 4.3% ($E_{MP,PANS} = 4.3\%$) compared to experiments [2], whereas the URANS results indicated an MP of 2.7a, with an error of 21.7%, ($E_{MP,URANS} = 21.7\%$). It is evident that the PANS solution is closer to the experimental results [2, 4].

Figure 4.2 shows the mean streamwise velocity profile from the PANS simulation at locations of y/a = 5.6 and y/a = 7. The results agree very well with those of PIV [2]. Figure 4.3 shows a comparison of the mean transverse velocity distribution predicted by the PANS simulation with the PIV data. The maximum discrepancy location is approximately $x/a = \pm 2.5$, which is the shear layer between the jets and the surroundings. In contrast, figures 4.4 and 4.5 show the URANS results of the streamwise and the transverse velocity profile, respectively. In the URANS streamwise velocity, the U-velocity show a higher value in the peak and a lower value in the valley, compared with the PIV data. Regarding the transverse velocity profile, the URANS

Simulation case	Number of cells (millions)	MP
PANS Grid 2	9.6	3.56a
PANS Grid 1	19	3.60a
URANS Grid 2	9.6	2.66a
URANS Grid 1	19	2.70a
PIV, Wang et al. [2]		3.45a
PIV, Lee et al. [4]		3.56a

Table 4.3: Merging point data from PANS and URANS.

result exhibits larger discrepancy compared with PANS predictions, nevertheless, the shape resembles that of PIV data.

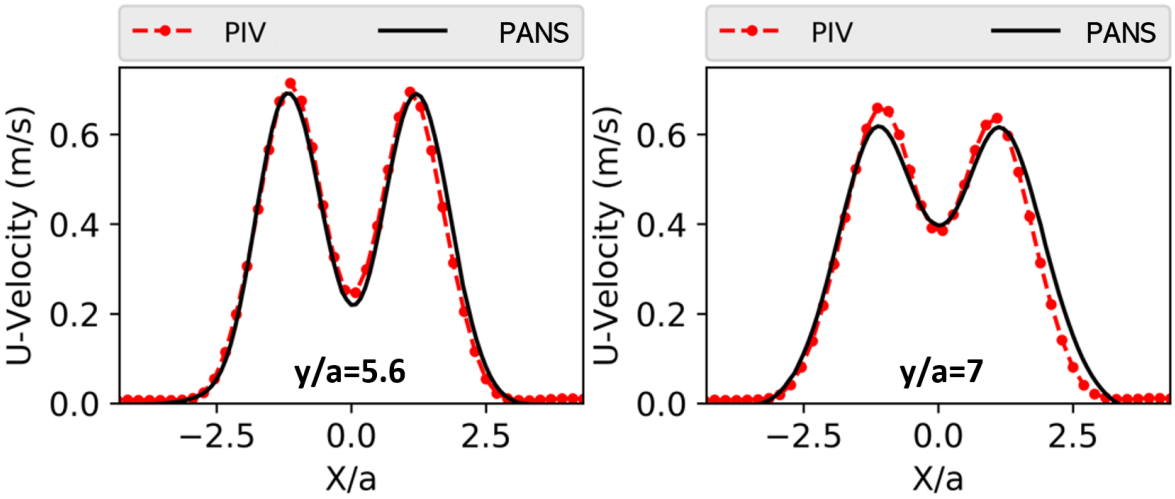

Figure 4.2: Mean streamwise velocity profile obtained from PANS simulation. Reprinted with permission from [28].

Figure 4.6 shows the Reynolds stress off-diagonal term $\overline{u'v'}$ from PANS and URANS

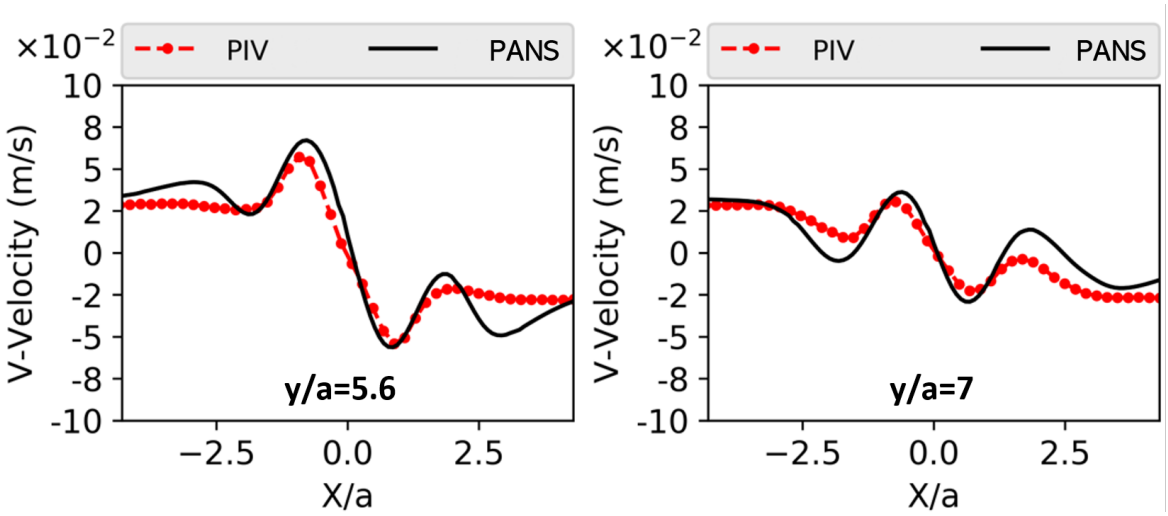

Figure 4.3: Mean transverse velocity profile obtained from PANS simulation. Reprinted with permission from [28].

in comparison with PIV data [2]. Note that the Reynolds stress term in figure 4.6 is computed from velocity statistics in a similar manner as the PIV experiments [2, 4]. The PANS results slightly overpredicted the Reynolds stress magnitude. The URANS data here show relatively large discrepancies, because of the nature of the Reynolds averaging process. The URANS model was intended to model Reynolds stress. The modeled Reynolds stress in URANS was represented by turbulence variables (k and ϵ), therefore the Reynolds stress components were not depicted in the flow statistics.

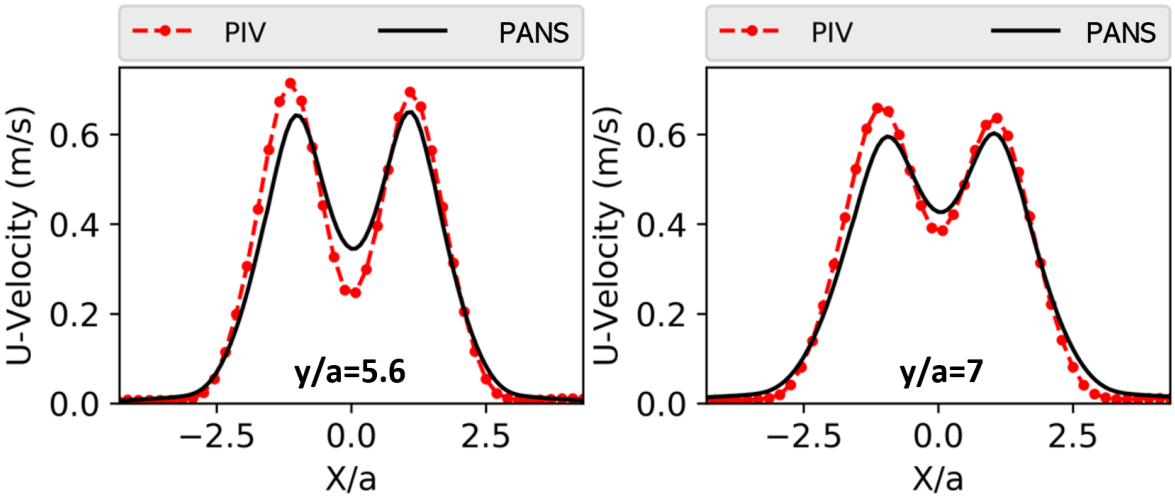

Figure 4.4: Mean streamwise velocity profile obtained from URANS simulation. Reprinted with permission from [28].

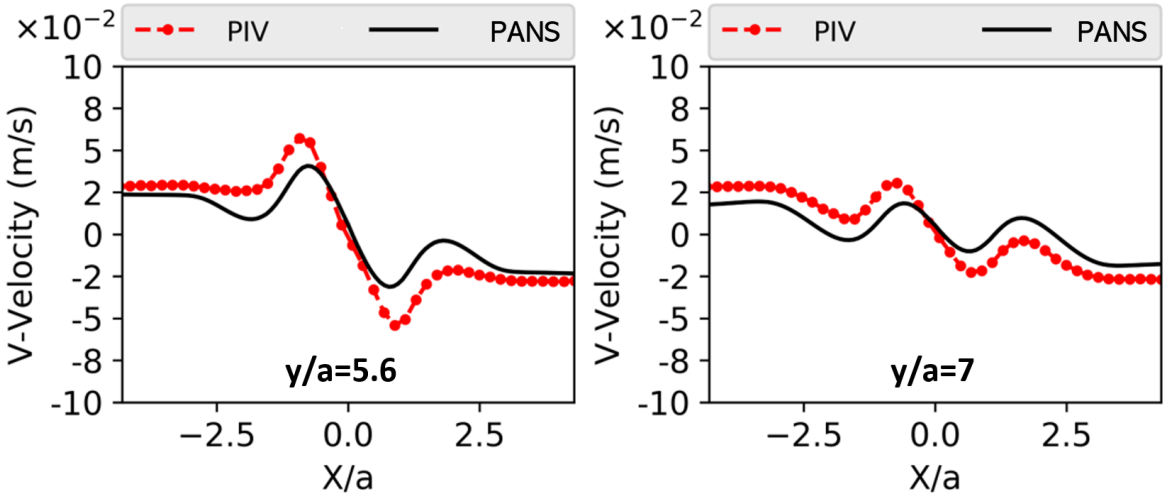

Figure 4.5: Mean transverse velocity profile obtained from URANS simulation. Reprinted with permission from [28].

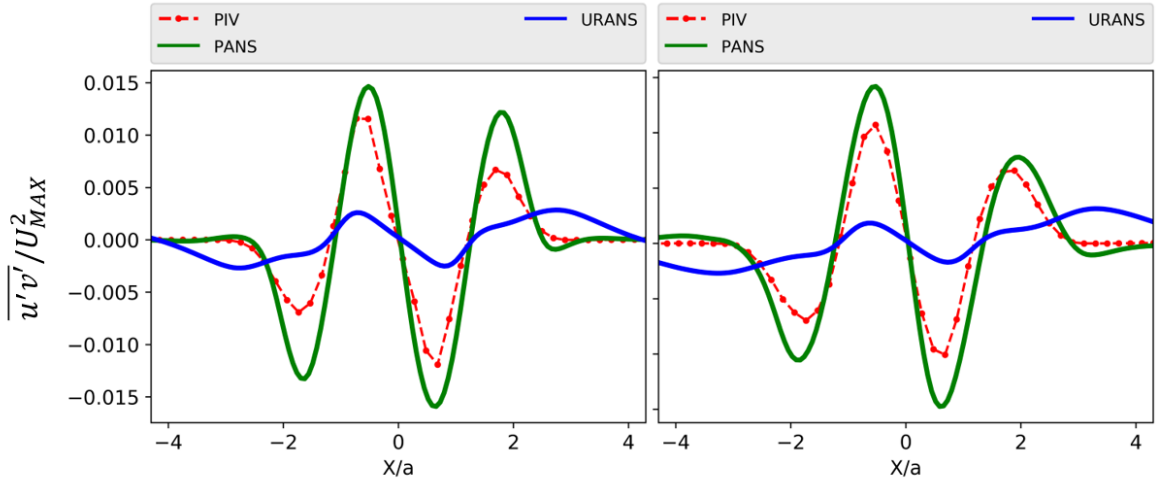

Figure 4.6: Reynolds stress off-diagonal component comparison plot of PANS, URANS and PIV. [2].

4.3.2 Instantaneous flow

The instantaneous streamwise velocities from PANS and URANS solutions at an arbitrary time step are shown in figure 4.7 to compare the two turbulent models. The plot showed that PANS solution exhibits a stronger unsteady behavior with a clearer interaction between the two jets. Figure 4.8 shows the instantaneous vorticity contour plot from the PANS and URANS solutions; the PANS solutions show clear vortex-shaped structures formed at the mixing layer between the jets and the surroundings. The PANS results showed its capability to capture more complex flow structures compared to URANS.

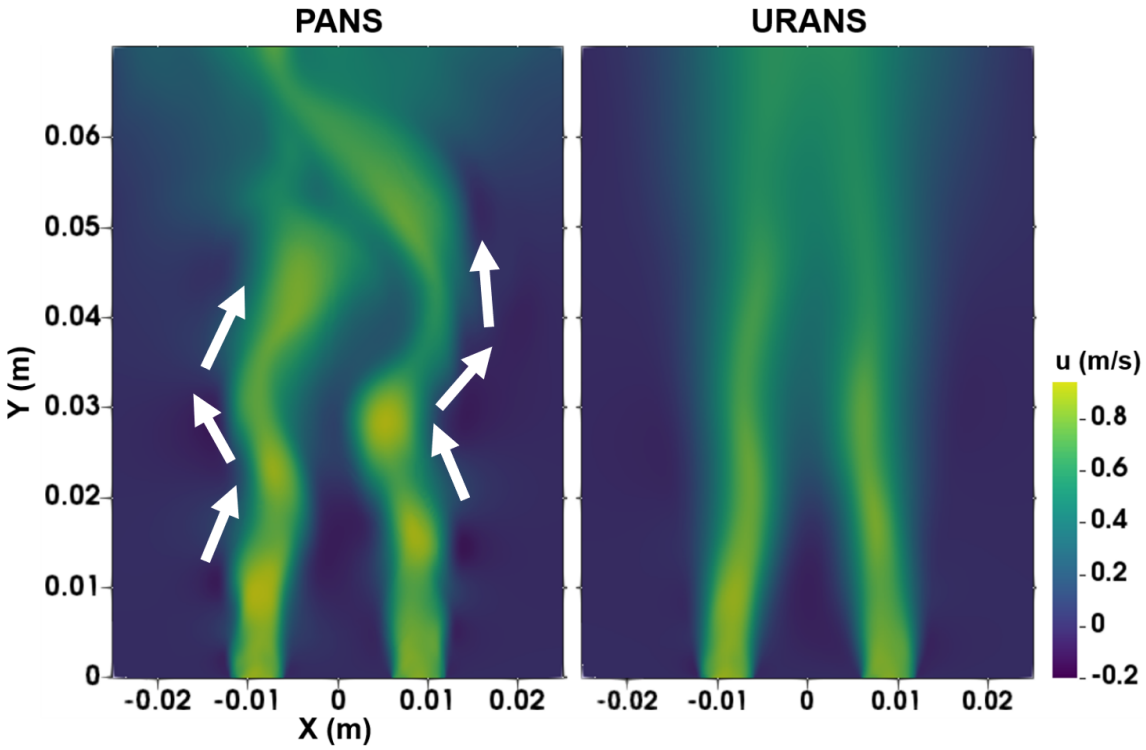

Figure 4.7: Instantaneous streamwise velocity contours for visual comparison: PANS simulation (left) and URANS simulation (right). Reprinted with permission from [28]

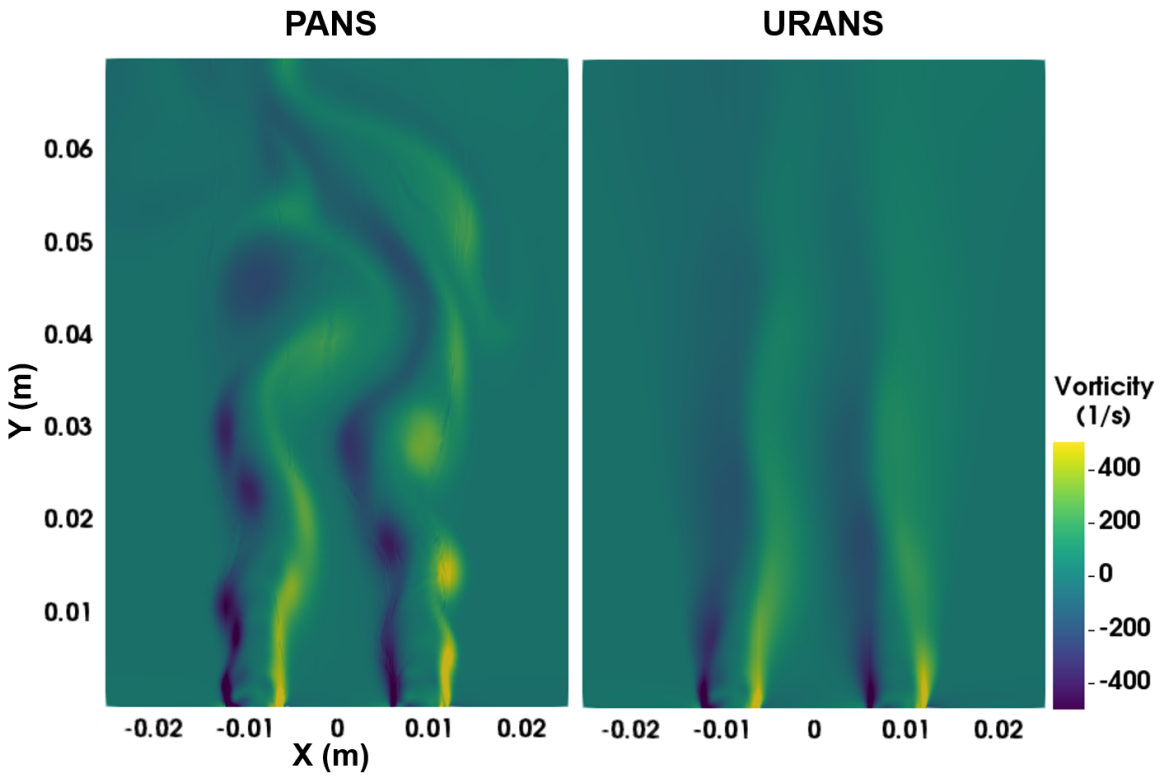

Figure 4.8: Instantaneous Z-vorticity contours for visual comparison: PANS simulation (left) and URANS simulation (right). Reprinted with permission from [28].

4.3.3 Spectral analysis

In the present study, spectral analysis was used to analyze the transient characteristics of turbulent flow. The methods used to analyze velocity data were fast Fourier transform (FFT) and power spectral density (PSD) calculations. Details of those methods can be found in Appendix B.

In order to analyze the spectral information, four sample locations were selected at various streamwise locations along the left mixing layer of the jet. The locations are marked in figure 4.9.

Figures 4.10 and 4.11 show the PSD of the turbulence kinetic energy signal from the URANS and PANS models at the aforementioned sample locations. Regarding the

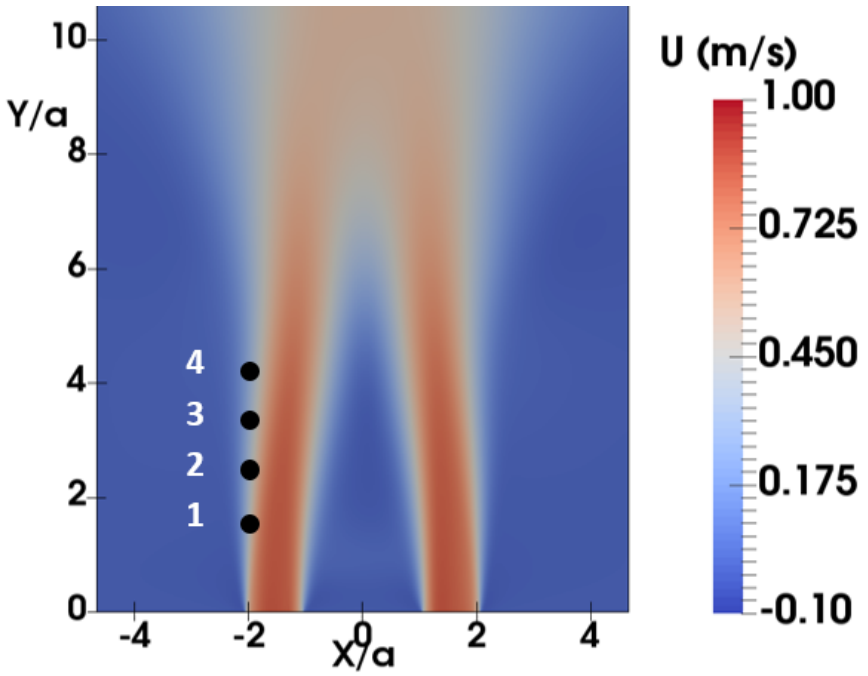

Figure 4.9: Mean streamwise velocity contour from PANS and the marked four sample locations for FFT analysis.

PANS simulation results, the energy is preserved at low frequencies, and the dissipation of energy mostly occurs at frequencies greater 100 Hz. Because the turbulence is anisotropic in the mixing layer, PSD plots may not always exhibit the energy cascading process following a theoretical -5/3 slope. The energy cascading process of a slope of -5/3 may be observed at sample location 4 for the frequency range of 10-40 Hz. The PSD starts to drop at a certain frequency (50 Hz), and the rate of PSD decay becomes lower at a frequency of approximately 250 Hz. For frequencies over 250 Hz, the rate at which the PSD decreases is fixed at a slope of -5/3, which may be attributed to the turbulence model. Thus, the PANS models are considered effective for power spectrum frequencies of up to 250 Hz. A similar shape is observed in the URANS results in figure 4.10; however, the rate of PSD decay is higher than that of PANS. The decaying energy process starts immediately at 1 Hz, following a -5/3 slope. The dissipation

process starts at approximately 30 Hz, and the modeled slope starts at approximately 100 Hz. In comparison, the PANS results presented a better power spectrum behavior than that of the URANS results.

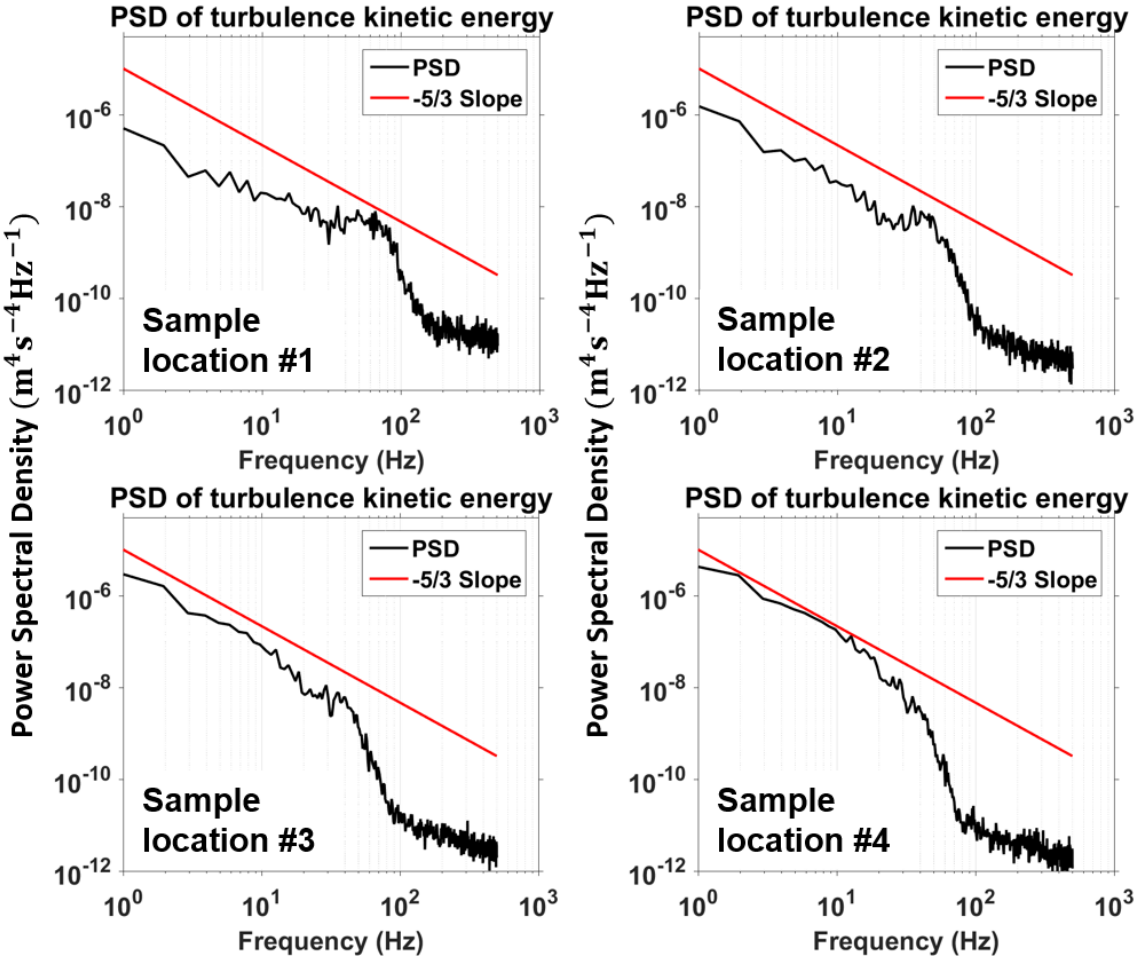

Figure 4.10: PSD on turbulent kinetic energy of probes from URANS. Reprinted with permission from [28].

The transverse velocity can represent the eddy passing in the mixing layer. Thus, the frequency of the transverse velocity signal can be viewed as the eddy shedding frequency of the jet mixing layer. Four sample locations are marked in figure 4.9; the fluctuation part of transverse velocity data is extracted for FFT analysis.

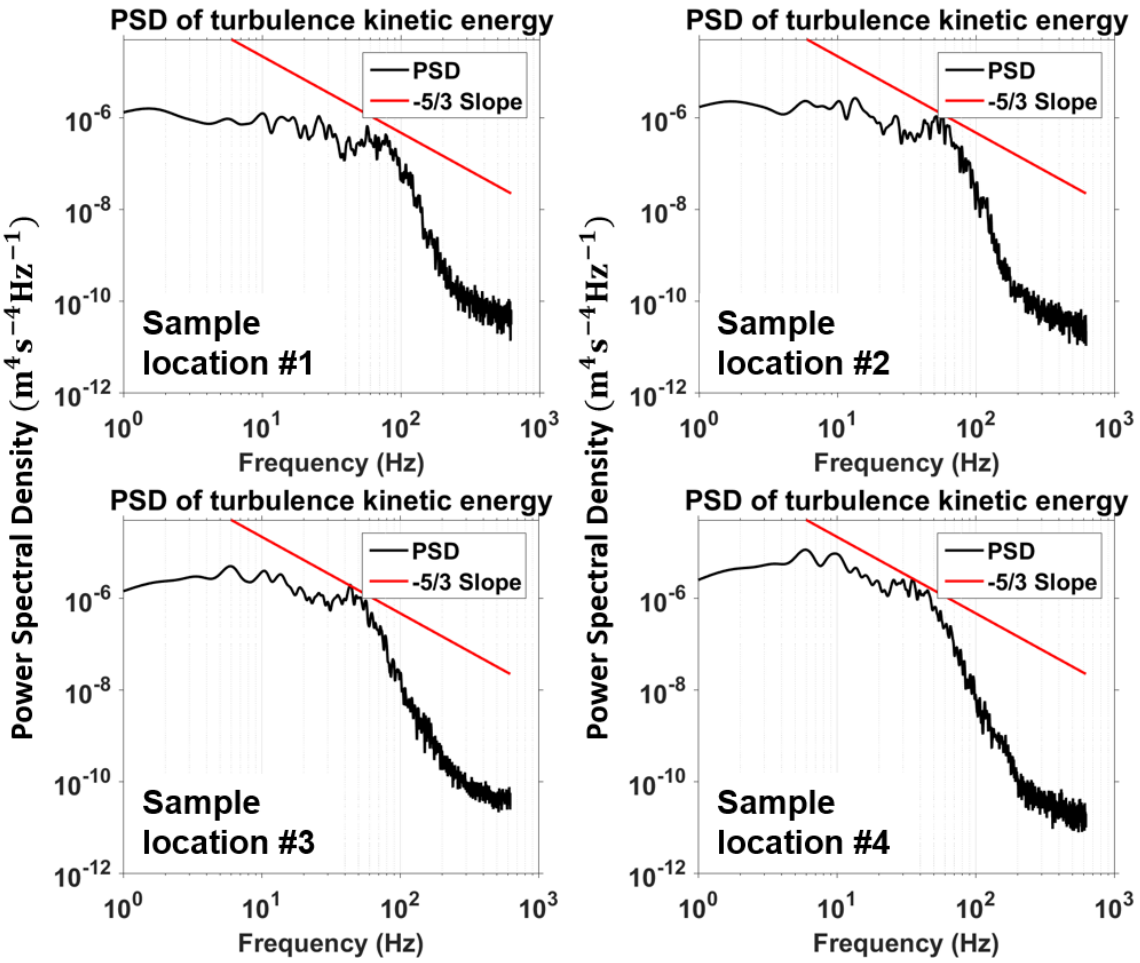

Figure 4.11: PSD on turbulent kinetic energy of probes from PANS. Reprinted with permission from [28].

Figures 4.12 and 4.13 illustrated the frequency information of the fluctuating transverse velocity at the aforementioned sample locations (figure 4.9). The PANS simulation shown on, sample locations 1 and 2 shows a dominant frequency at approximately 32 Hz (figure 4.12). In sample location 3, the leading frequency decreases to approximately 22 Hz, whereas the signal strength of approximately 32 Hz is still noticeably strong. The 32 Hz signal continues to decay up to sample location 4, where the 22 Hz signal becomes dominant. This can be explained by the following: as the vortex moves further downstream, the rotation speed slows down. In the study by Lee et al. [4], the

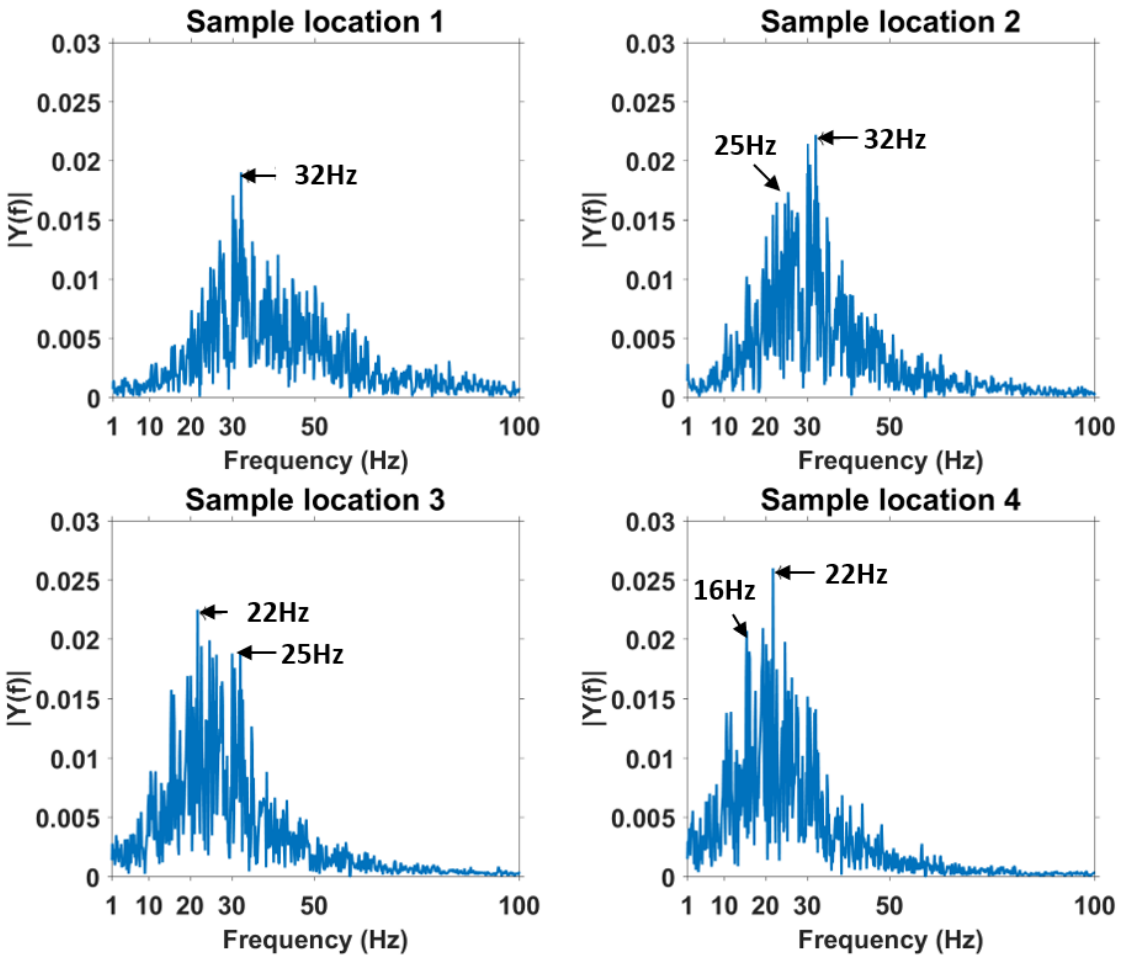

Figure 4.12: FFT of transverse velocity at four sample locations of PANS. Reprinted with permission from [28].

same analysis at those sample locations also revealed that the 32 Hz peak frequency decays to and 21 Hz. As a comparison case, the FFT analysis of the URANS simulation data at those same locations is shown in figure 4.13. At sample location 1, the URANS shows a peak frequency of approximately 35 Hz, which is close to the PANS result. However, at sample locations 2, 3, and 4, the peak frequency of the URANS solution is 15 Hz. Owing to the averaging nature of the RANS model, the peak frequency of the sample locations that are further downstream is lower than that of the PANS model.

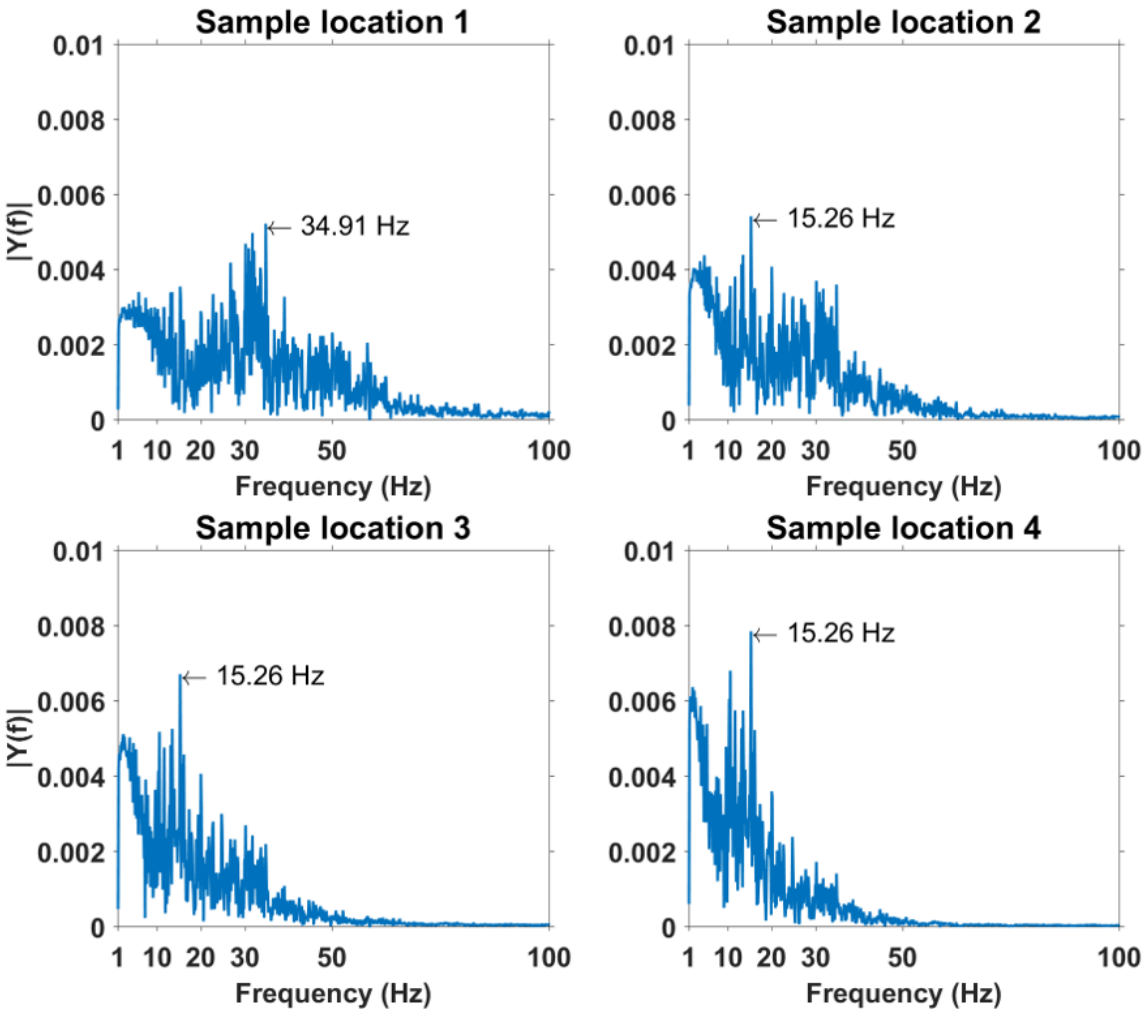

Figure 4.13: FFT of transverse velocity at four sample locations of URANS. Reprinted with permission from [28].

5.1 Large eddy simulations

LES is a computational techniquefor simulating turbulent flows in which large-scale turbulent structures are directly simulated, and small turbulent scales/eddies are modeled using sub-grid scale (SGS) models. LES is a computationally expensive method. The LES concepts were first proposed by Smagorinsky [38] for atmospheric air current simulations. The fundamental assumption of LES is that the largest eddies are directly affected by the geometry/boundary conditions and should be resolved. The small-scale turbulence contributes less to the turbulent flow; therefore, it is considered less critical. In LES concepts, the small-scale turbulence is nearly isotropic and possesses universal characteristics.

The concept of the LES model development is the filtering process. The filtering approach is similar to that of PANS as explained in the previous section. Various types of filters can be used in LES techniques; the simplest one is the volume average box filter as indicated in equation (5.1).

$$\overline{u}_i(\overrightarrow{x},t) = \frac{1}{\Delta^3}\int_{x-\frac{1}{2}\Delta x}^{x+\frac{1}{2}\Delta x}\int_{y-\frac{1}{2}\Delta y}^{y+\frac{1}{2}\Delta y}\int_{z-\frac{1}{2}\Delta z}^{z+\frac{1}{2}\Delta z} u_i(\overrightarrow{x},t)dxdydz \tag{5.1}$$

The filtered Navier-Stokes equation for LES is the same as that of PANS, which was given in equation (4.2) and described in the previous section (Section 4.1). The difference lies in the concept of the sub-filter stress (SFS) term, which is also called sub-grid scale (SGS) stress in LES studies [39, 40]. In LES, the SGS stress describes the small-scale eddies that are not significant to the turbulent flow. Therefore, LES

specifies a cutoff wave number for the dissipation range of the energy cascading process. In PANS, filter control parameter such as f_k and f_ϵ must be provided for a given simulation and can be used to control the extent of the resolved scale of simulation.

In LES, the modeling of SGS stress is usually based on the Boussinesq-type of approximation:

$$\tau(\overline{u}_i, \overline{u}_j) - \frac{1}{3}\tau_{kk}\delta_{ij} = -\nu_T \left(\frac{\partial \overline{u}_i}{\partial x_j} + \frac{\partial \overline{u}_j}{\partial x_i} \right) \tag{5.2}$$

where ν_{SGS} is SGS eddy viscosity, and $\frac{1}{2}\tau_{kk} = k_{SGS}$ is the SGS turbulent kinetic energy.

In the Smagorinsky model, which is the first proposed LES model, the eddy viscosity is modeled algebraically by assuming that the energy production and dissipation are in equilibrium, as indicated in equation (5.3).

$$\mu_{SGS} = \rho(C_s\Delta)^2\sqrt{2\overline{S}_{ij}\overline{S}_{ij}}, \quad where \quad \overline{S}_{ij} = \frac{1}{2}\left(\frac{\partial \overline{u}_i}{\partial x_j} + \frac{\partial \overline{u}_j}{\partial x_i} \right) \tag{5.3}$$

Here, C_s is the Smagorinsky constant and Δ is the grid spacing.

In the current work, the wall-adapting local eddy-viscosity (WALE) model is used for the calculation of eddy viscosity, which is defined as the follows:

$$\mu_{SGS} = \rho(C_w\Delta)^2 \frac{(S^d_{ij}S^d_{ij})^{3/2}}{(\overline{S}_{ij}\overline{S}_{ij})^{5/2} + (S^d_{ij}S^d_{ij})^{5/4}} \tag{5.4}$$

where S^d_{ij} denotes the traceless* symmetric part of the square of the velocity gradient tensor:

$$S^d_{ij} = \frac{1}{2}(\overline{g}^2_{ij} + \overline{g}^2_{ji}) - \frac{1}{3}\delta_{ij}\overline{g}_{kk}, \quad where \quad \overline{g}_{ij} = \frac{\partial \overline{u}_i}{\partial x_j}$$

*A traceless tensor is a tensor of which the summation of diagonal components is zero.

5.2 Simulation setups

The setting for LES is similar to that of PANS simulations (Section 4), the linear upwind stabilized transport (LUST) [37] scheme was applied to the momentum equations, and the second-order backward differencing scheme was used for the temporal term. The PISO algorithm was used to couple the pressure and velocity.

5.2.1 Computational domain

For LES cases, the computational domain was modified to improve the stability as shown in figure 5.1. At the top of the geometry, the flows were redirected to small channels to exit the domain. Because this LES used the boundary condition by OpenFOAM's turbulent flow generator, two channels were attached to the entrance location of the jets for the turbulence flow to develop. The computational mesh in LES focused on the converging region and merging region marked as LES zone in figure 5.2. In the present study, over 85% of cells were located within the LES zone. A view of the refined mesh is shown in figure 5.3. Over 99% of the cells were hexahedral, the remaining 1% were polyhedral cells due to local refinement.

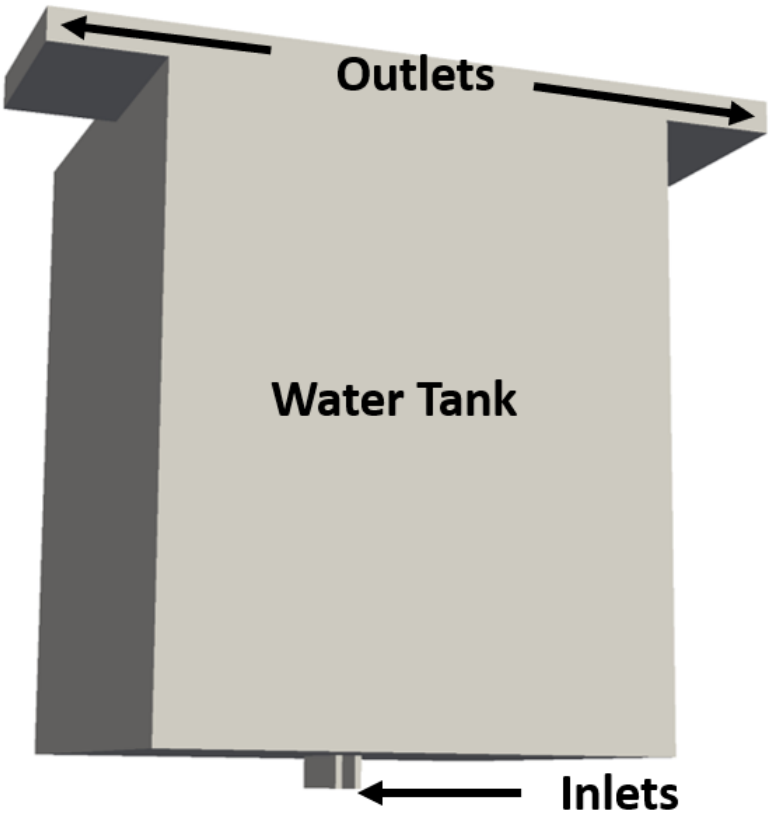

Figure 5.1: Computational domain for LES.

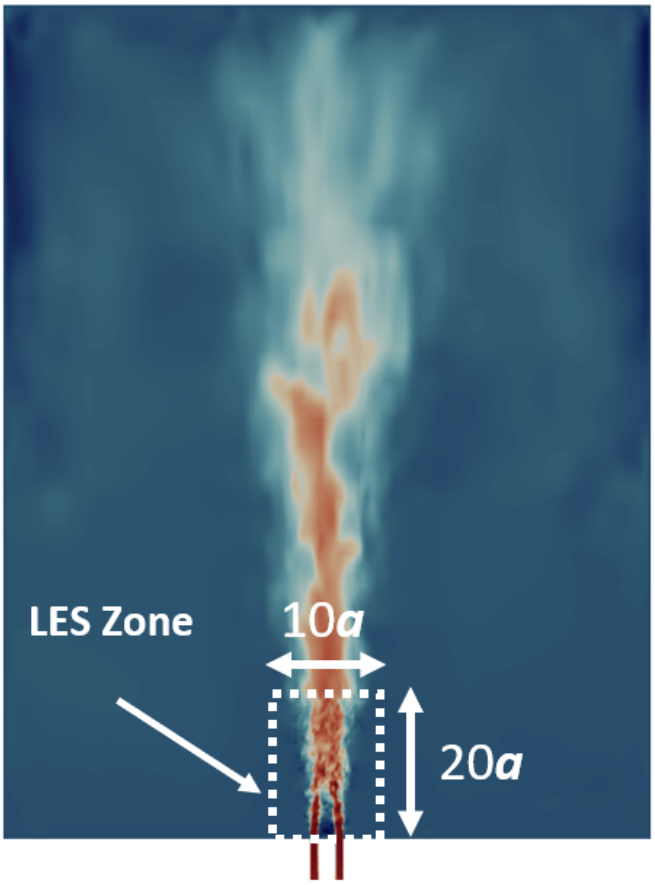

Figure 5.2: Illustration of mesh refinement for LES.

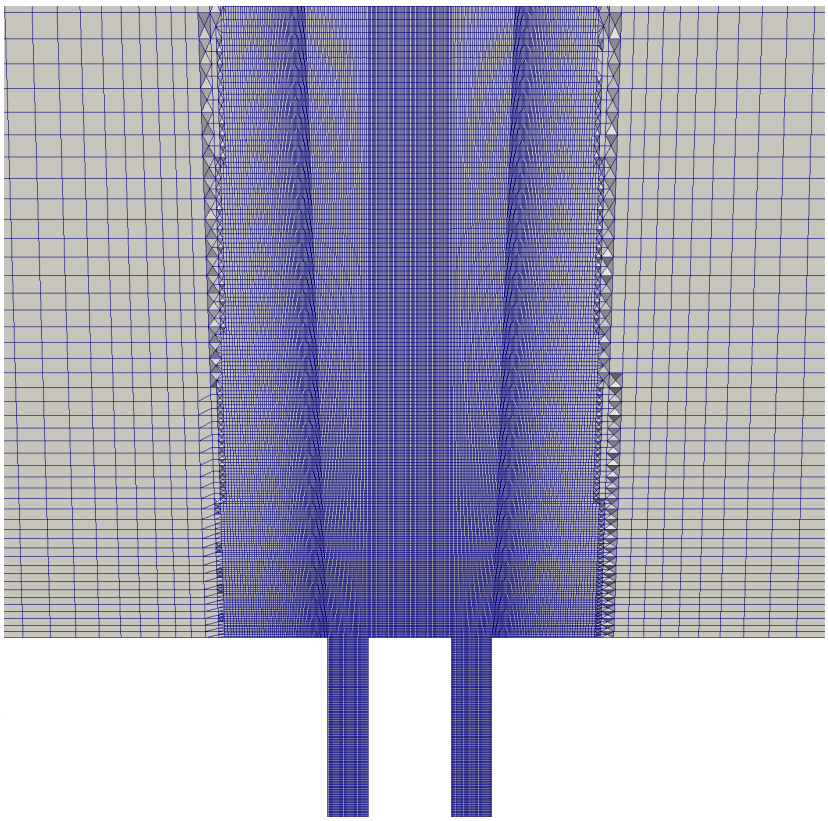

Figure 5.3: Clipped view of refined mesh for LES.

5.2.2 Boundary conditions

For LES in the present study, the simulation cases did not rely on experimental data. The boundary condition for the jets used the ***turbulentInlet*** function in OpenFOAM to generate the perturbed velocity for artificial turbulent flow. The mean streamwise velocity and RMS of streamwise velocity were measured at the entrance of the two jets to the water tank, which is the boundary condition location for PANS and RANS. Figure 5.4 shows the LES velocity compared to the PIV experiments [2, 4] at locations where the jets enter into the water tank. The mean velocity profile is comparable in both experiments. However, the RMS velocity profile exhibits a small discrepancy at the center between the two jets. LES seems to provide a slightly higher turbulent intensity between the two jets. This is discussed in the results section.

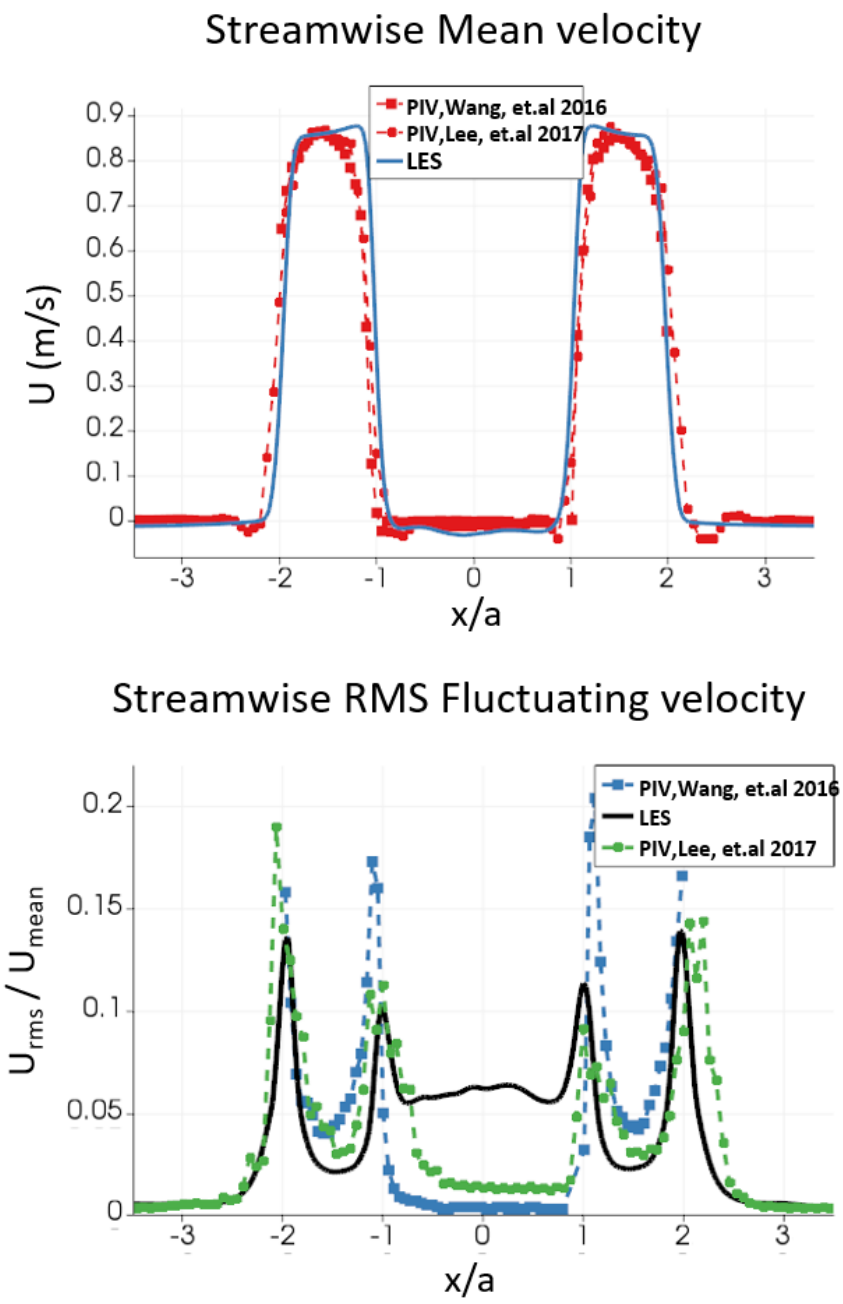

Figure 5.4: Mean velocity profile and RMS velocity profile comparison to PIV experiment. (Wang et al. [2] and Lee et al. [4].)

5.3 LES results

5.3.1 Mean flow validation

A grid convergence study for LES was performed based on merging point (MP) data. Figure 5.5 shows the MP for mesh sizes ranging from 13 million cells to 56 million cells. The MP difference between 32 million and 56 million cells was less than 1%. Therefore, the validation and post-processing analysis were based on the results from the 32 million cells.

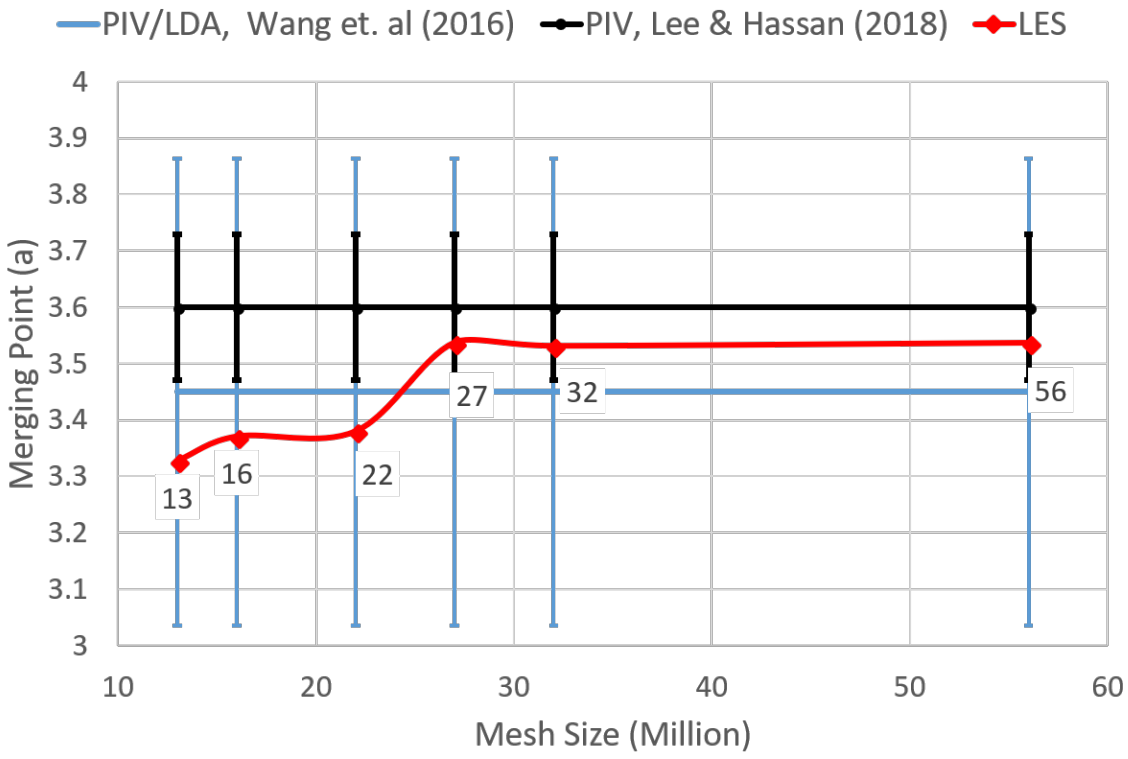

Figure 5.5: Grid convergence study on LES in terms of the merging point.

The time-averaged quantities were calculated after the jets reached the fully developed state. The time-averaged velocities were collected over 5 s that exceeds 50

times the large eddy turnover time. As stated earlier, one objective of this study is the validation of the LES model for twin-jet flow. Table 5.1 presents the MP data comparison against experimental data. The LES results indicate a good prediction of MP when compared with the experiments.

Figure 5.6 shows a comparison of time-averaged streamwise velocity profiles from the LES and PIV measurements by Wang et al. [2] at locations y/a = 5.6 and y/a = 7. The velocity profiles reasonably match with the experimental data. At x/a close to 0, the simulation indicates a slight overprediction. The figure seems to indicate that the PANS and RANS perform slightly better than the current LES; however, the LES is performed without relying on the PIV measurement data. As previously pointed out from the boundary condition sensitivity study, the twin-jet mixing behavior was sensitive to the boundary condition and particularly to turbulent intensity. Thus, the difference at x/a close to 0 was attributed to the variations in the turbulence boundary condition when compared to those in the PIV experiment.

Figure 5.7 shows a comparison of time-averaged transverse velocity profiles between LES and PIV at y = 5.6a and y = 7a. The comparison shows a reasonably good agreement at both locations.

Figure 5.8 shows the Reynolds stress off-diagonal term $\overline{u'v'}$ from LES compared to the PIV data [2]. Note that the Reynolds stress values in figure 5.8 were computed from velocity statistics in a similar manner as the PIV experiments [2,4]. The Reynolds stress profiles between jets agree reasonably well with PIV data [2]. At the jet interaction with the surroundings ($x/a = \pm 2$), the Reynolds stress shows a little overprediction.

Methods	Mesh Size (Cells)	MP (a)
Steady-state realizable k-ϵ	9.6 Million	2.95a
PANS standard k-ϵ	19 Million	3.6a
URANS standard k - ϵ	19 Million	2.70a
LES	32 Million	3.54a
LDA, Wang et al. [3]	-	1.72a - 3.45a
PIV, Wang et al. [2]	-	2.66a - 3.50a
PIV, Lee et al. [4]	-	3.48a - 3.74a

Table 5.1: Comparison of merging points.

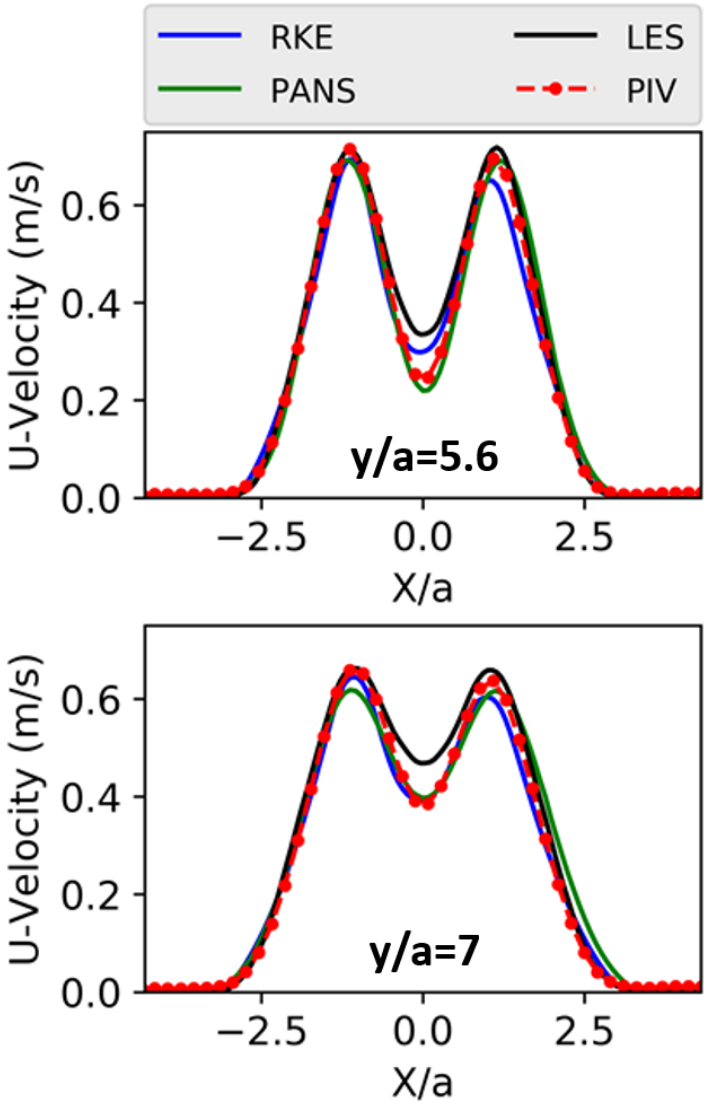

Figure 5.6: Comparison of streamwise mean velocity profiles. (y=5.6a and y=7a)

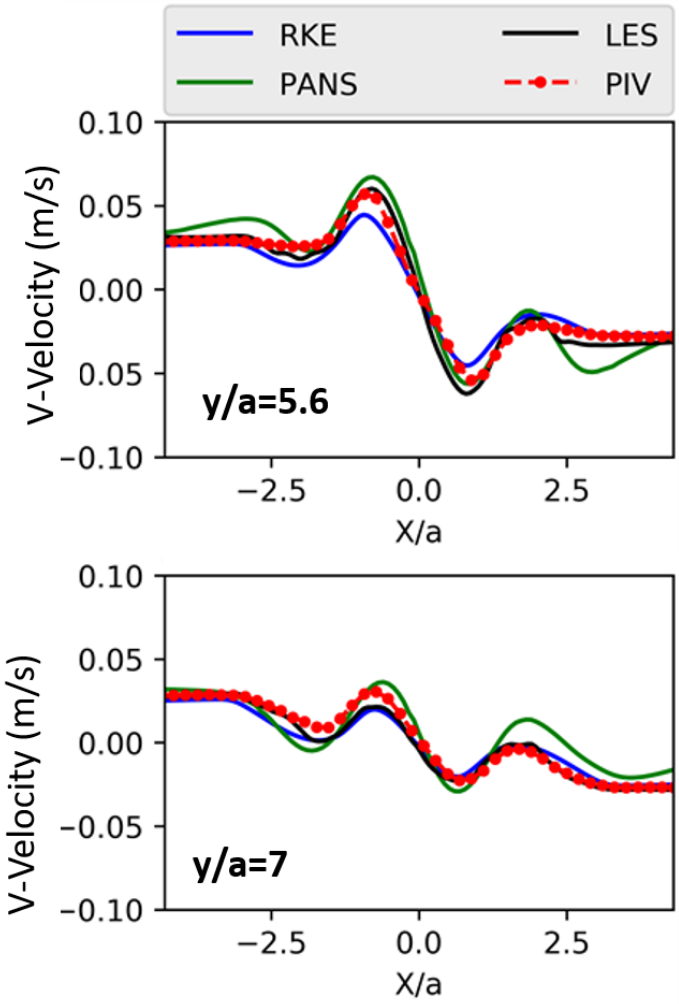

Figure 5.7: Comparison of transverse mean velocity profiles. (y=5.6a and y=7a)

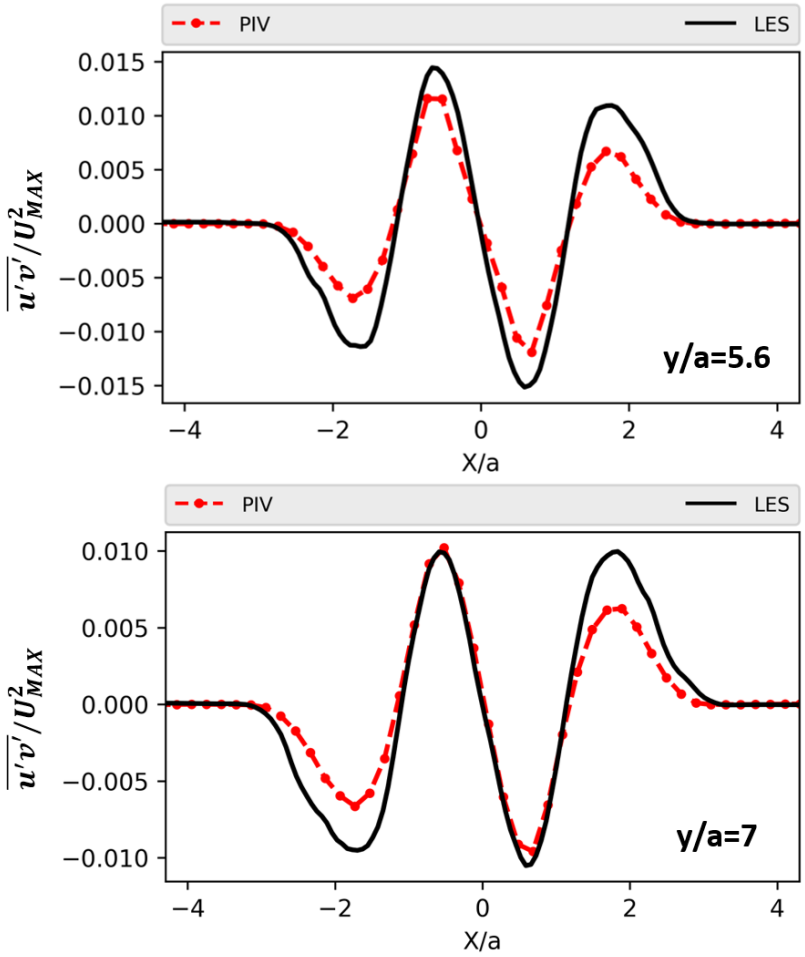

Figure 5.8: Comparison of diagonal components of Reynolds stress ($\overline{u'v'}/U_{MAX}^2$) profiles at y=5.6a and y=7a.

5.3.2 Vorticity

Because the benchmark PIV experiments [2,4] were based on two-dimensional plane measurements, only the rotations with respect to the z-direction were reported. The mean z-vorticity Ω_z can be viewed as the time-averaged rotation speed of fluid particles in the x-y plane. The mean z-vorticity was computed from the mean velocity field (U, V).

$$\Omega_z = \frac{\partial V}{\partial x} - \frac{\partial U}{\partial y} \tag{5.5}$$

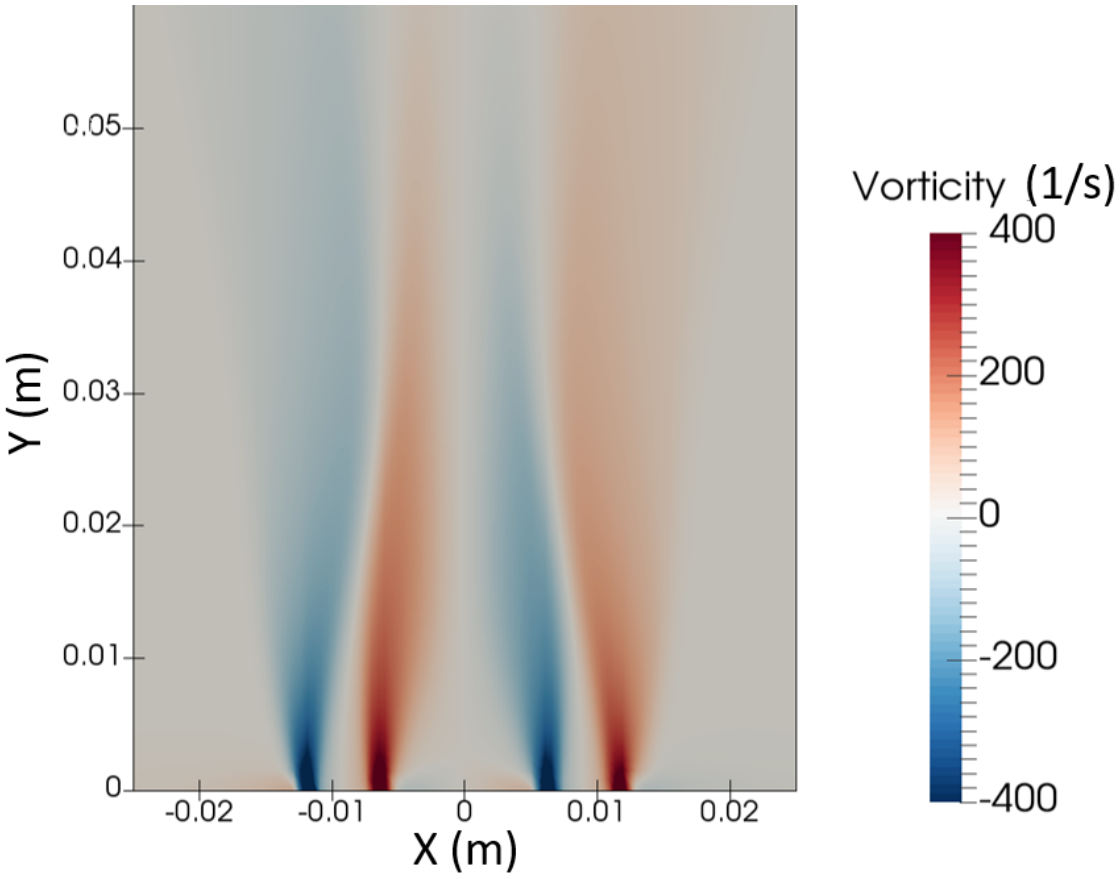

Figure 5.9: Mean vorticity distributions from RANS (realizable $k-\epsilon$).

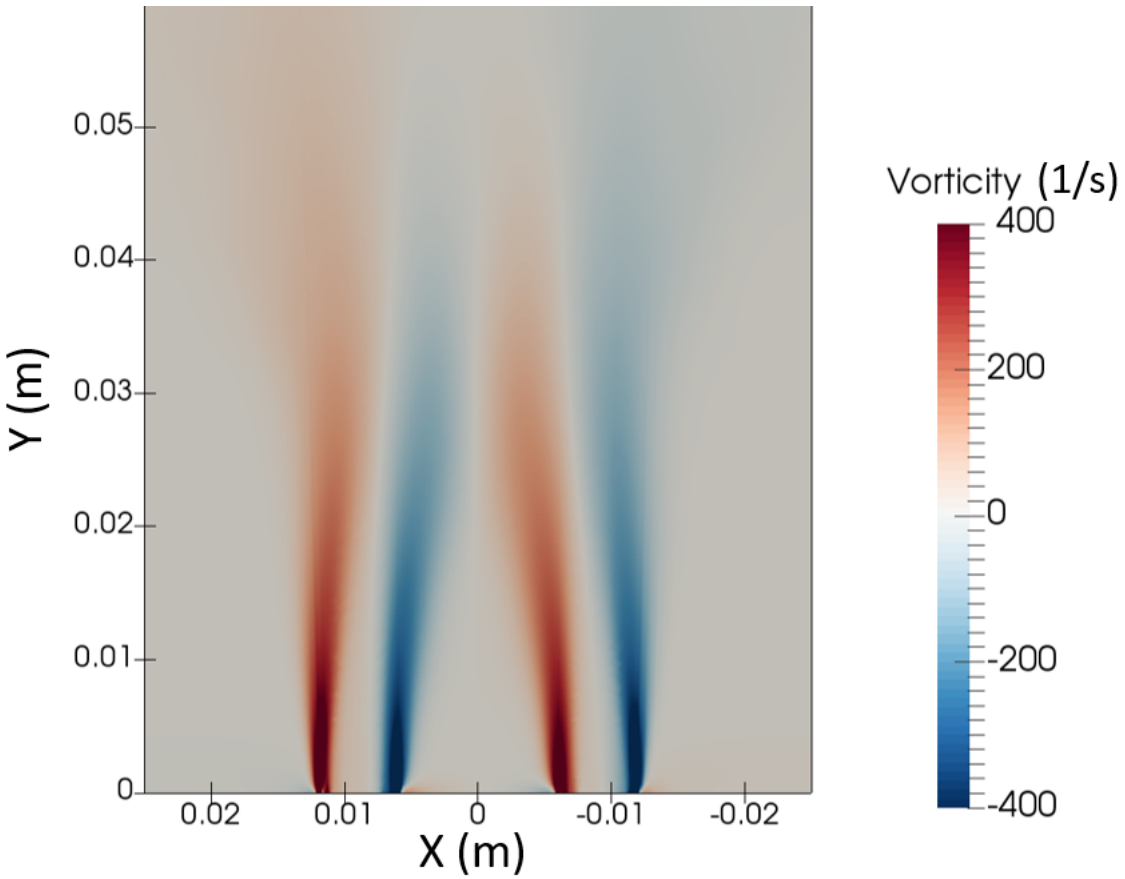

Figure 5.10: Mean vorticity distributions from PANS.

Figure 5.9 shows the mean z-vorticity contour from RANS (realizable $k-\epsilon$) simulations. Figure 5.10 illustrates the mean z-vorticity from PANS simulations. The mMean z-vorticity contour from LES is shown in figure 5.11. Three turbulence model results exhibited similar shape and magnitude, and the results are reasonably agree with those of Lee et al. [4]. However, LES results showed a closer agreement with experiments at near-jet inlet region. The vorticity contours in RANS and PANS exhibit a "dissipated" pattern.

Regarding three-dimensional vortex structures, the Q-criterion [41] is used. The Q-criterion is a scalar value defined by $Q = \frac{1}{2}\left(|\Omega_{ij}|^2 - |S_{ij}|^2\right)$, which can be interpreted as

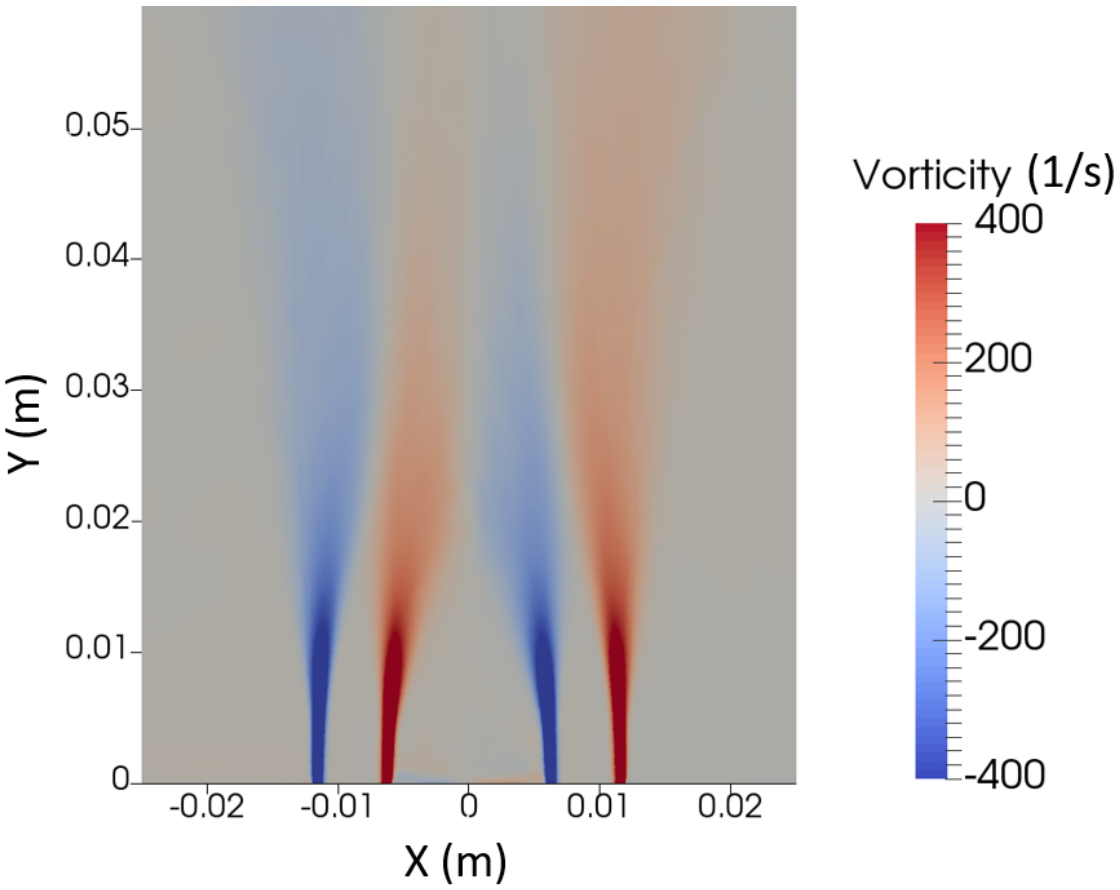

Figure 5.11: Mean vorticity distributions from LES.

vortex regions. For positive values, the flow is considered vorticity-dominant, whereas negative values mean that the flow is strain-dominated. Figure 5.12 shows the Q isosurface from the instantaneous flow of LES, and a tube-shaped vortex structure can be seen near the jet entrance. The tube-shaped vortex structure breaks into smaller scale of vortices as it moves further to the downstream direction. As a comparison, the Q isosurface from PANS simulation is shown in figure 5.13, a similar tube-shaped vortex is found near the jet entrance. Compared to LES, PANS simulation data exhibit less detail of the vortical structures.

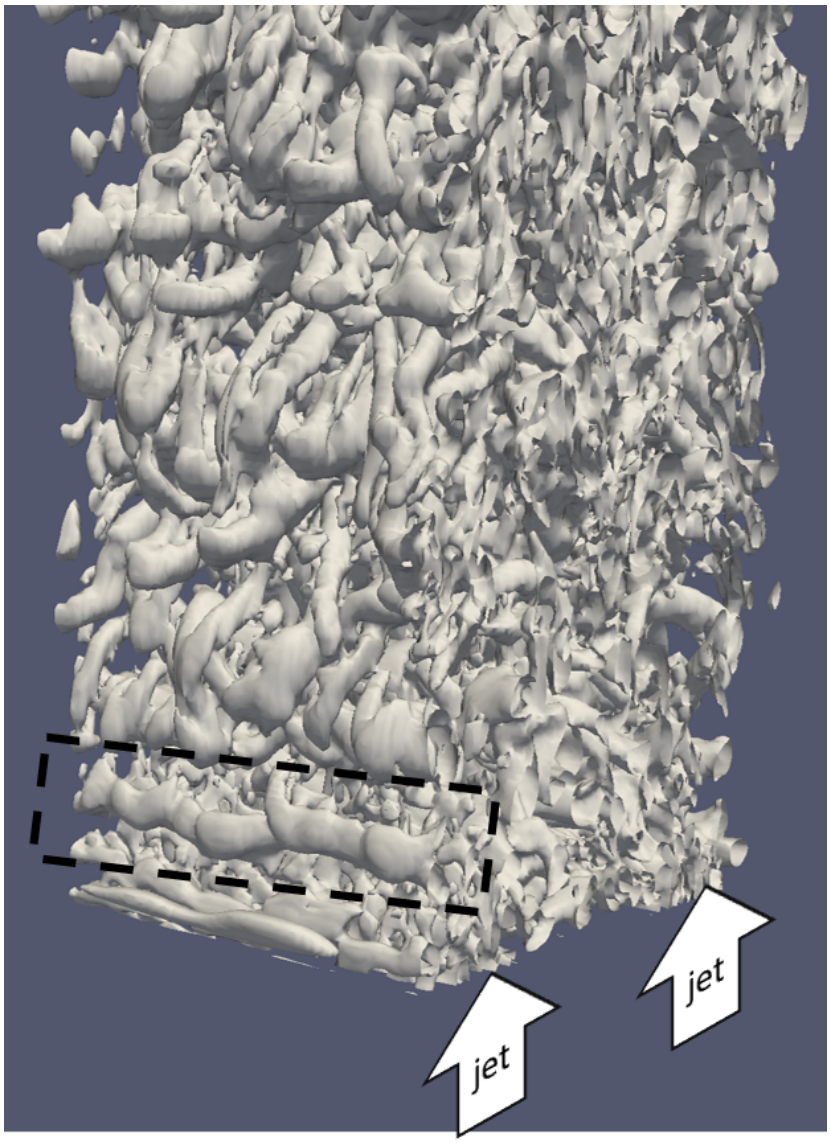

Figure 5.12: Instantaneous isosurface of **Q** of LES.

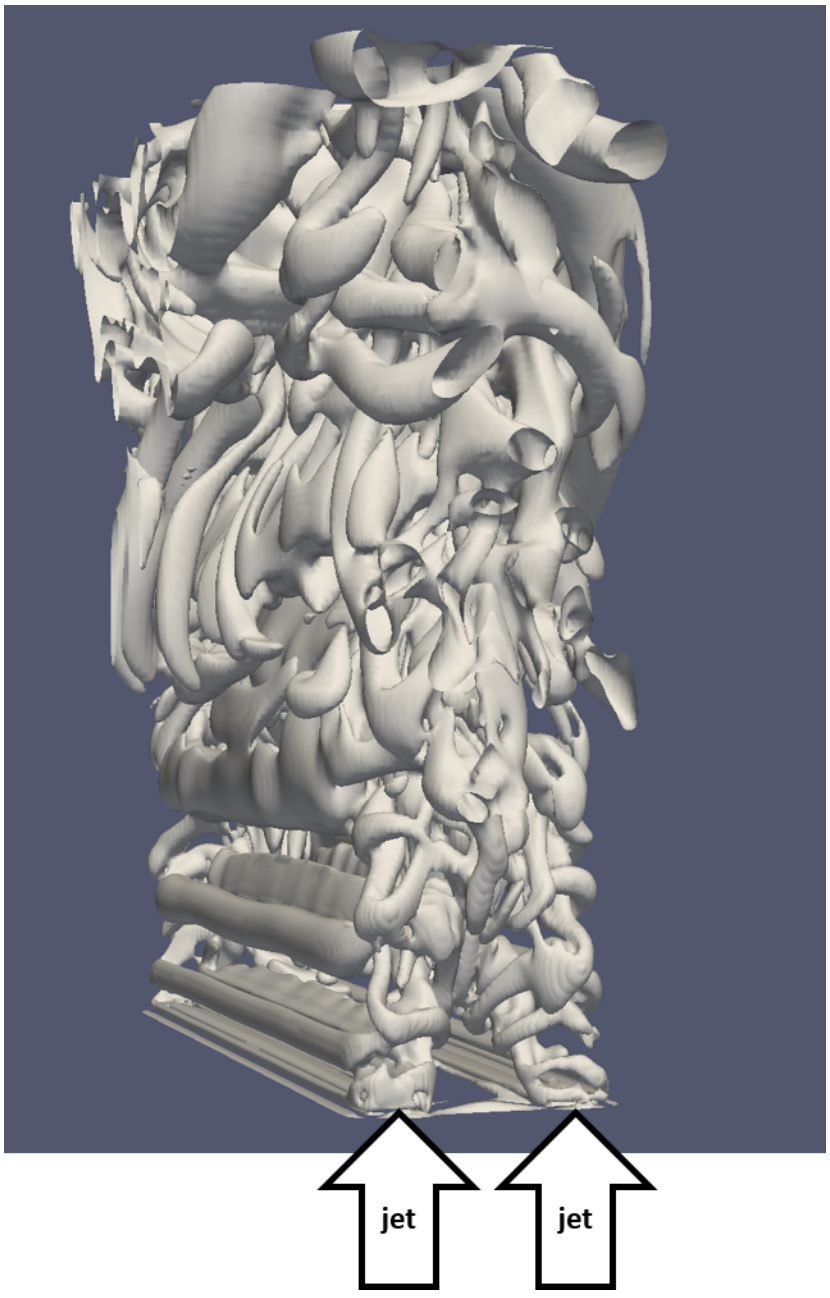

Figure 5.13: Instantaneous isosurface of **Q** of PANS simulations.

5.3.3 Spectral analysis

In this study, the spectral analysis was performed using FFT and PSD calculations, similar to those described in Section 4.3. Details of FFT and PSD can be found in Appendix B.

The transverse velocity fluctuation can represent the eddy shedding of the jet mixing layer between the jets and surrounding. In the benchmark experiment [4], velocity data were extracted from the shear mixing layer of the left jets. Same as in Section 4.1, four sample locations were selected on the shear mixing layer along the streamwise direction as shown in figure 4.9. The fluctuating part of the transverse velocity signal was extracted from the sample locations for the the FFT analysis. Figure 5.14 shows the peak frequency at each location in comparison with the PIV data reported by Lee et al. [4]. LES overpredicted the peak frequency by 25%. However, the four probes exhibited a similar frequency decay pattern when compared to the PIV data [4]. The decrease in the dominant frequency was due to the vortex pairing phenomenon as examined by Shim et al. [42] and Winant et al. [43].

The frequency difference compared to the experimental data was possibly due to the fact that the experiments were using centrifugal pumps with a 60 Hz pump frequency. Thus, the frequency data from experiments can be affected by the pump. In contrast to the PANS simulations that used instantaneous PIV data [4] as the boundary condition, in LES, the fluctuating boundary condition did not involve an explicitly enforced frequency from the PIV data.

Figure 5.15 shows the PSD of turbulence kinetic energy from four sample locations (locations marked in figure 4.9) using the Welch's method. The solid red lines represent the -5/3 slope as proposed by Kolmogorov to describe the energy cascade process,

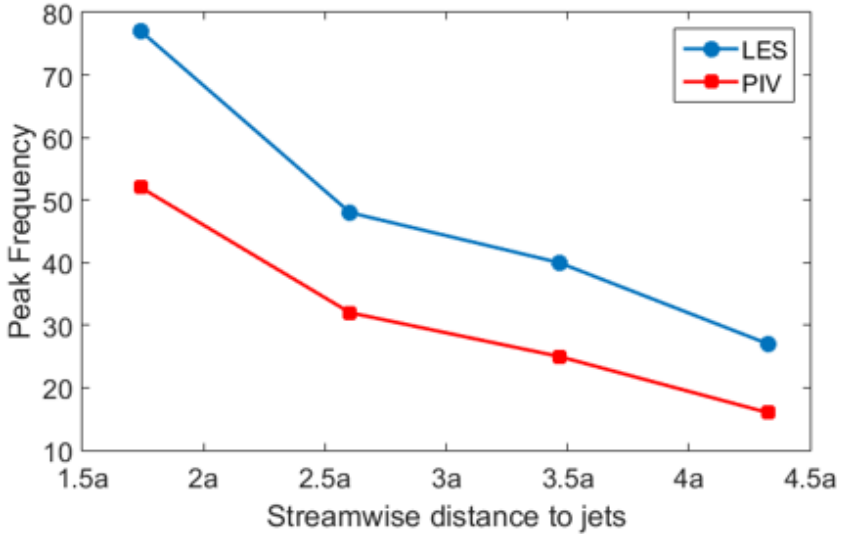

Figure 5.14: Comparison of peak frequency at four sample locations.

where larger eddies break down into smaller eddies in homogeneous turbulent flows. The energy cascade process occurs in the inertial range in which the energy decays at a slope that is maintained at -5/3. This is also known as the Kolmogorov -5/3 law. In figure 5.15, the energy cascade occurs between 30 Hz and 120 Hz, and the viscous effect gradually took over above 120 Hz. Thus, the PSD decay exhibits a steeper slope. The results also indicate that the LES grid is sufficiently fine to resolve the inertial range.

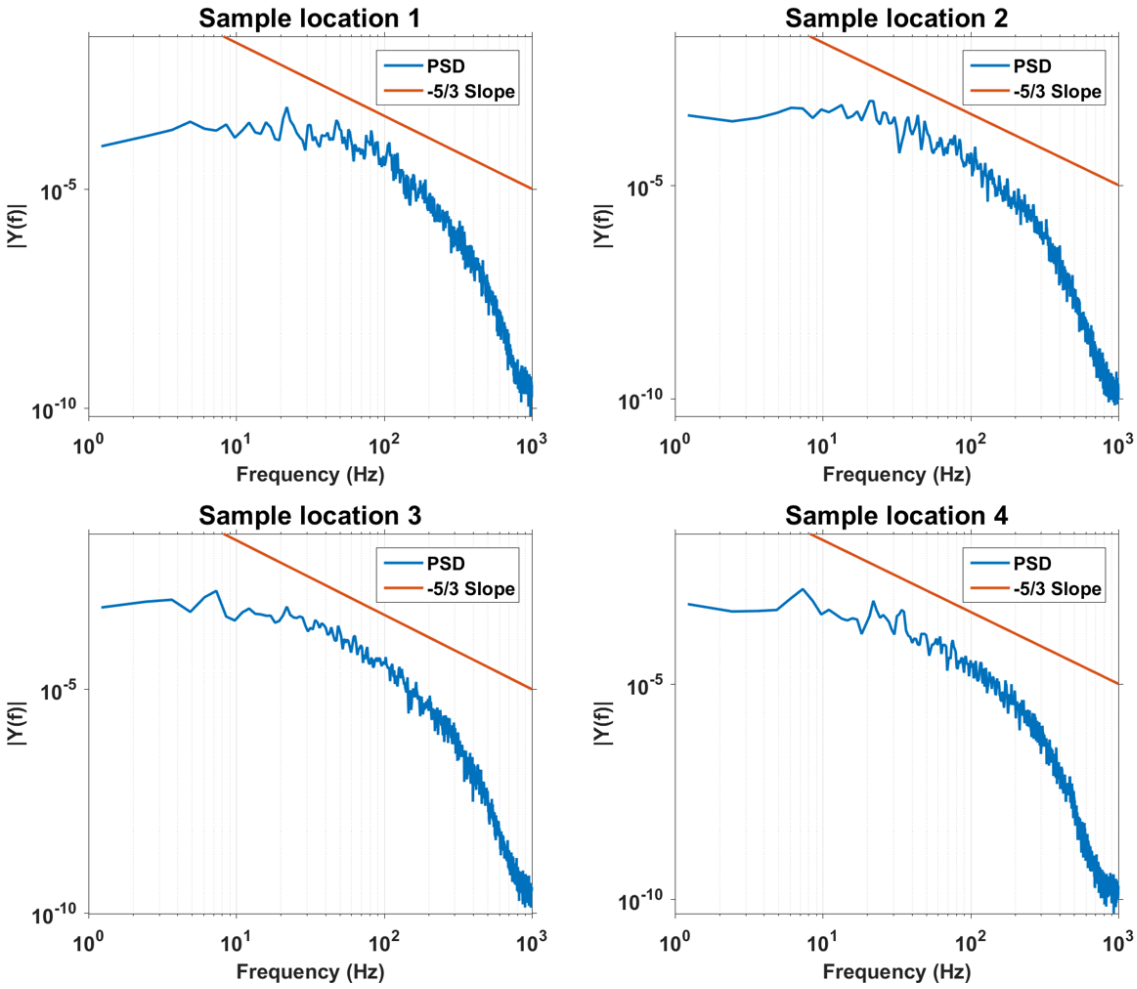

Figure 5.15: PSD of turbulent kinetic energy of probes from LES.

5.4 POD analysis on LES

The proper orthogonal decomposition (POD) analysis on turbulence research was introduced by Lumley [44] to identify the most dominant flow features in experimental data and numerical simulations. The present study uses the snapshot POD method introduced by Sirovich et al. [45]. A detailed description and analysis of the method were discussed by Meyer et al. [46]. More details on POD calculation steps can be found in Appendix C. For a given flow, POD analysis decomposes the velocity field $\vec{u}(x_i, t)$ into a set of orthogonal basis functions $\phi(x_i)$ and a set of temporal coefficients

$\alpha(t)$.

$$\vec{u}^n(x_i, t) = \sum_{n=1}^{N} \alpha_i^n \phi^i \tag{5.6}$$

The vector plots of POD modes 1 and 2 are shown in figure 5.16. In this figure, the left plots depict the vector plots of POD modes 1 and 2 obtained from the present LES, and the right plots depict the PIV data reported by [4]. The vortex structures between the two jets from mode 1 are similar to those of mode 2 data from PIV [4]; however, mode 2 obtained from LES shows similar vortex structures compared to mode 1 from [4]. In order to explain the discrepancy, the turbulent kinetic energy distribution associated with the individual mode is shown in figure 5.17. The first and second modes contained 3.5% and 3.4% of energy respectively, in terms of energy. The mode number is ranked based on the kinetic energy level, and thus, the mix between the first two modes when compared to the PIV data [4] was potentially due to experimental uncertainty or computational uncertainty. In addition, the vortices marked in figure 5.16 are located near the MP. Thus, POD mode 1 and mode 2 likely represent the merging behavior of the twin-jet interaction.

The PSD analysis was performed on POD coefficients of mode 1 and mode 2 as shown in figure 5.18. Mode 1 and mode 2 reveal comparable dominant frequencies corresponding to 16 Hz, 20 - 21 Hz, and 29 Hz. Lee et al. [4] reported similar frequencies from their POD analysis on PIV experimental data, which are 16 Hz, 21 Hz, and 31 Hz. This also proved that although the first two modes from LES and PIV exhibit a mixed match as shown in figure 5.16, they represent analogous vortex structures. As stated before, the vortex structure from the first two modes are located between y/a = 3 and y/a = 4, i.e., near MP. Therefore, the first two modes characterize the merging

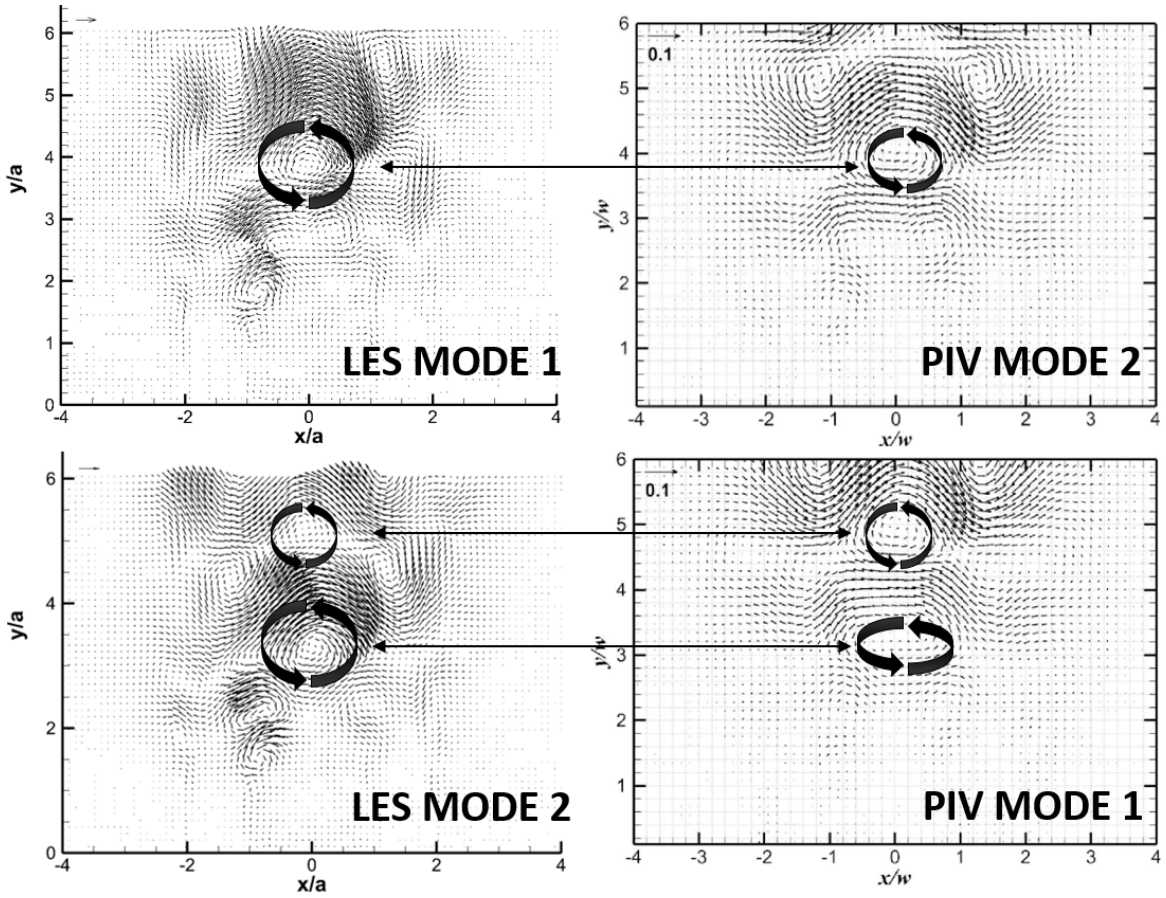

Figure 5.16: Vector plot of POD mode 1 and mode 2 from LES data and PIV benchmark data [4].

behavior between two jets. The spectrum information predicted by LES is comparable to PIV data [4].

Recall that in figure 5.14, the peak frequency from four sample locations exhibited a 25% overprediction when compared with that in the experiments and this was potentially due to the frequency of the centrifugal pump used in the experiments. However, the frequency from the POD coefficient matches well with that in the experiments. Considering that the first two modes represented vortex structures near MP, this indicated that the fluctuation behavior of the merging of two jets was not affected by the pump.

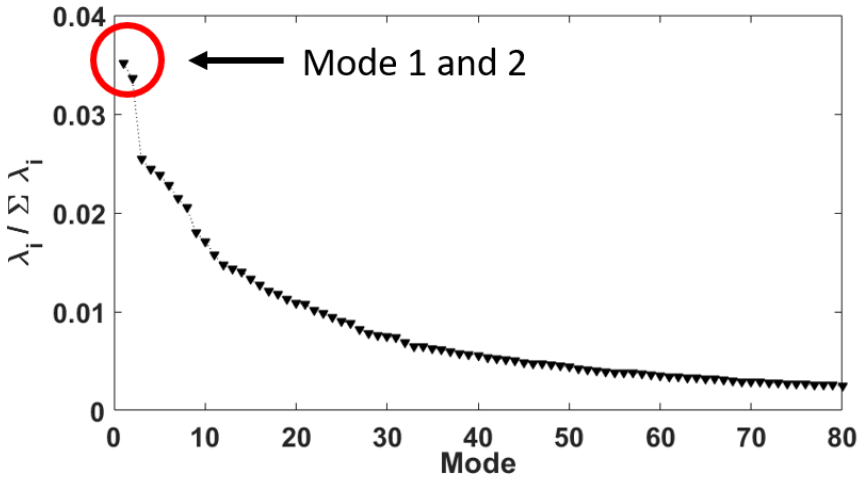

Figure 5.17: Turbulent kinetic energy per POD mode.

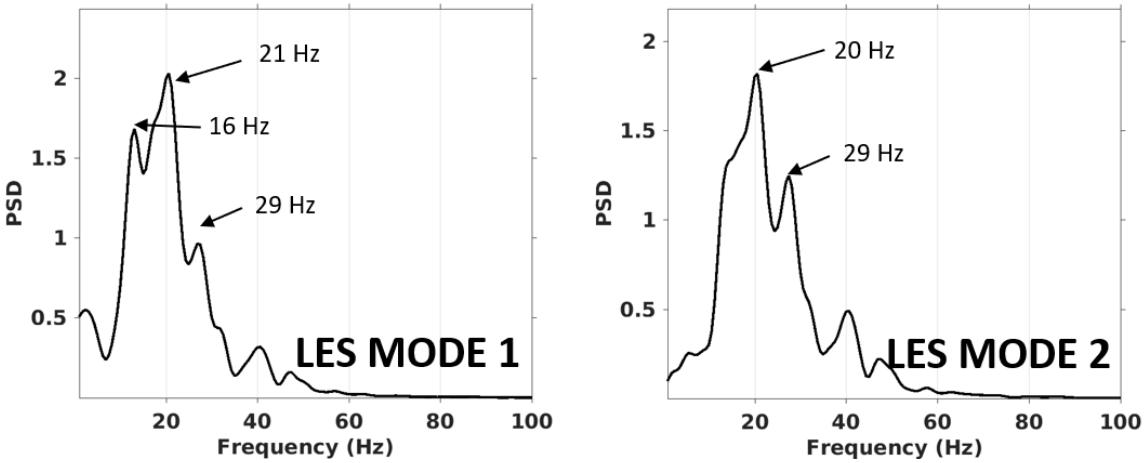

Figure 5.18: Spectral analysis of POD coefficients. (Left: mode 1; Right: mode 2).

Cross-correlation can estimate the deterministic correlation between two deterministic signals. Figure 5.19 shows the selected POD coefficient from mode 1 and mode 2 plotted versus time (left) and the cross-correlation between those coefficients (right). The cross-correlation indicates a 9.2 ms delay between mode 1 and mode 2. In comparison, in the PIV study, Lee et al. [4] indicated a 10 ms delay between mode 1 and mode 2. In this regard, the POD results from LES data in modes 1 and 2 agree well

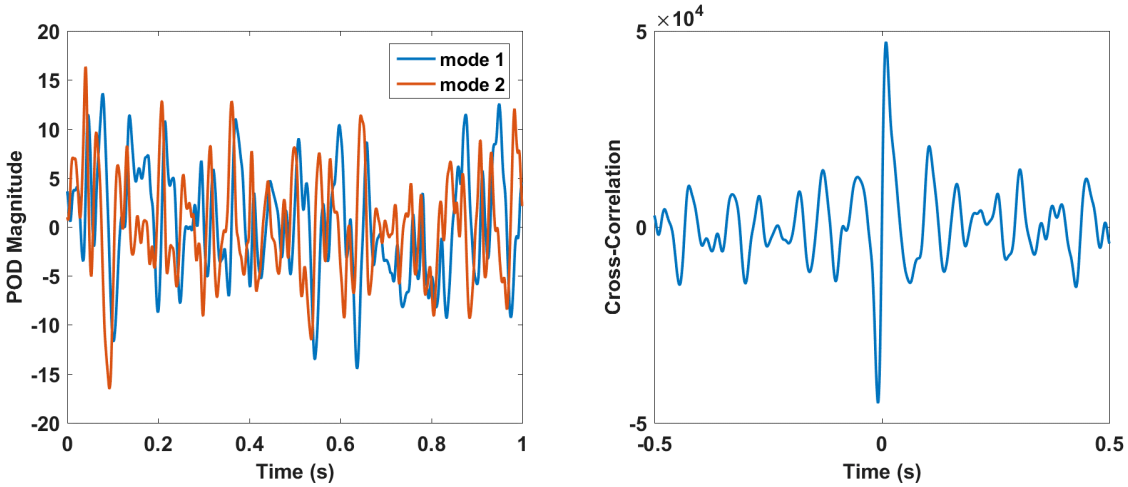

Figure 5.19: POD coefficient plot with respect to time (left) and cross-correlation between mode 1 coefficient and mode 2 coefficient.

with the experimental results [4].

Because the mean flow plus mode 1 and mode 2 consisted of over 95% of kinetic energy, figure 5.20 shows the reconstructed streamwise velocity contour field using the mean velocity and the first two modes at an arbitrary time. The first two modes reveal the interaction between jets to a certain extent. Figure 5.21 shows a comparison of the time-averaged streamwise velocity between the POD reconstructed flow and LES data profile at y/a = 5.6. It is indicated that the reconstructed mean flow exhibits only subtle differences when compared to the original data.

As previously stated, mode 1 and mode 2 describe the vortex structure near the MP. With respect to the reconstructed flow field, the streamwise velocity fluctuation near the MP is extracted for the PSD analysis. Similarly, the same extraction is performed from the original LES data. The PSD analysis is performed on the streamwise fluctuating velocity from the reconstructed flow and LES data, and the spectrum distribution is shown in figure 5.22. The peak frequencies from both data in figure 5.22 approxi-

mately correspond to 19 Hz, which is close to the POD coefficients peak frequency at mode 1 and mode 2. This demonstrated that the first two modes are attributed to the vortex interaction near the MP. In addition, this comparison showed that the first two POD modes in twin jets were sufficient to describe the jets interaction behavior and mean flow.

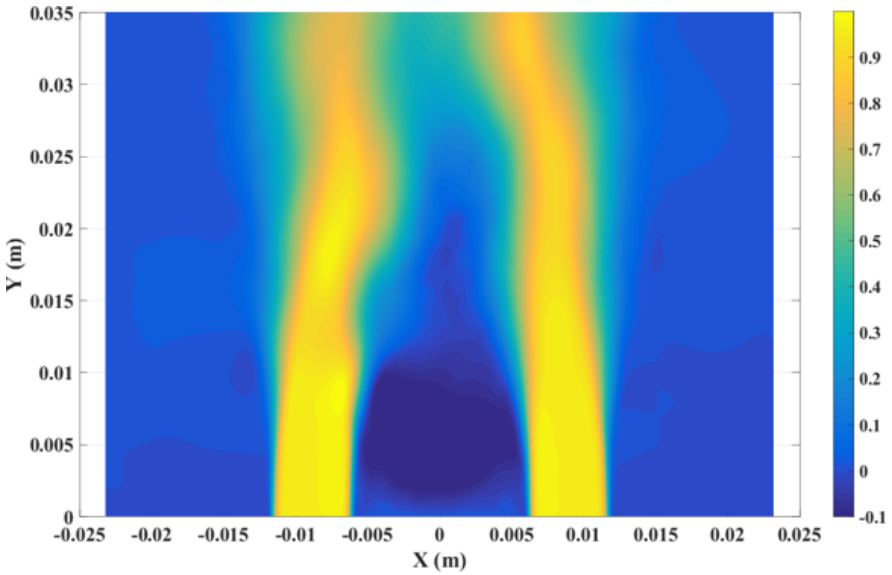

Figure 5.20: Streamwise velocity contour of reconstructed flow from POD mode 1 and mode 2.

To further examine the contribution of more modes, the RMS of streamwise velocity is calculated with different numbers of modes, as shown in figure 5.23. It can be observed that the structure of RMS contour is formed with 10 POD modes, but the magnitude is approximately 50% of those using 1,000 modes.

Figures 5.24 and 5.25 indicate reconstructed stream-wise and transverse velocity fields, respectively, from the first 10, 100, and 1,000 modes. In this study, over 97% of the turbulent kinetic energy is captured by the first 1,000 modes. As shown in

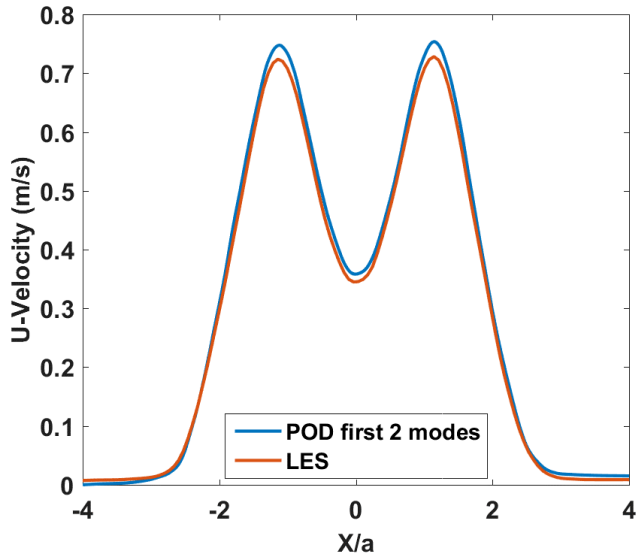

Figure 5.21: Comparison of time-averaged streamwise velocity profile at y/a = 5.6 between original LES data and reconstructed flow field.

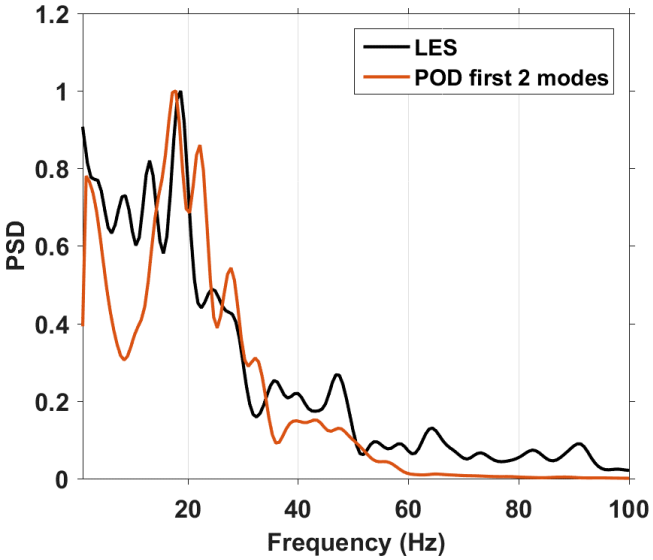

Figure 5.22: Comparison of spectral density between original LES data and reconstructed data using the first 2 modes.

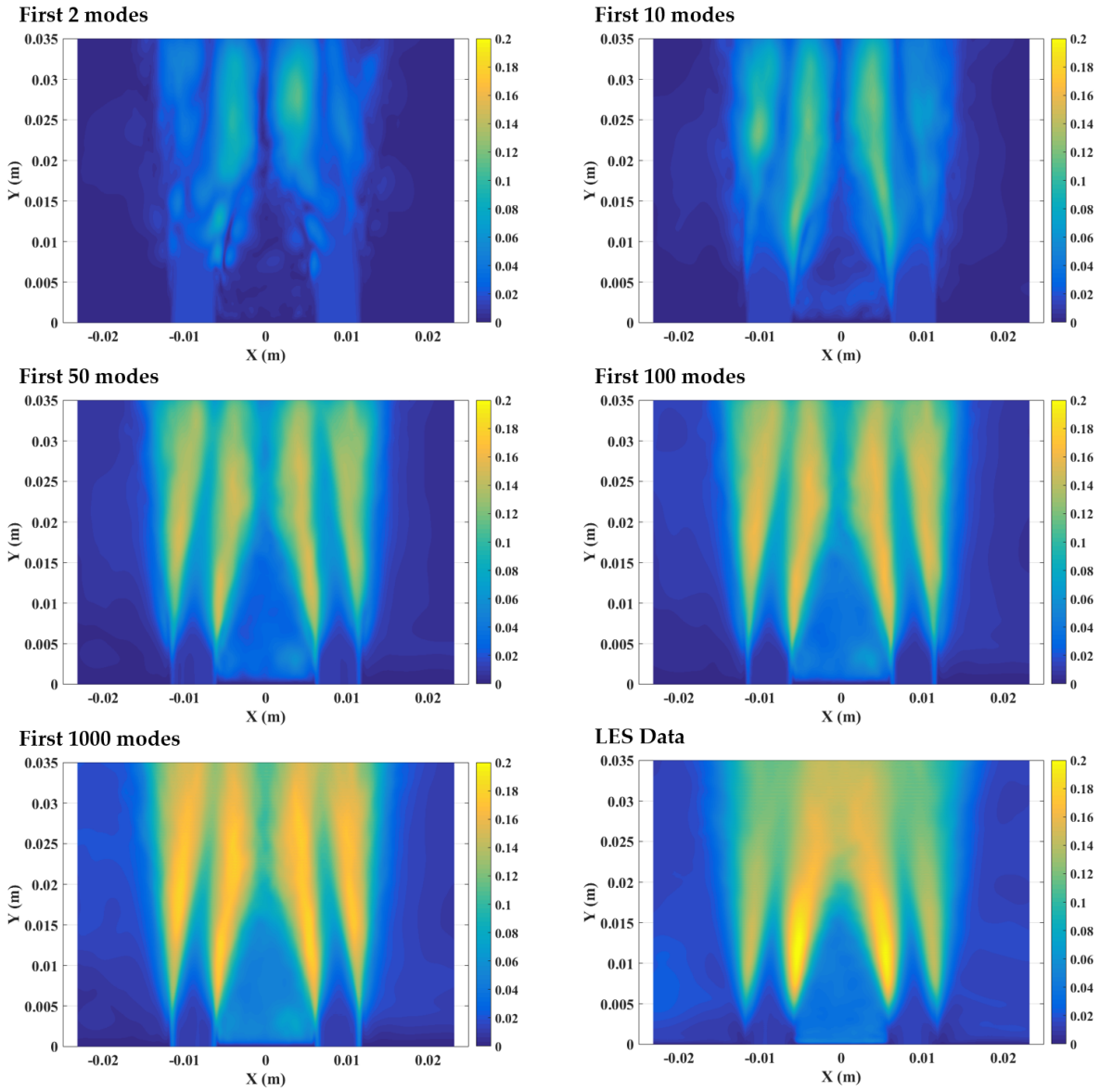

Figure 5.23: Comparison of RMS of streamwise velocity contour between LES data and reconstructed flow using 2 modes (top left), 10 modes (top right), 50 modes (middle left), 100 modes (middle right), and 1,000 modes (bottom left).

figures 5.24 and 5.25, an increase in the number of modes considered in POD flow reconstruction increases the level of detail revealed in the vortex structures. The flow reconstructed from 1,000 modes appears identical to the LES original data in terms of contour plots.

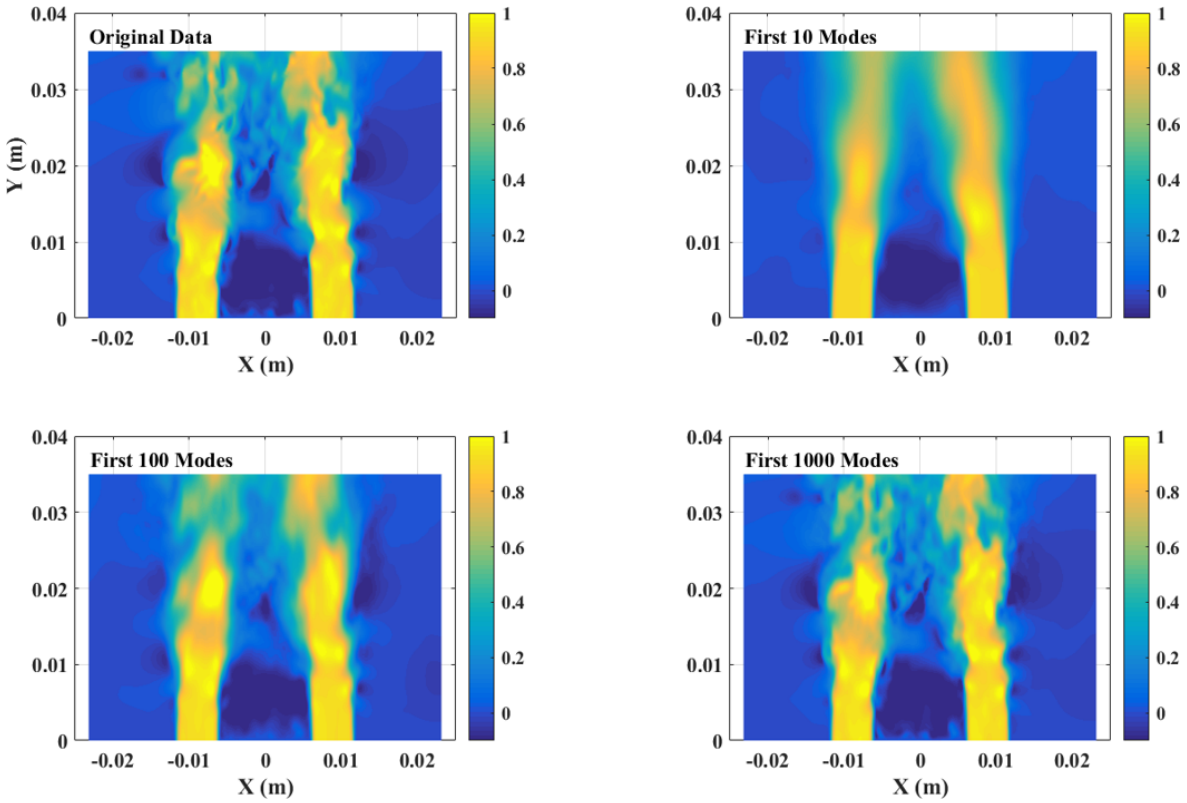

Figure 5.24: Comparison of streamwise velocity contour between LES data and reconstructed flow field using 10 modes (top right), 100 modes (bottom left), and 1,000 modes (bottom right).

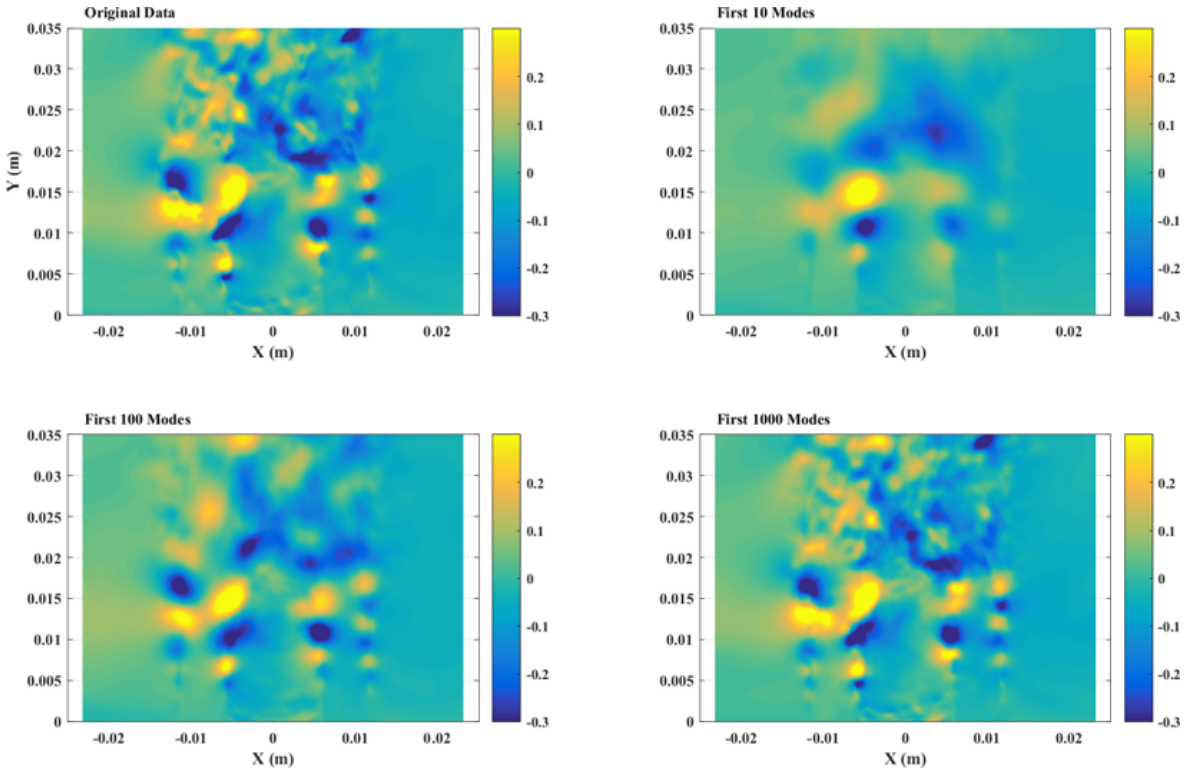

Figure 5.25: Comparison of transverse velocity contour between LES data and reconstructed flow field using 10 modes (top right), 100 modes (bottom left), and 1,000 modes (bottom right).

6. CONCLUSION

Three-dimensional steady-state and transient simulations were conducted using the OpenFOAM solver for a rectangular twin-jet system. The realizable k - ϵ and SST k - ω models were used for the simulation of twin-jet flows; the results were compared with those of the steady-state RANS simulations. For parallel twin-jet flows, the two RANS models realizable k - ϵ and SST k - ω) produced comparable results. The simulation results were compared with the PIV data [2], and the comparison revealed a good agreement at selected locations in the merging region. When the PIV data [2] were used as boundary conditions, the merging points (MPs) were close to those of the experimental data. Regarding the Reynolds stress values, the RANS simulations showed discrepancies. The Boussinesq eddy viscosity assumption tended to overpredict the Reynolds stress components. An investigation on the sensitivity of the boundary conditions revealed that the mixing characteristics of twin jets are sensitive to the inlet boundary conditions. The key to accurately predict the flow field and the merging characteristics of a twin-jet system was the implementation of proper inlet boundary conditions.

In the second part of this study, the PANS simulation was tested by comparing it with the URANS simulation for the transient state based on the same mesh and boundary conditions. The PANS model showed a superior capability in resolving smaller turbulence scales. According to the PSD analysis, the PANS simulation can resolve higher frequencies compared with URANS for the same mesh size. Regarding the mean statistics, the PANS simulation yielded an MP of 3.6a, which was close to experimental measurement ($E_{MP,PANS} = 4.3\%$). With the transient PIV data as the

boundary condition, the PANS can preserve frequency information at the turbulent jet mixing layer while URANS tended to make the frequency decay faster.

In the third part, the LES results of turbulent twin jets were validated relative to the experimental data [4]. The MP and velocity profile at selected locations indicated a good agreement with the experimental data. The flow in the merging region was well represented in the LES data. The LES indicated an MP of 3.54a. The energy cascading phenomenon was observed in the PSD analysis of velocity fluctuation near MP.

The POD analysis results exhibited similar vortex structures when compared to the experimental data [4]. The spectral analysis results on POD mode 1 and mode 2 coefficients exhibited a good agreement with those in the experiments [4] with a peak frequency of 21 Hz. Given that the simulation was not affected by the centrifugal pumps used in the experiments, the frequencies of the first two POD modes were obtained independently of input signal frequency. The LES also showed that even with pump frequency in the affected PIV experiments, the interaction frequency between the two jets was not affected. Specifically, the POD reconstruction using the first two modes indicated that the peak frequency near the MP was preserved after reconstruction, and this could be useful for a reduced order modeling work.

6.1 Computational cost discussion

Figure 6.1 shows the streamwise velocity contour plot as a comparison among the three turbulent models. For RANS, the velocity is mean velocity, whereas for PANS and LES, the velocity was instantaneous velocity. It is evident that LES could reveal clearest transient flow structures in terms of eddies in turbulent flow and interaction between two jets. However, LES is the most computationally expensive method in this

study. Thus, it is beneficial to show CPU hours for each type of simulation.

For steady-state RANS, the simulation took approximately 1,000 CPU hours for the finest mesh in the present work (9.6 million cells). For PANS case (19 million cells), the simulation performed with 240 cores consumed 33,000 CPU hours. For LES case (32 million cells), the simulation used up 135,000 CPU hours.

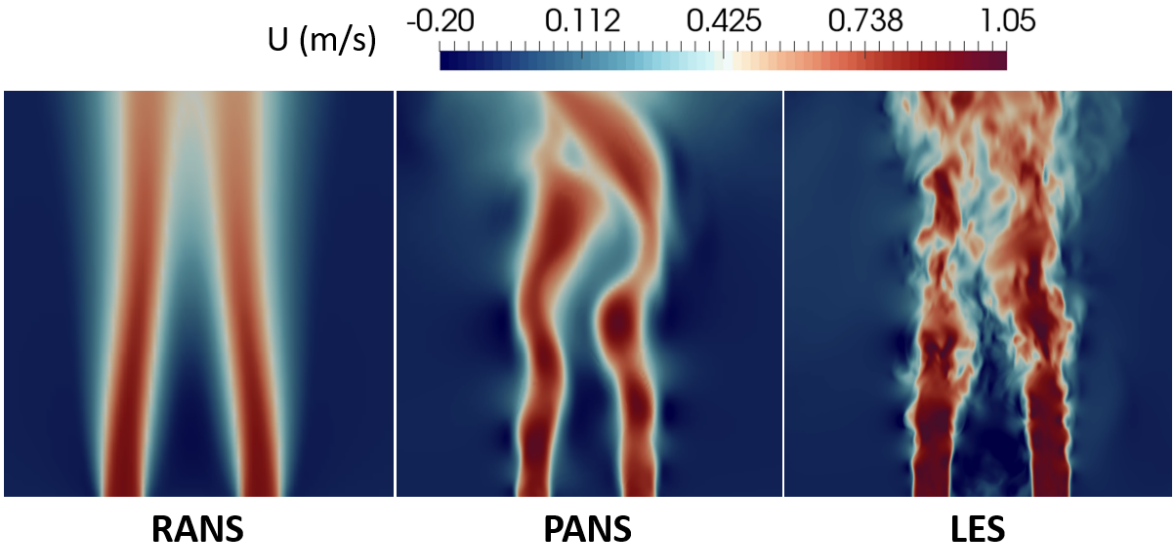

Figure 6.1: Comparison of contour plots of streamwise mean velocity profiles for RANS, PANS, and LES.

6.2 Future work

The recommend future work includes the following directions:

- The PANS simulation showed a good potential to perform reasonably well with one-fourth CPU hours cost of LES. An extensive parameter study to determine the best approach using PANS at various scenarios would be recommended.

- PANS in this study was based on the standard $k-\epsilon$ model. In theory, the PANS

methodology applies to any RANS models. Thus, it is worthwhile to investigate PANS based on other RANS models.

- The POD analysis results indicated a promising tool to reveal the fluctuating eddy structure and it could be used for a reduced order modeling effort in future studies.

REFERENCES

[1] M. Crosskey and A. Ruggles, "UTK twin jet water facility computational fluid dynamics validation data set," in *Proceedings of International Congress on Advances in Nuclear Power Plants (ICAPPŠ14)*, pp. 1940–1945, 2014.

[2] H. Wang, S. Lee, and Y. A. Hassan, "Particle image velocimetry measurements of the flow in the converging region of two parallel jets," *Nucl. Eng. Des.*, vol. 306, pp. 89–97, Sept. 2016.

[3] H. Wang, S. Lee, Y. A. Hassan, and A. E. Ruggles, "Laser-Doppler measurements of the turbulent mixing of two rectangular water jets impinging on a stationary pool," *Int. J. Heat Mass Transf.*, vol. 92, pp. 206–227, Jan. 2016.

[4] S. Lee and Y. A. Hassan, "Experimental study of flow structures near the merging point of two parallel plane jets using PIV and POD," *Int. J. Heat Mass Transf.*, vol. 116, pp. 871–888, Jan. 2018.

[5] "The OpenFOAM foundation." `https://openfoam.org/`. Accessed: 2018-06-01.

[6] H. G. Weller, G. Tabor, H. Jasak, and C. Fureby, "A tensorial approach to computational continuum mechanics using object-oriented techniques," *Computers in Physics*, vol. 12, pp. 620–631, Nov. 1998.

[7] S. B. Pope, *Turbulent flows*. Cambridge University Press, Oct. 2000.

[8] D. C. Wilcox *et al.*, *Turbulence modeling for CFD*, vol. 2. DCW industries La Canada, CA, 1993.

[9] D. R. Miller and E. W. Comings, "Force-momentum fields in a dual-jet flow," *J. Fluid Mech.*, vol. 7, p. 237, Feb. 1960.

[10] E. Tanaka, "The interference of two-dimensional parallel jets : 1st report, experiments on dual jet," *Bulletin of JSME*, vol. 13, no. 56, pp. 272–280, 1970.

[11] E. Tanaka, "The interference of two-dimensional parallel jets : 2nd report, experiments on the combined flow of dual jet," *Bulletin of JSME*, vol. 17, no. 109, pp. 920–927, 1974.

[12] G. F. Marsters, "Interaction of Two Plane, Parallel Jets," *AIAA Journal*, vol. 15, pp. 1756–1762, Dec. 1977.

[13] H. Elbanna, S. Gahin, and M. I. I. Rashed, "Investigation of two plane parallel jets," *AIAA Journal*, vol. 21, pp. 986–991, July 1983.

[14] Y. F. Lin and M. J. Sheu, "Investigation of two plane paralleltiinven ilated jets," *Exp. Fluids*, vol. 10, pp. 17–22, Oct. 1990.

[15] A. Nasr and J. C. S. Lai, "Two parallel plane jets: Mean flow and effects of acoustic excitation," *Exp. Fluids*, vol. 22, pp. 251–260, Jan. 1997.

[16] N. E. Bunderson and B. L. Smith, "Passive mixing control of plane parallel jets," *Exp. Fluids*, vol. 39, pp. 66–74, July 2005.

[17] J. C. S. Lai and A. Nasr, "Two parallel plane jets: comparison of the performance of three turbulence models," *Proc. Inst. Mech. Eng. G J. Aerosp. Eng.*, vol. 212, pp. 379–391, Jan. 1998.

[18] E. A. Anderson and R. E. Spall, "Experimental and Numerical Investigation of Two-Dimensional Parallel Jets," *J. Fluids Eng.*, vol. 123, pp. 401–406, June 2001.

[19] A. Durve, A. W. Patwardhan, I. Banarjee, G. Padmakumar, and G. Vaidyanathan, "Numerical investigation of mixing in parallel jets," *Nucl. Eng. Des.*, vol. 242, pp. 78–90, Jan. 2012.

[20] A. Nasr and J. Lai, "An Investigation on Applying Reichardt's Hypothesis to Flow Prediction of Ventilated Two Parallel Plane Jets," *Advances in Aerospace Science and Applications*, vol. 1, no. 1, pp. 1–6, 2011.

[21] O. Reynolds, "On the dynamical theory of incompressible viscous fluids and the determination of the criterion," *Philosophical Transactions of the Royal Society of London A: Mathematical, Physical and Engineering Sciences*, vol. 186, pp. 123–164, Jan. 1895.

[22] J. Boussinesq, *Essai sur la theorie des eaux courantes.* Paris,: Imprimerie Nationale„ 1877.

[23] B. Launder and B. Sharma, "Application of the energy-dissipation model of turbulence to the calculation of flow near a spinning disc," *Letters in heat and mass transfer*, vol. 1, no. 2, pp. 131–137, 1974.

[24] T.-H. Shih, W. W. Liou, A. Shabbir, Z. Yang, and J. Zhu, "A new k-epsilon eddy viscosity model for high reynolds number turbulent flows," *Computers & Fluids*, vol. 24, no. 3, pp. 227–238, 1995.

[25] D. C. Wilcox, "Reassessment of the scale-determining equation for advanced turbulence models," *AIAA journal*, vol. 26, no. 11, pp. 1299–1310, 1988.

[26] F. R. Menter, "Two-equation eddy-viscosity turbulence models for engineering applications," *AIAA journal*, vol. 32, no. 8, pp. 1598–1605, 1994.

[27] S. Patankar, *Numerical Heat Transfer and Fluid Flow*. CRC Press, Jan. 1980.

[28] H. Li, N. K. Anand, and Y. A. Hassan, "Computational study of turbulent flow interaction between twin rectangular jets," *Int. J. Heat Mass Transf.*, vol. 119, pp. 752–767, Apr. 2018.

[29] P. J. Roache, "Perspective: A method for uniform reporting of grid refinement studies," *J. Fluids Eng.*, vol. 116, pp. 405–413, Sept. 1994.

[30] P. J. Roache, "Quantification of uncertainty in computational fluid dynamics," *Annu. Rev. Fluid Mech.*, vol. 29, pp. 123–160, Jan. 1997.

[31] S. Girimaji and K. Abdol-Hamid, "Partially-averaged navier stokes model for turbulence: Implementation and validation," in *43rd AIAA Aerospace Sciences Meeting and Exhibit*, vol. 2000, (Reston, Virigina), p. 2000, American Institute of Aeronautics and Astronautics, Jan. 2005.

[32] S. S. Girimaji, "Partially-averaged navier-stokes model for turbulence: A reynolds-averaged navier-stokes to direct numerical simulation bridging method," *J. Appl. Mech.*, vol. 73, pp. 413–421, May 2006.

[33] H. Tennekes, J. L. Lumley, J. Lumley, *et al.*, *A first course in turbulence*. MIT press, 1972.

[34] B. Akula, P. Roy, P. Razi, S. Anderson, and S. Girimaji, "Partially-averaged navier-stokes (pans) simulations of lid-driven cavity flow—part 1: Comparison with urans and les," in *Progress in Hybrid RANS-LES Modelling* (S. Girimaji, W. Haase, S.-H. Peng, and D. Schwamborn, eds.), vol. 130 of *Notes on Numerical Fluid Mechanics and Multidisciplinary Design*, pp. 359–369, Cham: Springer, Cham, 2015.

[35] B. Chaouat and R. Schiestel, "Analytical insights into the partially integrated transport modeling method for hybrid reynolds averaged navier-stokes equations-large eddy simulations of turbulent flows," *Phys. Fluids*, vol. 24, p. 085106, Aug. 2012.

[36] B. Basara, S. Krajnovic, S. Girimaji, and Z. Pavlovic, "Near-Wall formulation of the partially averaged navier stokes turbulence model," *AIAA Journal*, vol. 49, pp. 2627–2636, Dec. 2011.

[37] H. Weller, "Controlling the computational modes of the arbitrarily structured C grid," *Mon. Weather Rev.*, vol. 140, pp. 3220–3234, Apr. 2012.

[38] J. Smagorinsky, "General circulation experiments with the primitive equations," *Mon. Weather Rev.*, vol. 91, pp. 99–164, Mar. 1963.

[39] F. Nicoud and F. Ducros, "Subgrid-scale stress modelling based on the square of the velocity gradient tensor," *Flow, Turbulence and Combustion*, vol. 62, pp. 183–200, Sep 1999.

[40] F. S. Sarikurt and Y. A. Hassan, "Large eddy simulations of erosion of a stratified layer by a buoyant jet," *Int. J. Heat Mass Transf.*, vol. 112, pp. 354–365, Sept. 2017.

[41] J. Jeong and F. Hussain, "On the identification of a vortex," *J. Fluid Mech.*, 1995.

[42] Y. M. Shim, R. N. Sharma, and P. J. Richards, "Proper orthogonal decomposition analysis of the flow field in a plane jet," *Exp. Therm. Fluid Sci.*, vol. 51, pp. 37–55, Nov. 2013.

[43] C. D. Winant and F. K. Browand, "Vortex pairing: the mechanism of turbulent mixing-layer growth at moderate reynolds number," *Journal of Fluid Mechanics*, vol. 63, no. 2, pp. 237–255, 1974.

[44] J. L. Lumley, "The structure of inhomogeneous turbulent flows," *Atmospheric turbulence and radio wave propagation*, 1967.

[45] L. Sirovich, "Turbulence and the dynamics of coherent structures. i. coherent structures," *Quart. Appl. Math.*, 1987.

[46] K. E. Meyer, J. M. Pedersen, and O. Özcan, "A turbulent jet in crossflow analysed with proper orthogonal decomposition," *J. Fluid Mech.*, vol. 583, pp. 199–227, July 2007.

[47] L. F. Richardson, "On the approximate arithmetical solution by finite differences of physical problems involving differential equations, with an application to the stresses in a masonry dam," *Proceedings of the Royal Society of London A: Mathematical, Physical and Engineering Sciences*, vol. 83, no. 563, pp. 335–336, 1910.

[48] W. L. Oberkampf and C. J. Roy, *Verification and Validation in Scientific Computing*. Cambridge University Press, Oct. 2010.

[49] J. E. Gentle, *Numerical Linear Algebra for Applications in Statistics*, ch. 3.2.7 Singular Value Factorization, pp. 102–103. Berlin: Springer-Verlag, 1998.

[50] S. Wold, K. Esbensen, and P. Geladi, "Principal component analysis," *Chemometrics Intellig. Lab. Syst.*, vol. 2, pp. 37–52, Aug. 1987.

[51] J. Lumley, "Coherent structures in turbulence," in *Transition and Turbulence* (R. E. MEYER, ed.), pp. 215 – 242, Academic Press, 1981.

[52] K. Fukunaga, *Introduction to statistical pattern recognition*. Academic press, 2013.

APPENDIX A

ADDITIONAL DETAIL ON GRID CONVERGENCE INDEX

This appendix section provides additional information on Grid Convergence Index (GCI) and its derivations. GCI was proposed by Roache [29] with the intention of providing a uniform approach for reporting grid refinement studies. The original GCI method was used to report the relative difference between two computational grids. As stated by Roache [30], GCI can also be used to account for uncertainty from a certain numerical solution, which can be used as the error-bars for CFD results.

Since the GCI method was introduced based on Richardson extrapolation, Appendix A.1 will present the generalize Richardson extrapolation. Appendix A.2 will show the development of GCI.

A.1 Generalized Richardson extrapolation

The Richardson extrapolation was originally proposed in 1910 [47]. The basic concept behind Richardson extrapolation can be explained as follows: if one knows the rate of convergence of a discretization method with a certain mesh refinement, based on two discretized solutions from systematic mesh refinement, one can estimate the exact solution of the mathematical model. The original Richardson extrapolation was formulated exclusively for a second-order scheme. For a generalized p^{th}-order accurate scheme, the error expansion is defined as [48]

$$\varepsilon_h = f_h - \hat{f} = g_p h^p + g_{p+1} h^{p+1} + g_{p+2} h^{p+2} + \dots \tag{A.1}$$

where the subscript h is the grid spacing, f_h is discretized solution, $\hat{f}$ is the exact solution, and g are expansion coefficients for the generalized Richardson extrapolation.

Now, we define the grid refinement factor as the ratio of the coarse grid spacing over the fine grid spacing:

$$r = \frac{h_2}{h_1} > 1 \tag{A.2}$$

where h_2 is the coarse grid spacing, and h_1 is the fine grid spacing.

We have, $h_2 = rh_1$, and equation (A.1) from two different meshes can be rewritten as

$$f_{h_1} = \hat{f} + g_p h_1^p + g_{p+1} h_1^{p+1} + \mathcal{O}(h_1^{p+2}) \tag{A.3}$$

$$f_{rh_1} = f_{exact} + g_p (rh_1)^p + g_{p+1} (rh_1)^{p+1} + \mathcal{O}((rh_1)^{p+2}) \tag{A.4}$$

We eliminate g_p by $r^p\times$ equation (A.3) $-$ equation (A.4):

$$f_{exact} = f_h + \frac{f_h - f_{rh}}{r^p - 1} + g_{p+1} (h_1)^{p+1} \frac{r^p (r-1)}{r^p - 1} + \mathcal{O}(h_1^{p+2}) \tag{A.5}$$

Combining terms of order h^{p+1} and higher with the exact solution, we obtain

$$\tilde{f} = f_{exact} - g_{p+1} (h_1)^{p+1} \frac{r^p (r-1)}{r^p - 1} - \mathcal{O}(h_1^{p+2}) \tag{A.6}$$

where $\tilde{f}$ is the estimated solution by the generalized Richardson extrapolation:

$$\tilde{f} = f_h + \frac{f_h - f_{rh}}{r^p - 1} \tag{A.7}$$

Equation (A.7) is the generalized Richardson extrapolation with $(p+1)$ order accuracy.

A.2 Grid convergence index

To introduce Roache's grid convergence index, we consider the relative discretization error (RDE) of the fine grid from the generalized Richardson extrapolation as indicated below:

$$RDE_1 = \frac{f_1 - \tilde{f}}{f_1} \tag{A.8}$$

where the subscript 1 represents the fine grid.

Substituting equation (A.7) into the above equation, and using f_1 to represent the fine grid solution, and f_2 the coarse grid solution, we have,

$$RDE_1 = \frac{f_2 - f_1}{f_1 r^p - f_1} \tag{A.9}$$

To understand the importance of the grid refinement factor r and the discretization order p in RDE_1, consider the following example. Given two numerical solutions of some quantity of interest f obtained from fine and coarse grid values as 0.95 and 1, respectively; this gives the a relative difference of 5% between two solutions. For a 2^{nd} order accurate scheme with grid refinement factor $r = 2$, $RDE_1 = 1.67\%$. On the other hand, for a 1^{st} order accurate scheme with grid refinement factor $r = 1.5$, $RDE_1 = 10\%$. Therefore, the relative difference between two grid solutions can mean very different depending on the grid refinement factor r and order of accuracy p.

Roache [29] proposed the original GCI method based on the aforementioned relative

discretization error; the GCI for the fine grid numerical solution is defined below:

$$GCI_{fine} = \frac{F_s|\frac{f_1-f_2}{f_1}|}{(r^p-1)} \tag{A.10}$$

If a large number of CFD computations are to be performed, one may wish to use the coarser grid with h_2 for GCI; thus, RDE_2 is defined as:

$$\begin{aligned} RDE_2 &= \frac{f_2-\tilde{f}}{f_2} \\ &= \frac{f_2-(f_1+\frac{f_1-f_2}{r^p-1})}{f_2} \\ &= \frac{f_2-f_1}{f_2}+\frac{f_2-f_1}{f_2}\frac{1}{r^p-1} \\ &= \frac{f_2-f_1}{f_2}(1+\frac{1}{r^p-1}) \\ &= \frac{f_2-f_1}{f_2}(\frac{r^p}{r^p-1}) \end{aligned} \tag{A.11}$$

Therefore, GCI_{coarse} is defined for coarse grid error estimation as

$$GCI_{coarse} = \frac{F_s r^p}{(r^p-1)}|\frac{f_1-f_2}{f_2}| \tag{A.12}$$

In the present study with steady state RANS (Section 3), GCI_{fine} was used for solution verification and discretization error estimation.

APPENDIX B

SPECTRAL ANALYSIS

In the present study, spectral analysis was used to investigate the frequency information from transient simulations (PANS, URANS, and LES), see Sections 4.3.3 and 5.3.3. Fast Fourier Transform (FFT) was used to transform velocity signals from time domain to frequency domain. Power Spectral Density (PSD) is a method for evaluating signal power as a function of frequency. This study used PSD to calculate the turbulent kinetic energy distribution as a function of the signal frequency.

B.1 Fast Fourier transform

All periodic waves can be generated by combining *sin* and *sos* waves of different frequencies. Fourier transform decomposes a periodic wave into its component frequencies:

$$F(k) = \int_{-\infty}^{\infty} f(x) e^{-2\pi i k x} dx \tag{B.1}$$

where $f(x)$ is a series of the signal as a function of x, $F(k)$ is signals in frequency domain, and k represents frequencies.

Discrete Fourier transform (DFT) is a method that converts a finite sequence of equally-spaced discrete sample data into a set of complex numbers giving frequency amplitudes for *sin* and *cos* components. FFT is an efficient algorithm to compute DFT. FFT interprets a series of discrete signal from a time or space domain to a frequency domain. DFT is defined as,

$$F_k = \sum_{n=1}^{N-1} f_n e^{-i2\pi kn/N}, \quad with \quad k = 0, 1, ..., N-1 \tag{B.2}$$

FFT computes the same results as DFT, but reduces the number of operations from $2N^2$ to $2N \cdot log_2 N$. FFT is a useful technique to reveal periodicities in input signals as well as the relative strengths of any periodic components. In the present study, FFT is used to identify dominant frequencies of eddies in turbulent flow from discrete velocity signals.

B.2 Power spectral density

Power Spectral Density (PSD) is a technique for measuring a signal power content as a function of frequency. PSD calculation performs a Fourier integral transform on the autocorrelation of a discrete signal. The function can be described as:

$$P_x(f) = \int_{-\infty}^{\infty} R_x(\tau)\, e^{-2\pi i f \tau} d\tau \tag{B.3}$$

where $R_x(\tau) = E[x(t+\tau) \cdot\ x(t)]$ which is the autocorrelation function of signal $x(t)$. Similar to FFT, PSD analysis also converts the signal from time domain to frequency domain. In contrast to FFT, PSD maps the energy distribution in the frequency domain.

PSD is useful for investigating turbulent kinetic energy distributions in the frequency domain. For example, the energy cascade process where large-scale motions induce smaller-scale motions in turbulent flow can be examined by performing a PSD analysis on fluctuating velocity signals or transient turbulent kinetic energy signals.

APPENDIX C

PROPER ORTHOGONAL DECOMPOSITION

The proper orthogonal decomposition (POD) method was developed independently by several researchers; thus, it is known by different names in different fields, such as singular value decomposition (SVD) [49] or principal component analysis (PCA) [50]. The POD for fluid mechanics was introduced by Lumley [51]. The basic idea of the POD method is that the field data (for example, the velocity field u_i) is approximated as a finite sum in the variables-separated form such as the following:

$$\mathbf{u}^n = \sum_{n=1}^{N} \alpha_i^n \phi^i \tag{C.1}$$

where α_i^n denotes the time-dependent expansion coefficients determined by projecting the velocity to POD modes, whereas ϕ^i represents the POD modes in space which will be defined in equation (C.6)

In this study, instantaneous velocity fields, such as PIV snapshots, are extracted from the simulation at each time step. The first step for POD analysis involves obtaining the mean velocity field. Based on the mean velocity field, the fluctuating part of the velocity field is calculated at each time step for POD analysis. All fluctuating velocity components from a single time step are arranged as a column of data. The present study used 8,250 snapshots for the POD calculation. For **N** snapshots, the matrix **U** is arranged as follows:

$$\mathbf{U} = \left[\mathbf{u^1 u^2} \ldots \mathbf{u^N}\right] = \begin{bmatrix} u_1^1 & u_1^2 & \ldots & u_1^N \\ \vdots & \vdots & \vdots & \vdots \\ u_M^1 & u_M^2 & \ldots & u_M^N \\ v_1^1 & v_1^2 & \ldots & v_1^N \\ \vdots & \vdots & \vdots & \vdots \\ v_M^1 & v_M^2 & \ldots & v_M^N \\ w_1^1 & w_1^2 & \ldots & w_1^N \\ \vdots & \vdots & \vdots & \vdots \\ w_M^1 & w_M^2 & \ldots & w_M^N \end{bmatrix} \tag{C.2}$$

The auto-covariance matrix is formulated as

$$\mathbf{C} = \mathbf{U^T} \cdot \mathbf{U} \tag{C.3}$$

Then the corresponding eigenvalue problem is solved as

$$\widetilde{\mathbf{C}}\mathbf{A^i} = \lambda^i \mathbf{A^i} \tag{C.4}$$

The solution is then ordered according to the size of eigenvalues, as

$$\lambda^1 > \lambda^2 > \ldots > \lambda^N = 0 \tag{C.5}$$

The eigenvectors constitute the basis for reconstructing the POD modes,

$$\phi^i = \frac{\mathbf{U}\mathbf{A}^i}{||\mathbf{U}\mathbf{A}^i||}, \quad i = 1, 2, \ldots, N \tag{C.6}$$

where "|| ||" is the matrix norm operator.

Each snapshot can be expanded into a series of POD modes with an expansion coefficient a_i for each POD mode i. The coefficients are known as POD coefficients, which can be determined by projecting the fluctuating part of the velocity field onto the POD modes. The POD coefficient can be calculated using equation (C.7).

$$\alpha_i = \phi^i \mathbf{u}^n \tag{C.7}$$

From Fukunaga [52], the amount of total kinetic energy from velocity fluctuations associated with a given POD mode is proportional to the corresponding eigenvalue. Thus, the ordering eigenvalues in equation (C.5) can ensure that the most important mode in terms of energy is the first mode. The results and discussions on POD analysis with LES data are presented in Section 5.4.